UNIVERSITÀ DEGLI STUDI DI SALERNO

PHD IN PHOTOVOLTAICS

Dottorato di Interesse Nazionale in Photovoltaics

Curriculum: Design and Integration

Time domain identification of photovoltaic modules dynamic parameters by physics informed neural networks

Dipartimento di Ingegneria dell'Informazione ed Elettrica e Matematica Applicata

Supervisor:

Prof. Giovanni Spagnuolo

PhD Candidate:

Nikta Shamsmohammadi

Mat. 8860800019

PhD Program Director:

Prof. Giovanni Spagnuolo

XXXVIII Cycle

2022 - 2025

Funded by the European Union

MUR
Ministero dell'Università e della Ricerca

Dottorato di Interesse Nazionale

PhD PV

Dottorato di Interesse Nazionale "PHOTOVOLTAICS"

Curricula:

- Solar cells technologies and lifecycle
- Design and integration
- Monitoring and diagnosis
- Power electronics and control
- Solar intermittency and storage
- Distributed generation and grid connection

Contents

List of Figures

List of Tables

0.1 Summary

General framework: In this research, a novel framework based on Physics-Informed Neural Networks (PINNs) is presented to enhance the estimation of dynamic parameters in photovoltaic (PV) generators in the time domain. The proposed framework combines data-driven learning with the governing physical equations of the PV dynamic circuit, enabling accurate reconstruction of the system's transient and dynamic behavior. The study addresses the challenge of accurately identifying PV physical parameters under varying environmental conditions, which has been a persistent problem in traditional data-driven or optimization-based methods due to their high data dependency, sensitivity to noise, and lack of physical consistency. In the proposed approach, time-domain voltage and current waveform are used as inputs, while the physical differential equations of the PV system are embedded into the network's cost function. This enables the model to learn from both experimental data and physical principles, achieving robust and accurate parameter estimation even under noisy or limited measurement conditions and less physics knowlages. The main goal of this research is to develop a time-domain model capable of reproducing the transient and dynamic behavior of PV generators with high accuracy, providing a reliable foundation for system control, performance monitoring, and fault diagnosis in photovoltaic applications. This research introduces a series of PINN-based frameworks developed to improve the accuracy, stability, and interpretability of parameter estimation in PV generators under dynamic and noisy conditions. Each framework addressing specific limitations and progressively enhancing the model's capability to capture the real physical behavior of PV systems in the time domain.

Baseline design: The work begins with a baseline PINN framework constructed on a standard single-diode PV circuit model incorporating a linear capacitor. The main goal of this initial design to evaluate the feasibility of using a physics-informed approach for estimating key physical parameters directly in the time domain. The loss function combines both

data-driven and physics-based components, enabling the model to simultaneously learn from experimental measurements and governing equations and in the research introduces an adaptive loss-weighting mechanism to balance the data and physics losses dynamically during training, ensuring stable convergence across parameters of different scales. Based on this methodology, the model developed into a nonlinear capacitor model, in which the junction capacitance is voltage-dependent. By embedding the nonlinear capacitance directly into the physical constraints of the PINN, the model achieved more accurate transient response predictions and lower estimation errors for both capacitance and series resistance. The accurate estimation of parameters in nonlinear model exhibited possibility of integration of nonlinear junction capacitance within a PINN framework for PV modeling.

Multiple PINN network structure: To further enhance training stability, a Multiple PINN architecture proposed. In this structure, independent subnetworks assigned to each parameter, while all networks remained governed by the same physical constraints. This approach improved convergence speed and numerical stability, particularly for parameters with different natural behavior. The results showed a higher estimation accuracy compared to the PINN network. The novelty of this approach lies in the introduction of a new structure that effectively decouples parameter learning based on their dynamic influence within the PV circuit.

Two-level layered PINN structure: A two-level layered PINN framework developed to estimate environmental and physical parameters. In this network, the first layer predicts environmental conditions such as irradiance and temperature, while the second layer uses these estimates to estimate the value of daynamic capacitor. This configuration enables the network to capture environmental dependencies explicitly and integrate them into the parameter estimation process. This represents the Two-Level layered PINN framework capable of simultaneously learning environmental and physical characteristics in PV systems.

Outcome: The proposed architectures offer a more advanced and physically consistent alternative to traditional optimization algorithms and

conventional data-driven neural networks. By integrating physical knowledge with data-driven learning, they achieve faster convergence, higher estimation accuracy, and greater robustness against noise and measurement uncertainty. Importantly, these architectures have been specifically designed for PV systems, taking into account their unique electrical characteristics, nonlinear dynamics, and environmental dependencies. Unlike general-purpose estimation models, the proposed designs explicitly incorporate the governing equations and transient behavior of PV circuits, enabling them to accurately model how current, voltage, and capacitance interact under varying irradiance and temperature conditions. This PV-oriented design makes the frameworks particularly effective in capturing the real physical behavior of PV modules during dynamic operation, which is crucial for understanding and predicting system performance under realistic environmental variations. As a result, the developed models provide a reliable, interpretable, and physically grounded tool for dynamic modeling, adaptive control, and fault diagnosis in photovoltaic applications.

Chapter 1

1

Introduction

The environmental impact of traditional energy production demonstrates the necessity of developing clean and more sustainable energy sources [1]. Solar power is one of the most important renewable energy sources, as it can be efficiently converted into electricity using photovoltaic (PV) systems known for their reliability and adaptability across different applications [2].

PV cells are the units that convert solar energy into electrical power. However, since each cell generates a limited amount of energy, several cells are connected in series and parallel configurations to form modules capable of delivering the required voltage and current levels. The performance and reliability of PV modules can be affected by multiple factors, including environmental conditions, electrical fluctuations, and material aging [3–6]. These effects may cause partial failures in some cells or reduced efficiency in certain modules, which affects the total energy output and overall system performance. Therefore, to extend the lifetime and ensure stable operation of PV modules, system management and monitoring are essential, and accurate modeling of PV systems is crucial for performance prediction, control, and fault diagnosis [7].

To perform reliable fault diagnosis and system monitoring, it is necessary to understand how the PV system behaves under different operating conditions. Therefore, modeling the PV system is essential to accurately

represent how variations in parameters affect the electrical behavior of the module. Accurate parameters identification provides into the health and degradation of PV systems, enabling early detection of faults and improving the precision of control and performance prediction algorithms [8].

1.1 Problem Statement

Several models are proposed to describe the behavior of PV systems. The most widely used model is the Single-Diode Model (SDM). This model represents the current-voltage (I–V) characteristics of PV modules. Although these models are widely used due to their simplicity, they are essentially static and assume that the PV module operates under steady-state conditions. Under real operating conditions, charge carriers in the semiconductor layers do not adjust to voltage variations, which leads to transient charge. This dynamic behavior can be represented by an equivalent capacitance across the p–n junction, since the junction stores and releases charge when the voltage changes. As a result, the transient response of a PV cell can be modeled through this capacitive effect, capturing the time-dependent evolution of current and voltage that the static SDM fails to reproduce. In general, the SDM does not include any dynamic elements, which means it cannot capture the transient behavior of a PV module and I–V curve does not reproduce the dynamic characteristics observed in measured waveforms [12–14, 16].

Therefore, dynamic modeling is essential because the real behavior of PV involves time-dependent variations that static models cannot capture. By including capacitive effects, the dynamic model reproduces the actual transient response and offers a clearer understanding of the generators's physical dynamics. This makes it crucial not only for accurate transient simulations but also for real-time monitoring of PV systems. Fig. 1.1 illustrates the dynamic capacitive behavior of the PV junction [9, 11].

In practical operation, a PV generators is connected to a power converter that regulates the operating point through high-frequency switching.

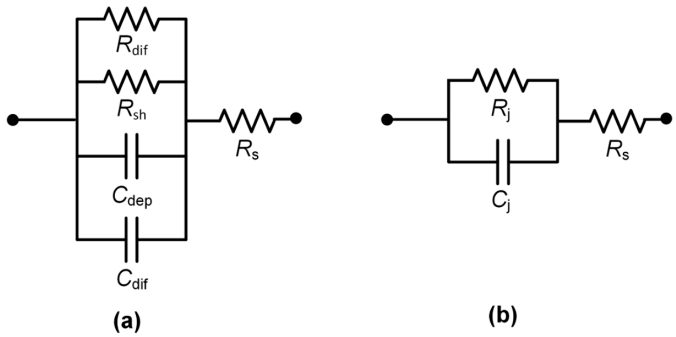

Figure 1.1: Equivalent circuit representations emphasizing the dynamic capacitive behavior of the PV junction. The junction capacitance consists of the depletion (C_{dep}) and diffusion (C_{dif}) components, associated respectively with charge separation in the space-charge region and minority-carrier storage in the quasi-neutral regions.

When the converter introduces a sudden variation in voltage, the internal capacitance stores or releases charge to re-establish equilibrium at the new voltage level. This process takes time and produces a transient response in the waveforms. Therefore, a dynamic modeling framework is required that includes the capacitance effect and represents the PV behavior through an equivalent RC model [9–12]. However, even dynamic models that use a constant capacitance are insufficient to accurately describe the real behavior of PV cells under switching or rapidly changing conditions. At high frequencies, the junction capacitance shows nonlinear, time-dependent characteristics. Consequently, the PV generators cannot be represented accurately by a linear RC model [11]. Therefore, the dynamic effects introduced by this capacitance must be included in the model to achieve accurate parameter identification and enable the effective design of adaptive control strategies [13, 14].

In PV systems, used maximum power point tracking (MPPT) algorithms such as Perturb and Observe (P&O) introduce small voltage perturbations to adjust the operating point of the module [15]. These voltage steps generate continuous ripples in current, effectively exciting the dynamic

behavior of the PV generators. analyzing this dynamic effect is essential not only for accurate modeling but also for diagnosis and condition monitoring of PV systems [14, 16].

By analyzing the transient response produced by these perturbations, valuable information about the internal parameters of the PV module is extracted. This makes the P&O process not only a control mechanism but also a natural source of dynamic data that supports parameter identification and real-time condition monitoring.

Under these conditions, the complexity of the dynamic response introduces challenges for parameter estimation. Data-driven algorithms cannot identify the underlying physical behavior in the data, while physics-based methods are unable to solve highly nonlinear and time-varying differential equations effectively, resulting in limited accuracy. Therefore, a hybrid approach modeling is preferred, as it leverages the strengths of both methods and provides improved accuracy and robustness in parameter identification.

1.2 Possible solutions

To address these challenges, recent advances in computational modeling have introduced hybrid approaches that combine physical understanding with data-driven learning. Among these approaches, Physics-Informed Neural Networks (PINN) have recently emerged as a powerful tool [17]. PINNs combine the governing dynamic equations of the PV system directly into the neural network's learning process, allowing the model to predict hidden parameters and system states while ensuring consistency with physical laws (Fig. 1.2).

The mathematical foundation of PINN is based on automatic differentiation, which enables gradient-based optimization through backpropagation. During training, the network learns a continuous mapping between input and output variables while in parallel minimizing the residuals of the governing dynamic equations. To balance the influence of data-driven learning and physics-based constraints, a weighting coefficient is assigned to each

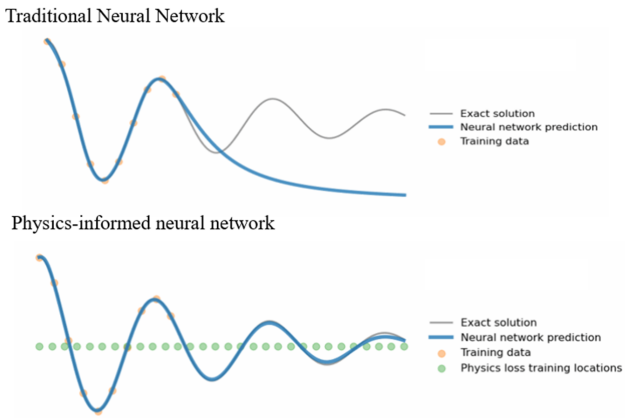

Figure 1.2: The traditional network relies on training data, the PINN incorporates the governing physical equations through additional loss terms (green points), enabling it to generalize more accurately and maintain physical consistency beyond the observed data.

loss component, ensuring that neither term dominates the training process. In this way, the model is guided not only by observed data but also constrained to satisfy the essential physical laws [18]. This hybrid formulation allows PINN to approximate complex, time-dependent, and nonlinear dynamics system with higher accuracy than data-driven or analytical methods [19].

Although the strong theoretical framework of PINN, the methodology remains several challenges when applied to nonlinear, time-dependent PV systems. In photovoltaic modeling, the electrical behavior of the system is determined by parameters related to various material properties, each influencing a particular characteristic. These parameters operate over different ranges under varying environmental conditions, which introduces additional nonlinearity and scaling disparities into the learning process. Therefore, the design of an effective PINN for PV generators requires consideration of both the intrinsic characteristics of each parameter and the influence of external operating conditions to ensure robust and physically consistent estimation. To achieve accurate modeling, the network must be designed in

correspondence with the physical behavior of the system where each governing parameter exhibits nonlinear influence on the current–voltage response. Such alignment between the learning structure of PV enables more stable training, faster convergence, and physically consistent parameter estimation under dynamic operating conditions [20].

Based on these considerations, we developed two novel network architectures specifically designed according to the intrinsic characteristics of photovoltaic systems. These architectures are based on the theoretical framework of PINN and are designed to address the nonlinear time-domain waveform analysis of photovoltaic generators. Unlike most analysis approaches that focus on steady-state analysis or frequency domain analysis, this study introduces two novel PINN-based framework for time-domain analysis of photovoltaic generators. This new analysis enables the network to learn the system's fast transient responses and nonlinear dynamics directly from time-domain waveform, providing a more physically consistent and interpretable representation of the PV behavior.

The discussion on dynamic parameter estimation and the implementation details of the PINN-based dynamic estimation framework are presented and analyzed in depth in next Chapters.

1.3 Objective and outline

The main objective of this study is to develop an novel advanced framework for dynamic modeling and parameter estimation of PV generators based on PINN. As discussed in next chapters, dynamic modeling analysis approaches for PV systems can be classified into two categories: frequency-domain models analysis, and time-domain dynamic models analysis [21–24].

time-domain waveform analysis provides a way to describe how the electrical variables of a PV system change over time. Although this approach effectively captures the dynamic behavior of PV systems, its application in research is still in its early stages [15, 23]. This leads to the following main research objectives:

- If we have the analysis transient during P&O can we use the time respond of the PV modules in P&O?

- Can the time-domain transient response of PV systems be effectively leverage using PINN to extract dynamic information in PV systems and develop novel PINN structure for better accuracy in parameter identification in PV?

- How can a physics-informed learning framework that incorporates the governing dynamics of PV systems enhance the robustness of parameter estimation under noisy conditions through improved model design and cost function formulation?

Overall, Table 1.1 illustrates the methodological evolution of this research from a linear capacitor model to increasingly complex nonlinear. The development of these models highlights the flexibility of PINN in integrating physical principles with data-driven learning and enabling robust estimation of photovoltaic parameters and accurate characterization of transient system dynamics. The first model describes the nonlinear SDM with a linear capacitor, in which the capacitance considered constant and independent of voltage or current variations. This formulation represents as the baseline for dynamic analysis, allowing the estimation of the fundamental parameters through a PINN framwork algorithm.

The subsequent model introduces a nonlinear voltage-dependent capacitor to capture more realistic dynamic behaviors of photovoltaic model. The nonlinear formulation is initially implemented using a PINN and enhanced through a Multiple PINN configuration, where each network focuses on learning a specific subset of paramet-networkpared to the PINN, the novel multiple network PINN approach improves convergency , and enhances the model's ability to capture complex nonlinear relationships between electrical quantities. Also, a more nonlinear model is developed, where the capacitance behavior depends on both voltage and current, and the influence of environmental factors such as temperature and irradiance is also incorporated.

Table 1.1: Overview of the developed models, algorithms, and corresponding dynamic equations

Dynamic Model	**Estimated Parameters**	**Algorithm**	**Type**	**Dynamic Equation**	**Chapter**
SDM with Linear Capacitor [15]	R_{sh}, R_s, C, I_{ph}	PINN	Linear	$C(t) = C$	3
SDM with Nonlinear Capacitor [25]	R_{sh}, R_s, b, I_{ph}	PINN	Nonlinear (voltage-dependent)	$C(v_c(t)) = b \cdot \exp\left(\frac{q v_c(t)}{kT}\right)$	3
SDM with Nonlinear Capacitor [25]	R_{sh}, R_s, b, I_{ph}	Multiple PINN	Nonlinear (voltage-dependent)	$C(v_c(t)) = b \cdot \exp\left(\frac{q v_c(t)}{kT}\right)$	4
SDM with Nonlinear Capacitor [20]	C_j, G, T	Two-level layered PINN	Nonlinear (current & voltage-dependent)	$C(V_{ac}(t), i_{ac}(t)) = \frac{C_{j0}}{\sqrt{1+\frac{(V_{ac}(t)+R_s i_{ac}(t))}{V_j}}}$	5

In general, Chapter 2 presents a comprehensive review of the literature, covering PV modeling techniques, equivalent circuit representations, and parameter identification methods. It also discusses the advantages and limitations of conventional analytical and numerical approaches, along with recent advances in data-driven modeling. Chapter 3 presents the proposed methodology based on PINN. It outlines the modeling framework, network architecture, and training strategy employed to estimate the dynamic PV parameters under both linear and nonlinear configurations. Chapter 4 introduces an novel enhanced PINN structure for PV parameter estimation, developed based on the distinct characteristics and dynamic responses of the parameters. Two parallel PINN networks were designed to better represent system complexity and transient behavior, with each network dedicated to learning specific dynamic features. Chapter 5 presents a novel two-level layered PINN architecture designed to estimate temperature and irradiance, with a strong focus on accurately analyzing transient behavior. This structure enhances the model's ability to capture both environmental

conditions and transient variations analysis. Chapter 6 presents the experimental validation of the proposed approach, demonstrating its practical effectiveness and reliability under real operating conditions. This chapter describes how the experimental setup and measurements were designed to verify the model's ability to accurately estimate PV parameters and reproduce the system's dynamic response. Finally, Chapter 7 concludes the thesis by summarizing the key findings and contributions, highlighting the significance of the proposed dynamic PV modeling framework, and outlining recommendations and future research directions.

References

[1] S. Bilgen, K. Kaygusuz, and A. Sari, "Renewable energy for a clean and sustainable future," *Energy Sources*, vol. 26, no. 12, pp. 1119–1129, 2004.

[2] M. B. Hayat, D. Ali, K. C. Monyake, L. Alagha, and N. Ahmed, "Solar energy—A look into power generation, challenges, and a solar-powered future," *International Journal of Energy Research*, vol. 43, no. 3, pp. 1049–1067, 2019.

[3] R. Ramabadran and B. Mathur, "Effect of shading on series and parallel connected solar PV modules," *Modern Applied Science*, vol. 3, no. 10, pp. 32–41, 2009.

[4] M. T. Chaichan and H. A. Kazem, "Environmental conditions and its effect on PV performance," in *Generating Electricity Using Photovoltaic Solar Plants in Iraq*, Cham: Springer, 2018, pp. 83–129.

[5] W. A. Omran, M. Kazerani, and M. M. A. Salama, "A study of the impacts of power fluctuations generated from large PV systems," in *Proc. IEEE PES/IAS Conf. Sustainable Alternative Energy (SAE)*, 2009, pp. 1–6.

[6] J. W. Zhang *et al.*, "Aging phenomena of backsheet materials of photovoltaic systems for future zero-carbon energy and the improvement pathway," *Journal of Materials Science and Technology*, vol. 153, pp. 106–119, 2023.

[7] K. Hasan *et al.*, "Effects of different environmental and operational factors on the PV performance: A comprehensive review," *Energy Science and Engineering*, vol. 10, no. 2, pp. 656–675, 2022.

[8] I. Polymeropoulos, S. Bezyrgiannidis, E. Vrochidou, and G. A. Papakostas, "Enhancing solar plant efficiency: A review of vision-based

monitoring and fault detection techniques," *Technologies*, vol. 12, no. 10, p. 175, 2024.

[9] van Nijen, D. A., Procel, P., van Swaaij, R. A., Zeman, M., Isabella, O., Manganiello, P. (2025). The nature of silicon PN junction impedance at high frequency. Solar Energy Materials and Solar Cells, 282, 113383.

[10] Hsieh, Y. C., Yu, L. R., Chang, T. C., Liu, W. C., Wu, T. H., Moo, C. S. (2019). Parameter identification of one-diode dynamic equivalent circuit model for photovoltaic panel. IEEE Journal of photovoltaics, 10(1), 219-225.

[11] van Nijen, D. A., Muttillo, M., Van Dyck, R., Poortmans, J., Zeman, M., Isabella, O., Manganiello, P. (2023). Revealing capacitive and inductive effects in modern industrial c-Si photovoltaic cells through impedance spectroscopy. Solar Energy Materials and Solar Cells, 260, 112486.

[12] Bobtsov, A., Mancilla-David, F., Aranovskiy, S., Ortega, R. (2023). Photovoltaic Arrays' Dynamic Model Parameter Estimation. IFAC-PapersOnLine, 56(2), 6845-6850.

[13] Di Piazza, M. C., Luna, M., Vitale, G. (2013). Dynamic PV model parameter identification by least-squares regression. IEEE Journal of Photovoltaics, 3(2), 799-806.

[14] Kim, K. A., Xu, C., Jin, L., Krein, P. T. (2013). A dynamic photovoltaic model incorporating capacitive and reverse-bias characteristics. IEEE Journal of photovoltaics, 3(4), 1334-1341.

[15] N. Femia, G. Petrone, G. Spagnuolo, and M. Vitelli, Power Electronics and Control Techniques for Maximum Energy Harvesting in Photovoltaic Systems. Boca Raton, FL: CRC Press, 2017.

[16] A. Bobtsov, F. Mancilla-David, S. Aranovskiy, and R. Ortega, "Identification of the Photovoltaic Module Dynamic Model via Dynamic Re-

gressor Extension and Mixing," *IEEE Transactions on Control Systems Technology*, 2024.

[17] M. Raissi, P. Perdikaris, and G. E. Karniadakis, "Physics-informed neural networks: A deep learning framework for solving forward and inverse problems involving nonlinear partial differential equations," *Journal of Computational Physics*, vol. 378, pp. 686–707, 2019.

[18] Z. Ren, S. Zhou, D. Liu, and Q. Liu, "Physics-informed neural networks: A review of methodological evolution, theoretical foundations, and interdisciplinary frontiers toward next-generation scientific computing," *Applied Sciences*, vol. 15, no. 14, p. 8092, 2025.

[19] X. Meng, Z. Li, D. Zhang, and G. E. Karniadakis, "PPINN: Parareal physics-informed neural network for time-dependent PDEs," *Computer Methods in Applied Mechanics and Engineering*, vol. 370, p. 113250, 2020.

[20] Shamsmohammadi, N., Spagnuolo, G., del Campo-Ávila, J., Palomo, E. J., Mora-López, L. (2025). Improving Estimation of Parameters in Photovoltaic Models Using Two-Level Layered Physics-Informed Neural Networks. IEEE Journal of Photovoltaics.

[21] A. Ramirez, "Frequency domain modeling of photovoltaic systems for transient analysis," *IEEE Transactions on Power Delivery*, vol. 37, no. 5, pp. 3762–3770, 2021.

[22] A. Bracale, A. J. Collin, M. Ishaq, and R. Langella, "Comparison of frequency domain models for assessing the harmonic emissions of low voltage photovoltaic systems," *IET Renewable Power Generation*, vol. 19, no. 1, p. e13152, 2025.

[23] A. El Aouni, S. E. Naimi, and Y. Ayat, "Machine learning-based photovoltaic power and energy prediction in time–frequency domain," *Electrical Engineering*, pp. 1–12, 2025.

[24] Y. Tang *et al.*, “Impedance Characteristic-Based Frequency-Domain Parameter Identification Method for Photovoltaic Controllers,” *Energies*, vol. 18, no. 12, p. 3118, 2025.

[25] D. A. van Nijen, M. Muttillo, R. Van Dyck, J. Poortmans, M. Zeman, O. Isabella, and P. Manganiello, "Revealing capacitive and inductive effects in modern industrial c-Si photovoltaic cells through impedance spectroscopy," *Solar Energy Materials and Solar Cells*, vol. 260, pp. 112486, Aug. 2023, doi: 10.1016/j.solmat.2023.112486.

Chapter 2

2

Identifying Physical Parameters In Photovoltaic Systems

2.1 Introduction

In order to monitor a PV system effectively, we usually rely on Equivalent Circuit Model (ECM) that describe how the system behaves under different conditions. These models describe the electrical behavior of the system through a set of parameters [1, 2]. To better understand how these models represent the physical behavior of PV systems, we begin by looking at the widely used SDM and how it is formulated in both static and dynamic models, as discussed in the next section.

2.2 Modeling Approaches For PV Systems

One of the most widely used frameworks for PV modeling is the SDM. It captures the electrical behavior of the device and forms the basis for most PV modeling approaches. Depending on the objectives of the analysis, the SDM can be implemented in either a static or dynamic model. The static model describes the steady-state conditions of the PV, while the dynamic extension incorporates transient behavior, allowing the model to reflect the

system's response to time-varying inputs [3].

The following subsection introduces the SDM structure for static and dynamic analysis.

2.2.1 Static Model Approach In PV Systems

Static models assume steady-state operating conditions. The SDM is widely used in this context, as it can accurately reproduce the I–V characteristics of PV modules under static conditions, as illustrated in Figure 2.1.

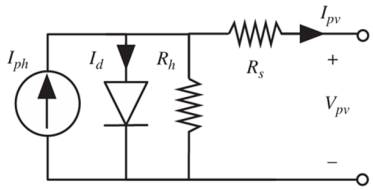

Figure 2.1: Equivalent circuit of the SDM used for static modeling of PV modules.

The SDM represents the PV cell using a current source (I_{ph}), a diode (D), a series resistance (R_s), and a shunt resistance (R_{sh}). The current source I_{ph} models the photo-generated current, while the diode accounts for the behavior of the p–n junction. The series resistance R_s represents ohmic losses in interconnections, and the shunt resistance R_{sh} models leakage currents across the junction [4].

This model is particularly effective for reproducing the I–V characteristic curve, which reflects key performance metrics such as the open-circuit voltage, short-circuit current, and MPP. Analyzing the shape and curvature of the I–V or P–V curves allows for basic fault detection, such as mismatches, degradation, or bypass diode activation [5].

While the SDM can reproduce the steady-state (I–V) characteristics, it inherently neglects the transient dynamics of photovoltaic devices. These static algebraic formulations assume an instantaneous equilibrium between the voltage and current, disregarding the internal charge storage and capacitive behavior of the p–n junction [30, 31]. Under dynamic conditions, the PV system can no longer be represented by a fixed (I–V) curve but instead

behaves as a nonlinear dynamic system in which the junction capacitance governs the charging and discharging processes during voltage and irradiance fluctuations [32–34].

The following subsection examines the dynamic modeling approach in more detail.

2.2.2 Dynamic Model Approach In PV Systems

To address the limitations of static representations, dynamic models extend the SDM framework by incorporating time-dependent elements that capture the transient electrical response of PV modules. In dynamic modeling, additional components are introduced to represent the junction and diffusion charge effects within the semiconductor layers. These elements describe the ability of the p–n junction to store and release charge in response to voltage perturbations, allowing the model to simulate how the current and voltage evolve over time under dynamic operating conditions [30, 31]. A typical dynamic extension of the SDM therefore includes a capacitance connected in parallel replaced the diode, as shown in Figure 2.2 [32, 33].

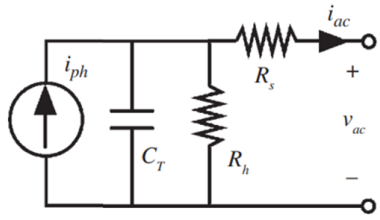

Figure 2.2: Equivalent dynamic model of a PV module including junction capacitance.

The inclusion of the junction capacitance enables the model to reproduce transient behaviors such as overshoot, delay, and relaxation phenomena that arise when the module is subjected to rapid voltage or irradiance variations. It also provides a more accurate representation of the displacement current generated during switching events in power converters, which the static model completely neglects [33, 34].

According to the literature, several analytical approaches have been

proposed to study these dynamic effects, In general categorized into time-domain and frequency-domain analyses [30–32]. The time-domain approach focuses on the transient response of current and voltage to step perturbations, providing information about the system's dynamic parameters and transiant behavior. On the other hand, the frequency-domain approach often based on impedance spectroscopy examines how the module responds to small-signal variations across different frequencies, revealing charge transport characteristics and capacitive behavior.

In the following subsection, both approaches are examined in detail to better understand and quantify the dynamic characteristics of the proposed model.

2.2.2.1 Frequency Domain Approach

The frequency domain analysis approach is a method for analyzing the dynamic behavior of PV modules. Techniques such as Impedance Spectroscopy (IS) are widely used in this context [8].

As demonstrated in the literature, the dynamic impedance response of the PV module reveals crucial insights into its operating point. For example in [9], By analyzing the frequency response of the module, the authors extract parameters related to charge transport and recombination using an equivalent circuit. The key strength lies in the ability of IS to reveal internal dynamic behaviors not visible through static I–V measurements. However, the method is highly sensitive to measurement conditions and requires precise excitation and noise-free data to ensure reliable parameter extraction. in the other sudy [10], the authors emulate the behavior of a full c-Si PV module under healthy, partially shaded, and faulted conditions. A key strength of this work is the identification of the Nyquist spectrum shape and radius as indicators of fault presence, which allows for fault detection even when I–V curves appear unaffected. However, the study is based solely on simulation data, and no experimental validation is provided, which limits its practical applicability in real-world environments.

In some studies, both static and dynamic characteristics of PV modules are combined to enable more accurate and robust modeling approaches. For example in [11], IS is used to characterize the dynamic behavior of PV modules by analyzing their frequency response through a Constant Phase Element (CPE)-based model. A key strength in this study is the joint optimization of static and dynamic parameters, ensuring consistency across models. However, the approach is sensitive to measurement quality, and independent fitting can lead to inconsistent parameter values. Similarly, [12] proposes an enhanced SDM model incorporating dynamic diode behavior for PV cell characterization using IS. By extracting both IV and impedance data at several operating points and using evolutionary algorithms for parameter fitting, the method achieves accurate replication of both static and dynamic responses. A major strength is the ability to predict the PV cell's impedance and IV curve from a single spectral measurement, significantly reducing testing time. Nevertheless, the model is only validated on single cell experiments under controlled conditions, which limits its generalizability to full PV modules or real-world scenarios. In other study [13], presents an approach for the dynamic characterization of photovoltaic modules by enabling simultaneous I–V curve measurement and impedance spectroscopy analysis. The proposed tool evaluates the module's frequency response across a wide range, allowing the identification of junction capacitance and degradation effects. Its main strength in the in-situ integration with PV strings and the extraction of dynamic parameters directly from experimental data. However, the study reports measurement limitations at very low and high frequencies due to long acquisition times and noise effects. Also in [35], they estimates the electrical parameters of silicon solar cells using IS to analyze their frequency-dependent response and identify degradation mechanisms such as Potential-Induced Degradation (PID) and Current-Induced Degradation (CID). The method provides a reliable approach for distinguishing between different degradation mechanisms and validating physical models. The main strengths are its accuracy, physical interpretation, and ability to separate degradation types, while the weaknesses include dependence on

complex measurement setups, long frequency sweeps, and sensitivity to initial fitting conditions. Also traditional IS is often not sufficient for fast or real-time characterization of photovoltaic devices due to its long measurement time. for example, [36] characterizes silicon photovoltaic cells using Broadband Impedance Spectroscopy (BIS) as a faster alternative to traditional IS. It applies an optimized quasi-logarithmic multisine signal to estimate the impedance response and fits the data to an equivalent circuit model using complex nonlinear least squares to extract parameters. The method reduces acquisition time to about one second while maintaining high accuracy, enabling real-time condition monitoring of PV modules. Strengths include speed, accuracy, and suitability for online monitoring, while weaknesses involve dependence on careful signal optimization, limited frequency range, and sensitivity to noise in practical applications. Also [37] establishes the theoretical foundation of IS for dye-sensitized solar cells (DSSC) by introducing the concepts of chemical capacitance and recombination resistance. This work's strength lies in its physical interpretation of charge transport and recombination, while its limitation is that the model cannot describe multilayer or disordered systems.

In general, this approach offers valuable insights into the dynamic behavior of PV modules. However, this method often requires complex processing and instrumentation and is typically limited to a fixed operating point, where the system is linearized around its steady-state condition and analyzed in the frequency domain using a small-signal model. this analysis provides information about local dynamics but not fully capture the nonlinear behavior of the system. To address these limitations, time-domain analysis offers a complementary perspective by capturing transient and nonlinear behaviors under dynamically changing inputs, which will be explored in the following subsection.

2.2.2.2 Time Domain Approach

Unlike the frequency domain, the time domain monitors transitions and variations and offers a more detailed view of the system's full range of behavior. It is especially useful in situations where the system's performance changes under different conditions and provides more accurate and relevant diagnostic information [14]. This is particularly important in MPPT algorithms such as P&O, where the system continuously perturbs the operating voltage and observes the resulting power variation [1].

This dynamic behavior is clearly illustrated in Fig. 2.3(a), where successive perturbations in the operating voltage (ΔV_{PV}) are applied, and the corresponding changes in power are observed [1]. The points from X_1 to X_{k+1} show how the P&O algorithm moves step by step toward the MPP by checking how the power changes with each voltage adjustment. When the system operates on the rising side of the P–V curve, increasing the voltage results in higher power, so the algorithm continues in the same direction. On the falling side, the same change leads to a drop in power causing the algorithm to reverse its direction. This behavior is illustrated in Fig. 2.3(b), which shows how the normalized PV voltage and the perturbation waveform change over time. The constant step size (Δx) and the fixed time interval (T_p) reflect a discrete-time control approach that depends on tracking short-term system responses to guide the MPPT process effectively.

To further understand how the PV system dynamically reacts to perturbations, Figure. 2.4 presents the step response of the system in the time domain. Figure. 2.4 shows the normalized voltage and power oscillations following a sudden change in operating conditions. The transient behavior is characterized by damped oscillations, where both voltage and power gradually settle to steady-state values. The voltage typically stabilizes faster than the power, as indicated by the shorter settling time. This information is essential for selecting appropriate perturbation intervals and step sizes in MPPT algorithms, ensuring that each perturbation is applied only after the system has sufficiently responded to the previous one.

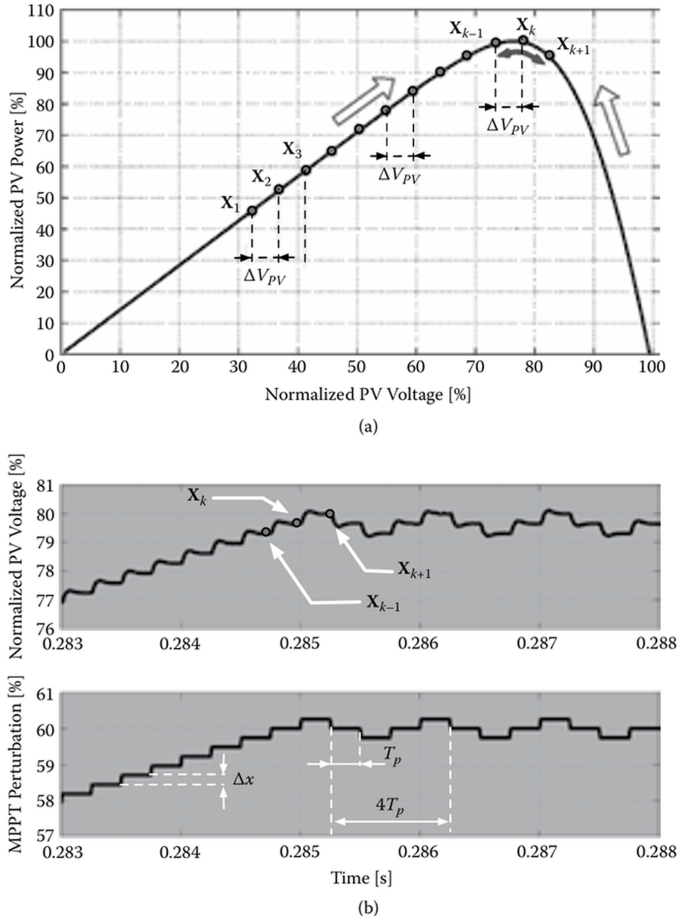

Figure 2.3: Time-domain analysis of the P&O algorithm during the MPPT process. (a) Sequence of voltage perturbations and corresponding power responses on the P–V curve, illustrating the algorithm's progression toward the MPP. (b) Evolution of the normalized PV voltage and the perturbation signal over time, highlighting the discrete control steps and sampling intervals.

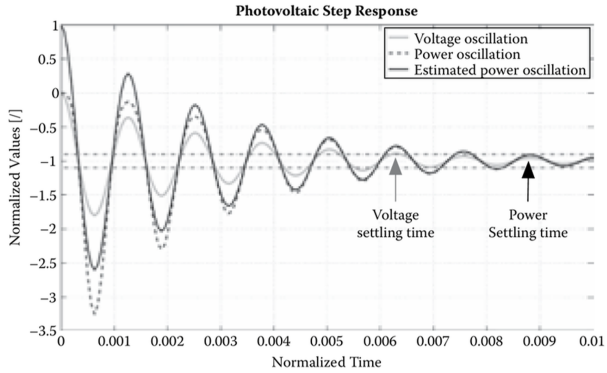

Figure 2.4: Step response of the photovoltaic system showing normalized voltage and power oscillations. The difference in settling times illustrates the dynamic characteristics of the system under a sudden change in operating voltage.

The dynamic response of the PV system is considered as a key factor in improving MPPT performance.

The next section focuses on the general problem of parameter identification parameters using transient analysis. It explains how system parameters can change during dynamic or non-steady-state conditions and discusses techniques that utilize transient responses to accurately estimate these variations.

2.3 Parameter Estimation Using Transient Response Analysis

Transient response analysis is widely applied across various different applications to identify system parameters. By analyzing how a system reacts to time-varying excitations, researchers can extract accurate physical characteristics that are often difficult to obtain under steady-state conditions.

In mechanical systems, when a sudden excitation is applied, the transient response is analyzed to extract parameters of the structure. For example, in rotating machinery, transient resonance crossings are especially

critical because vibration amplitudes and phase relationships change rapidly with rotational speed, requiring advanced modeling and estimation techniques. [38] presents a method to identify the vibration parameters of turbomachinery blades under transient conditions during run-up and run-down. The method employs an analytical single-degree-of-freedom model excited by a harmonic force with a linearly time-varying frequency, meaning the excitation frequency changes linearly with time. The transient response, which exhibits beating behavior after passing through resonance, is analytically approximated and then fitted to Blade Tip-Timing (BTT) data using nonlinear least-squares optimization to estimate the natural frequency and damping ratio. Validation with both numerical and experimental data demonstrates that the transient model provides much higher accuracy than the steady-state approach, particularly in damping estimation, while its main limitation lies in the need for good initial guesses and slower convergence due to nonlinear fitting. Similarly, [39] develops a Prony model–based method for analyzing transient vibration signals to diagnose machinery faults, especially in low-speed rolling element bearings. The method fits exponentially decaying sinusoids to short transient data segments and extracts parameters such as damping and frequency to evaluate fault severity. Using nonlinear least-squares and spectral analysis, the authors establish a quantitative relationship between vibration energy and fault size. The approach achieves high accuracy and efficiency in short transient signal analysis, though its validation is limited and requires further studies to generalize the empirical constants across different machines.

In thermal systems, transient temperature variations following a heat pulse are analyzed to estimate material properties such as thermal conductivity and heat capacity. [40] proposes a two-step parameter estimation procedure (TSPEP) to determine soil and grout thermal properties from thermal response test (TRT) data using transient analysis. A three-dimensional finite element model of a geothermal heat exchanger is combined with nonlinear least-squares optimization using a Gauss linearization approach. The first step estimates grout parameters using early transient data, while the second

step identifies soil parameters from later-time data. The method achieves high accuracy and successfully decouples soil and grout effects, although it is computationally intensive and sensitive to initial guesses and data selection. Also, [41] presents a transient-based inverse analysis to estimate thermal contact resistance (TCR) at solid–solid interfaces using measured temperature responses. A one-dimensional transient heat conduction model is solved numerically, and the TCR is determined via nonlinear least-squares fitting. Results indicate that transient data enhance sensitivity to resistance variations compared to steady-state approaches. This method shows strong accuracy and stability but is sensitive to boundary conditions and measurement noise. Another study [42], applies transient-based parameter estimation to determine both thermal conductivity and heat capacity of the ground using TRT data. By modeling the borehole heat exchanger as a cylindrical heat source and solving transient heat diffusion through finite differences, the authors fit measured outlet temperatures to simulated results using nonlinear least squares. The method provides more detailed physical insights than steady-state line-source models but is limited by computational demand and simplified assumptions.

Transient analysis also finds applications in chemical process systems, where the transient response of concentration or temperature after a sudden input change is used to estimate kinetic and mass transfer coefficients. For instance, [43] presents a model-based design of transient flow experiments (MBDoE) for high-precision estimation of kinetic parameters in chemical reactions. The study employs transient ramping of flowrate and temperature in a plug-flow reactor modeled as a sequence of batch reactors, using maximum likelihood estimation with Fisher Information analysis to identify Arrhenius parameters. The optimized design achieves higher accuracy and reduced experimental time compared to steady-state testing, though it depends on reliable initial guesses and faces computational challenges due to nonlinear optimization.

In electromechanical systems, the transient response of motor speed or acceleration after applying a step torque provides key information about

inertia and friction. [44] introduces an analytical approach to estimate mechanical parameters of induction machines using transient response analysis. The machine is modeled with a fifth-order d–q axis system, focusing on the transient behavior of reactive power with respect to voltage. Using rise and settling times from the transient response, the moment of inertia and damping coefficient are identified iteratively, achieving strong agreement with experimental data. The main advantages are analytical clarity and validation across multiple machine ratings, while weaknesses include computational cost and sensitivity to the initial parameter range. Similarly, [45] analyzes transient stator currents during motor startup to estimate resistance, reactance, and inertia. Among three proposed identification methods, the generalized iterative approach achieves the best performance by minimizing time-domain current errors, demonstrating high accuracy and adaptability to real operating conditions but at the cost of higher computation and sensitivity to nonlinear effects like magnetic saturation. In the same context, [46] applies transient voltage and current analysis to estimate parameters of synchronous machines during startup and load variations. Using nonlinear least-squares fitting of transient waveforms, the authors accurately identify synchronous reactance, damping, and time constants, showing high precision and practical applicability but sensitivity to noise and initial estimates.

Transient analysis is also used in fluid and structural systems. [47] develops a Bayesian inverse transient framework to assess pipeline conditions and estimate parameters such as impedance and wall thickness. Using the Differential Evolution Adaptive Metropolis (DREAM) algorithm, a Markov Chain Monte Carlo (MCMC) method, the approach estimates parameters and their uncertainties from transient pressure data. The method demonstrates strong robustness and uncertainty quantification but requires high computational resources and accurate priors. In electrical systems, [48] applies transient analysis for transformer parameter identification using voltage and current data during energization. A detailed electromagnetic transient model captures inrush current and flux dynamics, while nonlinear least-squares fitting is used to estimate parameters such as winding resistance

and leakage inductance. The method provides physically meaningful results with high accuracy but is computationally expensive and sensitive to measurement noise.

In aerospace applications, transient response analysis is used to model and identify nonlinear aerodynamic behavior during unsteady flight conditions. Reference [49] estimates aerodynamic parameters of aircraft during near-stall maneuvers by analyzing transient flight data. A hybrid neural–artificial bee colony (NABC) method captures the nonlinear transient dynamics of aerodynamic forces and moments during rapid angle-of-attack changes. This approach improves estimation accuracy of lift, drag, and pitching moment coefficients compared to steady-state models but requires high-quality transient data and involves considerable computational effort.

Also, in electrochemical systems, transient analysis has been extensively applied for battery parameter identification. [51] proposes a transient analysis method to estimate parameters such as internal resistance and diffusion capacitance from voltage and current response data following a current pulse. By fitting the voltage relaxation curve through nonlinear optimization, both fast and slow dynamic behaviors are captured effectively. Similarly, [50] estimates lithium-ion battery parameters from short pulse current tests using a simplified equivalent circuit model. The transient voltage response is analyzed to determine internal resistance, charge transfer resistance, and diffusion capacitance with high speed and accuracy, making the method suitable for online applications despite sensitivity to temperature and model simplifications.

Overall, these studies use physics-based or data-driven methods for transient response analysis and parameter estimation. A hybrid framework allows for both physical consistency and improved predictive performance. The next section introduces a hybrid approach that integrates these two perspectives to achieve more accurate and robust transient parameter estimation.

2.4 Physics-Informed neural network

To address the limitations of both methods, a hybrid approache have emerged that integrate physical knowledge with data-driven learning. PINN represent an innovative approach to this task [15]. They are especially efficient when noisy or insufficient data are available for the dynamic system to identify. In a PINN, the physical laws of the system are used as part of the cost function of the neural network so that the network learns through training not only the data but also the physical laws governing the system. By embedding physics into the training process, PINN can extract hidden dynamics from limited or noisy data. This makes them especially useful in nonlinear or time-dependent systems. they use physics as a guiding principle to regularize the learning process, reducing the risk of overfitting and improving generalization [16]. Also, PINN do not require traditional labeled training data as in supervised learning. Instead, they leverage physics-based loss functions derived from governing differential equations to learn the underlying system behavior. By embedding these physical constraints directly into the neural network, PINN ensure that their solutions inherently satisfy the fundamental laws governing the system [17].

Based on these features, PINN can be employed effectively for system identification, particularly in time-dependent applications where the capture of dynamic behavior is essential. A comprehensive comparison between classical methods, physics-based optimization approaches, and physics-informed neural networks (PINNs) is summarized in Table 2.1. The table highlights the main characteristics, advantages, and limitations of each category, providing a clear overview of their respective strengths and weaknesses in time-domain parametric identification.

In the following section, we explain how PINN applied to the identification of the system in the time domain.

Table 2.1: Comparison of data-driven, physics-based, and physics-informed (PINN) approaches for system identification

Aspect	**Data-driven methods**	**Physics-based methods**	**PINNs (hybrid)**
Core idea	Learn directly from data	Use governing physical equations	Combine data with physical constraints
Strengths	Learn complex nonlinear patterns	Based on physical principles	Robust to noise
Weaknesses	Lack physical constraints; poor extrapolation	Limit applicability to nonlinear or uncertain systems	High computational cost
Data requirement	Large datasets	Minimal data and rely on equations	Effective with limited and noisy data
Physical consistency	Lack physical consistency	Fully consistent with physics	Enforce physics through loss terms
Typical application	Complex systems with large datasets	Well-defined physical systems	Nonlinear or data-limited systems

2.5 Physics-Informed Neural Network As Parametric Identification Tools

In parameter estimation with PINN, factors such as noise level, number of parameters, model complexity, and system behavior influence the accuracy and robustness of the estimation. Nonlinear models typically exhibit greater complexity compared to linear models and often require a larger amount of input data to accurately estimate parameters and capture the underlying dynamics of the system. For example, in [18], the researchers started by modeling a linear elasticity problem. This initial linear model served as a foundational step to explore the PINN behavior and performance of the PINN framework network. For this linear model, they used 100 input data points to estimate two parameters. When extending to a more complex nonlinear problem, they estimated three parameters using 2000 input data points. Additionally, the dimensionality of the model is critically important. In [15], the researchers investigated the Navier–Stokes equation and the Korteweg–de Vries (KdV) equation, highlighting the influence of dimensionality on model complexity. The Navier–Stokes equation,

which models incompressible fluid flow in two dimensions (2D), requires solving for multiple variables across a complex, high-dimensional space. Due to the intricate nature of fluid dynamics and the high dimensionality involved, more parameters are necessary to accurately capture the spatial variations and interactions within the flow field. In this case, 5000 input data points were used to estimate two parameters. In contrast, the KdV equation is a simpler, one-dimensional (1D) equation that models wave propagation in shallow water or similar systems. Because of its lower complexity and dimensionality, significantly fewer parameters and data points are needed. The study used 199 and 200 samples to estimate two parameters at two different time points, t_n and t_{n+1}, within the KdV equation. This comparison underscores how the dimensionality and complexity of the equations directly impact the amount of data required and the number of parameters needed to accurately model these systems within the PINN framework. Also, to address the limitations of slow convergence and difficulties in handling stiffness and nonlinear behavior, various enhanced versions of PINN have been introduced in recent studies. For example, Coupled automatic-numerical automatic–numerical differentiation PINNs (CAN-PINN) combines automatic and numerical differentiation to improve training speed and stability, particularly under sparse data. It outperforms classical PINN in terms of accuracy and efficiency but depends on manually tuned differentiation parameters and may not scale well in complex geometries or noisy environments [19]. transform higher-order PDEs into first-order systems, enabling training with only first-order derivatives and exact enforcement of boundary conditions using . This results faster training and higher accuracy for high-order and parameterized problems, although the additional compatibility constraints can complicate training and affect convergence [20].

In addition to advancements in network architectures and differentiation strategies, recent efforts have increasingly focused on improving the design of physics-based loss functions in PINN. For instance, [21] introduces a neural network that learns the discrepancy between the assumed physical model and observed data. This approach allows for the simultaneous

minimization of data and physics losses, and supports uncertainty quantification through ensemble or Bayesian PINN frameworks. While this method improves robustness and adaptability in the presence of model errors, it also increases computational demands. Similarly, the Multiaxial fatigue life prediction physics-informed neural network (MFLP-PINN) framework incorporates material-specific physical behavior directly into the loss function to enhance prediction accuracy. However, its effectiveness largely depends on selecting a suitable physical model for the material. If the model's assumptions do not reflect the true behavior of the system, the quality of the predictions can deteriorate noticeably [22].

Moreover, the type of sampling method employed can significantly enhance the effectiveness of parameter estimation. For instance, in [23], the researchers utilized 30 samples to estimate five parameters by employing a Uniform Design sampling strategy [24]. This approach optimizes the number of samples by uniformly distributing them across the multivariate space, enabling the comprehensive capture of the design space with fewer samples. Consequently, Uniform Design facilitates a complete representation of the design space while maintaining the quality and accuracy of the analysis with a reduced number of samples.

Considering these characteristics, PINN have shown great potential as a suitable approach for parameter estimation in nonlinear, data-limited, and time-domain environments.

These advantages make them particularly attractive for applications in power systems, which will be explored in the following section.

2.6 Applications of Physics Informed Neural Network in Power Systems

In recent years, PINN have emerged as a powerful and innovative approach for modeling, analysis, and control of power systems and power electronics. For example, in [25], a PINN-based approach enables simultaneous

estimation of dynamic states and system parameters in power generators using limited Phasor measurement unit (PMU) data. The method incorporates differential equations as physical constraints during training. Its strengths include robustness to noisy data and the ability to estimate multiple variables concurrently. However, it relies on accurate physical models, requires careful hyperparameter tuning, and involves high computational costs for complex systems. Also, [26] presents a novel Physics-Informed Graph Neural Network (PIGNN) methodology that enables accurate state estimation in power systems. Key strengths include robustness to noise, reduced dependency on labeled data, and strong generalization capability. However, the method relies on accurate network topology, involves complex implementation, and lacks wide validation on real-world power systems.

One of the main challenges in parameter estimation of power electronic converters is the limited availability of measurement data and the need for accurate modeling. In [27], a novel method estimates the parameters of a Buck converter using Physics-Informed Machine Learnin (PIML). By leveraging PINN and peak-to-peak voltage and current data, this approach achieves high estimation accuracy without requiring disturbance injection. However, a notable weakness remains the lack of a systematic approach to determine the optimal weighting between the physical model and data terms in the loss function.

Accurate parameter estimation in power systems is challenged by measurement noise such as Gaussian, additiv (AD), and synchronization (sync), originating from sensors and environmental factors. In [28], the effect of different noises from 5% to 20% and input data ranging from 20 to 1000 samples on one parameter was studied. However, its limitations include high computational costs associated with hyperparameter tuning and training, as well as challenges in scaling the model for broader operating conditions. In [29], researchers addressed this complexity by incorporating three types of noise. Additionally, the neural network weights were initialized using the Xavier initialization method, which sets the weights in a random yet controlled manner at the onset of training. This initialization strategy enhances model

convergence and prevents issues like vanishing or exploding gradients. Furthermore, the circuit parameters were initialized with specific initial values, serving as starting points for model optimization and learning. The definition of lower and upper bounds for the inputs also played a crucial role in normalizing the data, thereby enabling the model to process the information more effectively and accurately. These capabilities are particularly valuable in PV systems, where environmental variability and system complexity pose significant challenges.

Because PINN has already been applied to problems involving nonlinear differential equations and for identifying a number of complex physical parameters across various domains such as fluid dynamics, heat transfer, and electromechanical systems, it provides a promising foundation for modeling highly nonlinear processes. Its ability to incorporate governing equations directly into the learning process enables simultaneous data fitting and physical constraint enforcement, resulting in improved generalization and physical consistency.

In general, this chapter provided an in-depth analysis of PV modeling approaches, including a detailed comparison between static and dynamic representations of PV modules. It also reviewed different parameter identification methods in the time domain and their limitations under nonlinear and noisy conditions. In addition, the chapter introduced PINN as an alternative approach for parameter estimation. The dynamic SDM was presented as the main dynamic modeling framework for transient analysis. This analysis provided the motivation for using physics-informed learning in dynamic PV modeling. Given these advantages, the next chapter focuses on employing the PINN framework for the dynamic analysis of PV systems, demonstrating its capability to model transient behavior and accurately estimate system parameters under varying operating conditions.

References

[1] N. Femia, G. Petrone, G. Spagnuolo, and M. Vitelli, *Power Electronics and Control Techniques for Maximum Energy Harvesting in Photovoltaic Systems*. Boca Raton, FL, USA: CRC Press, 2017.

[2] R. Ahmad, A. F. Murtaza, and H. A. Sher, "Power tracking techniques for efficient operation of photovoltaic array in solar applications – A review," *Renewable and Sustainable Energy Reviews*, vol. 101, pp. 82–102, 2019.

[3] G. Petrone, C. A. Ramos-Paja, and G. Spagnuolo, Photovoltaic Sources Modeling. Wiley, 1st ed., Jan. 2017. doi: 10.1002/9781118755877.

[4] E. I. Batzelis, "Simple PV performance equations theoretically well founded on the single-diode model," *IEEE Journal of Photovoltaics*, vol. 7, no. 5, pp. 1400–1409, 2017.

[5] M. A. Abdullah, A. H. M. Yatim, C. W. Tan, and R. Saidur, "A review of maximum power point tracking algorithms for wind energy systems," *Renewable and Sustainable Energy Reviews*, vol. 16, no. 5, pp. 3220–3227, 2012.

[6] C. Pavón-Vargas, L. E. Garcia-Marrero, J. D. Bastidas-Rodríguez, R. A. Guejia-Burbano, and G. Petrone, "Experimental assessment of partial shading detection in PV panels using impedance spectroscopy," *IEEE Transactions on Industry Applications*, vol. 61, no. 5, pp. 7584–7597, Sep.–Oct. 2025, doi: 10.1109/TIA.2025.3561708.

[7] N. Shamsmohammadi and G. Spagnuolo, "Parametric identification of the dynamic photovoltaic model by a physics-informed neural network," *2025 International Conference on Clean Electrical Power (ICCEP)*, Villasimius, Italy, 2025, pp. 195–200, doi: 10.1109/ICCEP65222.2025.11143684.

[8] R. A. Guejia-Burbano and G. Petrone, "Partial shading detection on PV panels through on-line Impedance Spectroscopy," in IEEE International Conference on Environment and Electrical Engineering and 2021 IEEE Industrial and Commercial Power Systems Europe (EEEIC/I&CPS Europe), ZUZL, pp. 1–0, doi: 10.1109/EEEIC/ICPSEurope51590.2021.9584621.

[9] L. E. G. Marrero, R. A. Guejia-Burbano, G. Petrone, M. Piliougine, and E. Monmasson, "Identification of static and dynamic parameters of PV models through multi-objective optimization," *2023 IEEE 17th International Conference on Compatibility, Power Electronics and Power Engineering (CPE-POWERENG)*, Tallinn, Estonia, 2023, pp. 1–6, doi: 10.1109/CPE-POWERENG58103.2023.10227400.

[10] M. De Riso, I. Matacena, P. Guerriero, S. Daliento, L. E. Garcia Marrero, and G. Petrone, "Dynamic modeling of Si-based photovoltaic modules using impedance spectroscopy technique," *2023 International Conference on Clean Electrical Power (ICCEP)*, Terrasini, Italy, 2023, pp. 430–435, doi: 10.1109/ICCEP57914.2023.10247369.

[11] L. E. Garcia-Marrero, C. Pavón-Vargas, G. Petrone, and E. Monmasson, "Advancements in photovoltaic research: Electro-impedance spectroscopy for PV cell characterization," *2024 International Symposium on Power Electronics, Electrical Drives, Automation and Motion (SPEEDAM)*, 2024, pp. 776–781, doi: 10.1109/SPEEDAM61530.2024.10609231.

[12] M. De Riso, I. Matacena, S. Daliento, and P. Guerriero, "Impedance spectroscopy as on-field monitoring technique for PV modules," *2024 19th Conference on Ph.D. Research in Microelectronics and Electronics (PRIME)*, 2024, pp. 1–6, doi: 10.1109/PRIME61930.2024.10559699.

[13] M. De Riso, P. Guerriero, I. Matacena, and S. Daliento, "A tool providing IV curve and IS analysis of a PV module embedded in a string,"

2023 8th International Conference on Smart and Sustainable Technologies (SpliTech), Split, Croatia, Jun. 2023, pp. 1–6, doi: 10.23919/SpliTech58133.2023.10308942.

[14] M. Liu, X. Cao, L. Wang, J. Fan, Y. Xu, and Z. Zhang, "Characterizing photovoltaic module power degradation through impedance spectroscopy: Transitioning to outdoor applications," *Renewable Energy*, p. 123438, 2025, doi: 10.1016/j.renene.2025.123438.

[15] M. Raissi, P. Perdikaris, and G. E. Karniadakis, "Physics-informed neural networks: A deep learning framework for solving forward and inverse problems involving nonlinear partial differential equations," *Journal of Computational Physics*, vol. 378, pp. 686–707, 2019.

[16] M. A. Nabian, R. J. Gladstone, and H. Meidani, "Efficient training of physics-informed neural networks via importance sampling," *Computer-Aided Civil and Infrastructure Engineering*, vol. 36, no. 8, pp. 962–977, 2021.

[17] S. Monaco and D. Apiletti, "Training physics-informed neural networks: One learning to rule them all?," *Results in Engineering*, vol. 18, p. 101023, 2023.

[18] E. Haghighat, M. Raissi, A. Moure, H. Gomez, and R. Juanes, "A physics-informed deep learning framework for inversion and surrogate modeling in solid mechanics," *Computer Methods in Applied Mechanics and Engineering*, vol. 379, p. 113741, 2021.

[19] P.-H. Chiu, J. C. Wong, C. Ooi, M. H. Dao, and Y.-S. Ong, "CAN-PINN: A fast physics-informed neural network based on coupled-automatic–numerical differentiation method," *Computer Methods in Applied Mechanics and Engineering*, vol. 395, p. 114909, 2022.

[20] R. J. Gladstone, M. A. Nabian, N. Sukumar, A. Srivastava, and H. Meidani, "FO-PINN: A First-Order formulation for Physics-Informed Neural

Networks," *Engineering Analysis with Boundary Elements*, vol. 174, p. 106161, 2025.

[21] S. Kissas, Y. Yang, E. W. Savage, W. R. Longland III, T. P. Hoang, and Y. A. G. Marquez, "Learned physics-informed neural networks for data-efficient and interpretable modeling of physics-based systems," *Computer Methods in Applied Mechanics and Engineering*, vol. 419, p. 116945, 2023.

[22] G. He, Y. Zhao, and C. Yan, "MFLP-PINN: A physics-informed neural network for multiaxial fatigue life prediction," *European Journal of Mechanics - A/Solids*, vol. 98, p. 104889, 2023.

[23] A. Habib, A. A. Houri, M. T. Junaid, and S. Barakat, "A systematic and bibliometric review on physics-based neural networks applications as a solution for structural engineering partial differential equations," *Structures*, vol. 69, p. 107361, Nov. 2024, Elsevier.

[24] K.-T. Fang, D. K. J. Lin, P. Winker, and Y. Zhang, "Uniform design: theory and application," *Technometrics*, vol. 42, no. 3, pp. 237–248, 2000.

[25] A. Kendall, Y. Gal, and R. Cipolla, "Multi-task learning using uncertainty to weigh losses for scene geometry and semantics," in *Proc. IEEE Conf. Computer Vision and Pattern Recognition (CVPR)*, Salt Lake City, UT, USA, 2018, pp. 7482–7491.

[26] Z. Huang and Y. Wang, "Applications of Physics-Informed Neural Networks in Power Systems – A Review," *IEEE Transactions on Power Systems*, vol. 38, no. 1, pp. 566–582, Jan. 2023.

[27] S. I. Ngo and Y.-I. Lim, "Solution and Parameter Identification of a Fixed-Bed Reactor Model for Catalytic CO_2 Methanation Using Physics-Informed Neural Networks," *Catalysts*, vol. 11, no. 1304, pp. 1–20, 2021.

[28] S. Zhao, Y. Peng, Y. Zhang, and H. Wang, "Parameter Estimation of Power Electronic Converters With Physics-Informed Machine Learning," *IEEE Transactions on Power Electronics*, vol. 37, no. 10, pp. 11567–11578, Oct. 2022.

[29] X.-Y. Guo and S.-E. Fang, "Structural parameter identification using physics-informed neural networks," *Measurement*, vol. 220, p. 113334, 2023.

[30] A. Bobtsov, F. Mancilla-David, S. Aranovskiy, and R. Ortega, "Identification of the Photovoltaic Module Dynamic Model via Dynamic Regressor Extension and Mixing," *IEEE Transactions on Control Systems Technology*, 2024.

[31] A. Bobtsov, F. Mancilla-David, S. Aranovskiy, and R. Ortega, "Photovoltaic Arrays' Dynamic Model Parameter Estimation," *IFAC PapersOnLine*, vol. 56, no. 2, pp. 6845–6850, 2023.

[32] M. C. Di Piazza, M. Luna, and G. Vitale, "Dynamic PV Model Parameter Identification by Least-Squares Regression," *IEEE Journal of Photovoltaics*, vol. 3, no. 2, pp. 799–806, Apr. 2013.

[33] K. A. Kim, C. Xu, L. Jin, and P. T. Krein, "A Dynamic Photovoltaic Model Incorporating Capacitive and Reverse-Bias Characteristics," *IEEE Journal of Photovoltaics*, vol. 3, no. 4, pp. 1334–1340, Oct. 2013.

[34] R. A. Guejia-Burbano, G. Petrone, and M. Piliougine, "Impedance Spectroscopy for Diagnosis of Photovoltaic Modules Under Outdoor Conditions," *IEEE Journal of Photovoltaics*, vol. 12, no. 6, pp. 1503–1511, 2022.

[35] T. Yeow, J. Sun, Z. Yao, J.-N. Jaubert, and K. P. Musselman, "Evaluation of impedance spectroscopy as a tool to characterize degradation mechanisms in silicon photovoltaics," *Solar Energy*, vol. 184, pp. 52–58, 2019.

[36] A. De Riso, G. Petrone, G. Spagnuolo, and M. Vitelli, "A tool providing I–V curve and IS analysis of a PV module embedded in a string," *Solar Energy*, vol. 275, p. 118625, 2025.

[37] S. Wang, P. Kaienburg, B. Klingebiel, D. Schillings, and T. Kirchartz, "Understanding thermal admittance spectroscopy in low-mobility semiconductors," *Journal of Physical Chemistry C*, vol. 122, no. 17, pp. 9795–9803, 2018.

[38] B. Cauberghe, P. Guillaume, P. Verboven, and E. Parloo, "Identification of modal parameters including unmeasured forces and transient effects," *Journal of Sound and Vibration*, vol. 265, no. 3, pp. 609–625, 2003.

[39] F. Bozzoli, G. Pagliarini, S. Rainieri, and L. Schiavi, "Estimation of soil and grout thermal properties through a TSPEP (two-step parameter estimation procedure) applied to TRT data," *Energy*, vol. 36, no. 2, pp. 839–846, 2011.

[40] S. Bornassi, T. M. Berruti, C. M. Firrone, and G. Battiato, "Vibration parameters identification of turbomachinery rotor blades under transient condition using Blade Tip-Timing measurements," *Measurement*, vol. 183, p. 109861, 2021.

[41] Z. Chen and C. K. Mechefske, "Diagnosis of machinery fault status using transient vibration signal parameters," *Journal of Vibration and Control*, vol. 8, no. 3, pp. 321–335, 2002.

[42] R. Wagner and C. Clauser, "Evaluating thermal response tests using parameter estimation for thermal conductivity and thermal capacity," *Journal of Geophysics and Engineering*, vol. 2, no. 4, pp. 349–356, 2005.

[43] M. V. Rama Rao, A. Pownuk, S. Vandewalle, and D. Moens, "Transient response of structures with uncertain structural parameters," *Structural Safety*, vol. 32, no. 6, pp. 449–460, 2010.

[44] N. K. Saxena and A. Kumar, "Analytical approach to estimate mechanical parameters in induction machine using transient response parameters," *International Transactions on Electrical Energy Systems*, vol. 29, no. 3, p. e2751, 2019.

[45] S. R. Shaw and S. B. Leeb, "Identification of induction motor parameters from transient stator current measurements," *IEEE Transactions on Industrial Electronics*, vol. 46, no. 1, pp. 139–149, Feb. 1999.

[46] H. Kojooyan-Jafari, L. Monjo, F. Córcoles, and J. Pedra, "Parameter estimation of wound-rotor induction motors from transient measurements," *IEEE Transactions on Energy Conversion*, vol. 29, no. 2, pp. 300–308, Jun. 2014.

[47] C. Zhang, M. F. Lambert, J. Gong, A. C. Zecchin, A. R. Simpson, and M. L. Stephens, "Bayesian inverse transient analysis for pipeline condition assessment: parameter estimation and uncertainty quantification," *Water Resources Management*, vol. 34, no. 9, pp. 2807–2820, 2020.

[48] H. Kojooyan-Jafari, L. Monjo, F. Córcoles, and J. Pedra, "Parameter estimation of wound-rotor induction motors from transient measurements," *IEEE Transactions on Energy Conversion*, vol. 29, no. 2, pp. 300–308, Jun. 2014.

[49] M. Louzazni, A. Khouya, K. Amechnoue, A. Gandelli, M. Mussetta, and A. Crăciunescu, "Metaheuristic algorithm for photovoltaic parameters: Comparative study and prediction with a firefly algorithm," *Applied Sciences*, vol. 8, no. 3, p. 339, 2018.

[50] M. Pucci and M. Cirrincione, "Neural networks for parameter identification of induction motors," *IEEE Transactions on Industry Applications*, vol. 38, no. 5, pp. 1324–1333, Sept./Oct. 2002.

[51] Y. Xu and M. J. Khan, "Parameter estimation of photovoltaic modules using hybrid particle swarm optimization and analytical methods," *Energy Conversion and Management*, vol. 195, pp. 938–948, Sept. 2019.

Chapter 3

3

Parameter Identification In The Photovoltaic Systems

3.1 Introduction

As discussed in the last chapters, the dynamic behavior of the PV module can provide additional valuable information about the system. This analysis applies a small voltage signal with varying frequency to the module and examines its current response. In real-world applications, MPPT algorithms such as P&O already introduce step changes in voltage to track the MPP as it varies with irradiance and temperature. This stepwise excitation can be useful for identifying the ECM parameters. By developing the static SDM into a dynamic SDM that incorporates the junction capacitance to capture the transient behavior of the p–n junction, parametric identification can be performed directly in the time domain. This approach uses current and voltage waveforms acquired at the PV terminals, thus avoiding the need for frequency-domain analysis. PINN represent a framework, as they are capable of incorporating the dynamic model while leveraging current samples that capture the module's response to the voltage perturbations imposed by the P&O MPPT algorithm [1, 2].

In the next sections, the PINN formulation is introduced and first

applied to a linear PV model to evaluate its ability to identify parameters. Once its effectiveness is confirmed in the linear case, the approach is extended to a nonlinear PV model.

3.2 Dynamic Linear Single Diode Model

In the dynamic model of a photovoltaic cell, the initial circuit includes the components R_d, C_D, and C_T to represent the diode's dynamic behavior. This subcircuit is replaced with a single equivalent capacitance to simplify the model. As a result, the simplified circuit consists only of the photocurrent source I_{ph}, the series and shunt resistances R_s and R_{sh}, and the equivalent capacitance C. The capacitance models the dynamic behavior of the PN junction of the crystalline cells in the PV module [1]. The final equivalent circuit preserves the transient characteristics of the PV cell while allowing for a more straightforward analysis. The dynamic PV module SDM is shown in Fig.5.1.

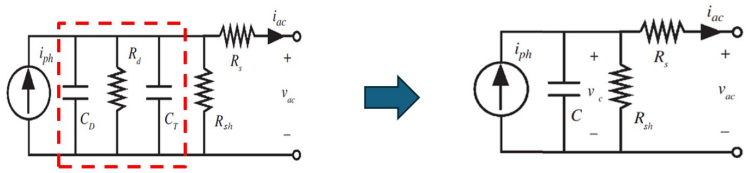

Figure 3.1: Dynamic SDM of the PV module.

Based on Kirchhoff's current law, the C current divides photogenerated current I_{ph} into the capacitor i_c, shunt resistor $i_{R_{sh}}$, and total output current i_{ac}. The equation is:

$$I_{ph} - i_c(t) - i_{R_{sh}}(t) - i_{ac}(t) = 0 \tag{1}$$

The capacitor current equation is as follows:

$$i_c = C\frac{dv_c(t)}{dt} \tag{2}$$

where C is the capacitance of the capacitor, and $v_c(t)$ is the voltage of the capacitor. In the linear case, the p-n junction capacitance is assumed to be constant. This simplification is introduced for having a simplified example on which to test the PINN potentiality on the given problem.

The equation for $i_{R_{sh}}$ is as follows:

$$i_{R_{sh}(t)} = \frac{v_c(t)}{R_{sh}} \tag{3}$$

Substituting these into the main equation, we have:

$$i_{ac}(t) = I_{ph} - C\frac{dv_c(t)}{dt} - \frac{v_c(t)}{R_{sh}} \tag{4}$$

On the other hand, the input voltage in the circuit is:

$$v_{ac}(t) = -R_s i_{ac}(t) + v_{R_{sh}}(t) \tag{5}$$

Since $v_{R_{sh}} = v_c$, we can write:

$$v_{ac}(t) = -R_s\left(I_{ph} - C\frac{dv_c(t)}{dt} - \frac{v_c(t)}{R_{sh}}\right) + v_c(t) \tag{6}$$

According to (6), the capacitor voltage equation becomes the following differential equation:

$$\frac{dv_c(t)}{dt} = \frac{v_{ac}(t) - \left(1 + \frac{R_s}{R_{sh}}\right)v_c(t)}{R_s C} + \frac{I_{ph}}{C} \tag{7}$$

The output current is given as:

$$i_{ac}(t) = \frac{v_c(t) - v_{ac}(t)}{R_s} \tag{8}$$

To investigate the dynamic behavior of the photovoltaic system over time, the state-space model can be defined based on these equations as follows:

$$\begin{bmatrix} \frac{dv_c(t)}{dt} \\ i_{ac}(t) \end{bmatrix} = \begin{bmatrix} \frac{1}{R_s C} \\ -\frac{1}{R_s} \end{bmatrix} v_{ac}(t) + \begin{bmatrix} -\left(1 + \frac{R_s}{R_{sh}}\right) \\ \frac{1}{R_s} \end{bmatrix} v_c(t) + \begin{bmatrix} \frac{I_{ph}}{C} \\ 0 \end{bmatrix} \tag{9}$$

This model allows us to analyze the response of the system to the input voltage $v_{ac}(t)$ over time.

In the following section, the simulation process in the Simulink is described in detail.

3.2.1 Dataset

The dynamic equivalent circuit of the PV simulated in the Simulink environment shown in Fig. 3.2.

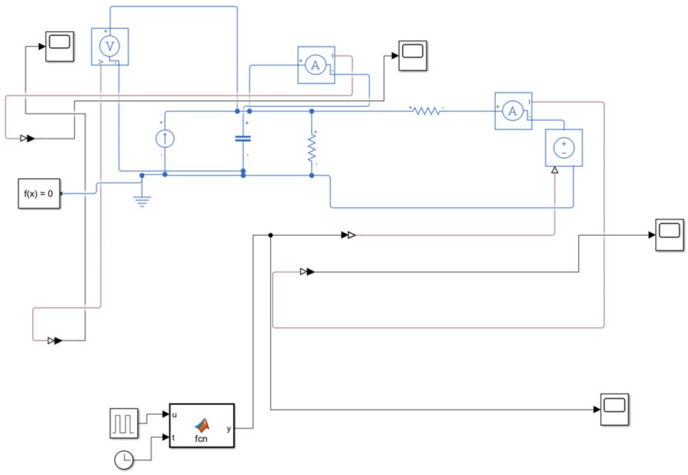

Figure 3.2: Equivalent circut in Simulink MATLAB.

For data extraction, the scope were used to record the voltage and current over time. The output data extracted as time-series vectors for analysis. These datasets were then used for training of the PINN. The input voltage $v_{in}(t)$ reflects typical MPPT behavior, and the PV output current $i_{ac}(t)$ represents the corresponding SDM response. Initially, noise is not added to the Simulink simulation to allow accurate analysis of the performance of the PINN identification method under different controlled conditions. The PV voltage and current datasets serve as input to the PINN to estimate the target parameters under both noisy and noise-free conditions in Python. Based on the literature, to evaluate the robustness of the PINN model, noise with standard deviations ranging from 0% to 5% is added to the PV current waveform [1]. Each noise level scenario repeats ten times with different random seeds to ensure statistical reliability. By simulating these inputs under varying noise conditions, the model's parameter estimation process shows its sensitivity and stability systematically. All simulations take place under STC, with irradiance at 1000 W/m^2 and temperature at

25 °C.

In the following subsection, the PINN approach is introduced and discussed in detail, highlighting its formulation and application to the problem at hand.

3.2.2 Physics Informed Neural Network Design

PINN can be used for both direct and inverse problems. In direct problems, they solve differential equations by learning solutions that follow physical laws. In inverse problems, they estimate unknown parameters from observed data. In both cases, the main advantage of PINN is that they include physics directly in the training process through the loss function. While the data-driven part is modeled by a feedforward neural network, the physics-based part ensures that the solution stays consistent with the governing equations.

A dynamic system is considered as presented in [2], which governing partial differential equation Partial Differential Equation (PDE) are given below:

$$u_t + \mathcal{N}[u;\lambda] = 0, \quad x \in \Omega,\ t \in [0,T] \tag{10}$$

$$f := u_t + \mathcal{N}[u;\lambda] \tag{11}$$

$u(t,x)$ is the unknown solution, implicitly defined through its time derivative u_t and the nonlinear operator $\mathcal{N}[u;\lambda]$, which together govern its evolution over space and time. The goal is to find $u(t,x)$ such that the PDE is satisfied within the spatial domain Ω and over the time interval $[0,T]$, subject to initial and boundary conditions. In other words, $u(t,x)$ is the target solution to be learned, while f is the residual that measures how well $u(t,x)$ satisfies the governing PDE [18]. The loss function is formulated for network as presented in (14).

$$\mathcal{L}(t,\theta) = \frac{1}{M}\sum_{i=1}^{M}\left(\left[\frac{dV_c}{dt} - u_{\text{PINN}}(t_i;\theta)\right]^2\right) + \lambda_1 \cdot \frac{1}{M}\sum_{j=1}^{M}\left(u_{\text{PINN}}(t_j;\theta) - u_{\text{obs}}(t_j)\right)^2 \tag{12}$$

It is worth to note that the system under study is a first order linear circuit, for which the time response can be calculated explicitly and a classical identification approach based on RMSE minimization can be applied. Nevertheless, the proposed example is useful to understand the PINN potential about the given problem and is a prelude of its application to the non-linear SDM.

In the following sections, we analyze how the PINN estimates the parameters and satisfies the physical constraints.

3.2.3 PV module circuit parameters and time domain waveforms

Table 3.1 describes the electric characteristics given by the manufacturer based on the datasheet for the Kyocera KC175GHT-2 panel at STC and the parameters of the SDM tuned for representing the panel [4].

According to [5], the capacitor value calculated for 16 cell. for calculate for 48 cells, it can be expressed as follows:

$$C_{16\text{cell}\times 3} = \frac{13316.44}{48} = 277.33\,\text{nF} \tag{13}$$

The input is the MPP step voltage (Fig. 3.3), and the output is the corresponding MPP step response current (Fig. 5.9).

The applied stepwise voltage is typical of MPPT control and is defined in (14) for a total duration of 4 μs:

$$V(t) = \begin{cases} 23.4 & 0 \le t < 1\ \mu s \\ 23.6 & 1\ \mu s \le t < 2\ \mu s \\ 23.4 & 2\ \mu s \le t < 3\ \mu s \\ 23.2 & t \ge 3\ \mu s \end{cases} \tag{14}$$

Table 3.1: Characteristics of a PV panel: Kyocera KC175GHT-2 at STC and .

Characteristics at STC	
V_{oc}	29.2 [V]
I_{sc}	8.09 [A]
M_{PP}	23.6 [V], 7.42 [A]
Thermal Coefficients	$\alpha_v = -109$ [mV/°C] $\alpha_I = 3.18$ [mA/°C]
Number of Cells	48
SDM Parameters	
I_{ph}	8.09 [A]
R_{s}	0.2185 [Ω]
R_{sh}	93.0571 [Ω]

Based on (9), the parameters R_s, R_{sh}, I_{ph}, and C need to be estimated. The details of the PINN architecture and training configuration are summarized in Table 6.1. In addition, (12) was considered as the loss function. The contribution of the data-based component was controlled by the weighting factor λ_1.

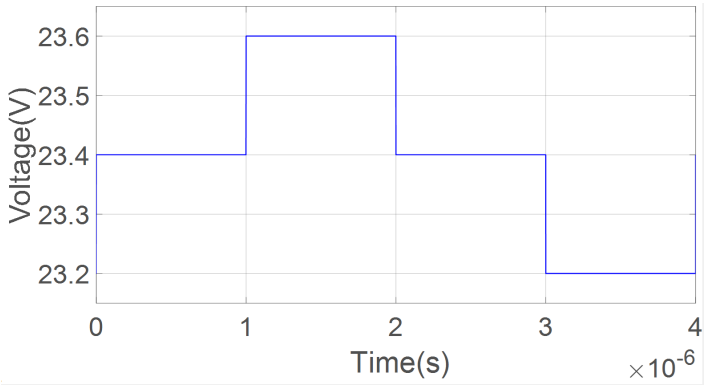

Figure 3.3: Step voltage input of the equivalent circuit in Simulink.

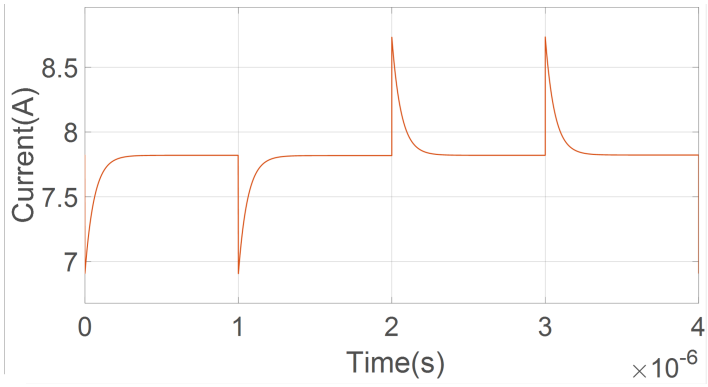

Figure 3.4: Step response current of the equivalent circuit in Simulink.

Table 3.2: PINN architecture and Training Details

Category	**Details**
Neural Network Structure	30 neurons, 3 hidden layers
Activation Function	Tanh
Optimizer	AdamW
Input Data Points	3000
Parameters Estimated	R_s, R_{sh}, C, i_{ph}
Training Epochs	250,001
Learning Rate	0.0005

Figures 3.5–3.8 illustrate the influence of each parameter on the output current. Increasing R_s reduces the peak current while increasing the initial slope. Increasing C, increases the peak current and results in a faster drop after discharge. Increasing I_{ph} raises the overall output current and the final constant-current level. The model exhibits the lowest sensitivity to I_{ph} and the highest sensitivity to R_{sh}.

Table 3.3: Parameter ranges for the estimation process.

Parameter	**Range**
I_{ph}	[0.1 A, 12 A]
R_s	[0.1 Ω, 0.35 Ω]
R_{sh}	[45 Ω, 140 Ω]
C	[125 nF, 375 nF]

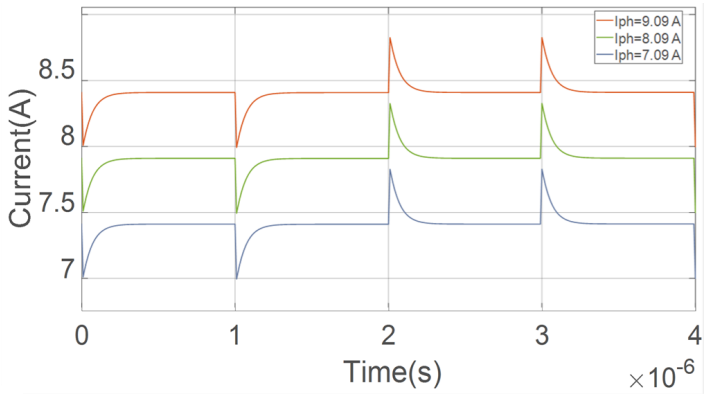

Figure 3.5: Effect of varying I_{ph} on the output current.

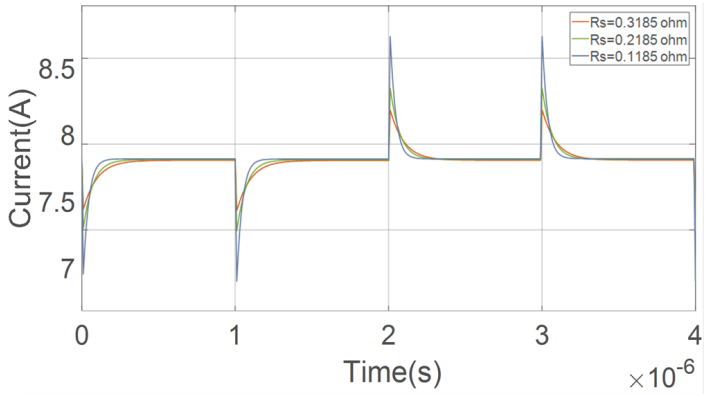

Figure 3.6: Effect of varying R_s on the output current.

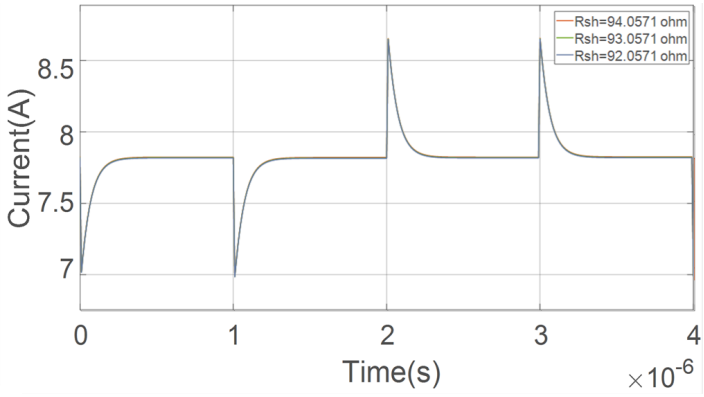

Figure 3.7: Effect of varying R_{sh} on the output current.

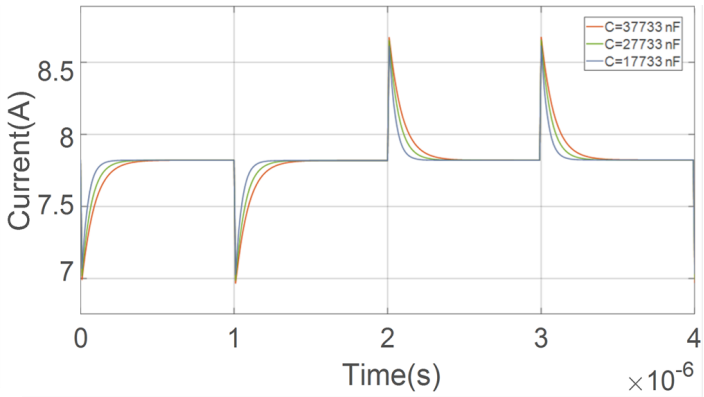

Figure 3.8: Effect of varying C on the output current.

Due to the high sensitivity to R_{sh}, several thresholds were tested for R_{sh} to determine an appropriate point for learning rate adjustment. When the value of R_{sh} during training reaches 90 Ω, the learning rate is reduced to 1×10^{-7}.

This threshold was chosen based on the physical behavior of the module, since increases in R_{sh} have negligible impact on the output current and the curves for different values of R_{sh} are hardly distinguishable. The input data consist of voltage and current values over time obtained from Simulink. The considered range for each parameter is reported in Table 3.3. The PINN framework embeds Kirchhoff's current law and the PV module's dynamic response, into the training process. The model is trained for 250,001 epochs

to ensure it can capture the converge properly for all parameters. Also, the L2 regularization [6] with a value of 10^{-8} is applied to improve the overall performance of the model. This simulation enables the evaluation of the system's performance under dynamic conditions and voltage variations. Figure 3.9 shows the comparison between the predicted and actual output current. Fig. 3.10 shows the evolution of the estimated parameters during training. The PINN demonstrates low sensitivity to the initial parameter values, which is beneficial in real applications where the exact range of parameters is not known. This property enables the model to achieve reliable convergence even with uncertain or approximate initial conditions.Moreover, it indicates that the network has effectively learned the underlying physical relationships of the system, rather than relying on specific starting points. As a result, the approach can be confidently applied to various operating conditions and datasets without extensive parameter tuning.

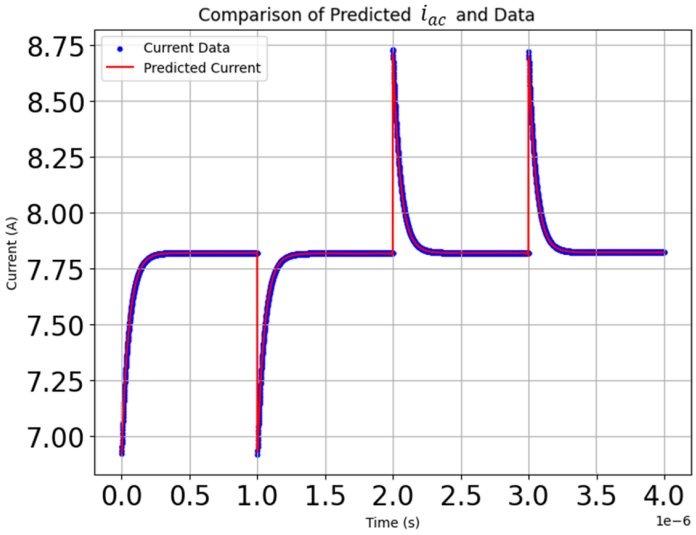

Figure 3.9: Comparison of predicted i_{ac} and simulated current data for the linear case. The blue dots represent the true data, while the red line shows the predicted current.

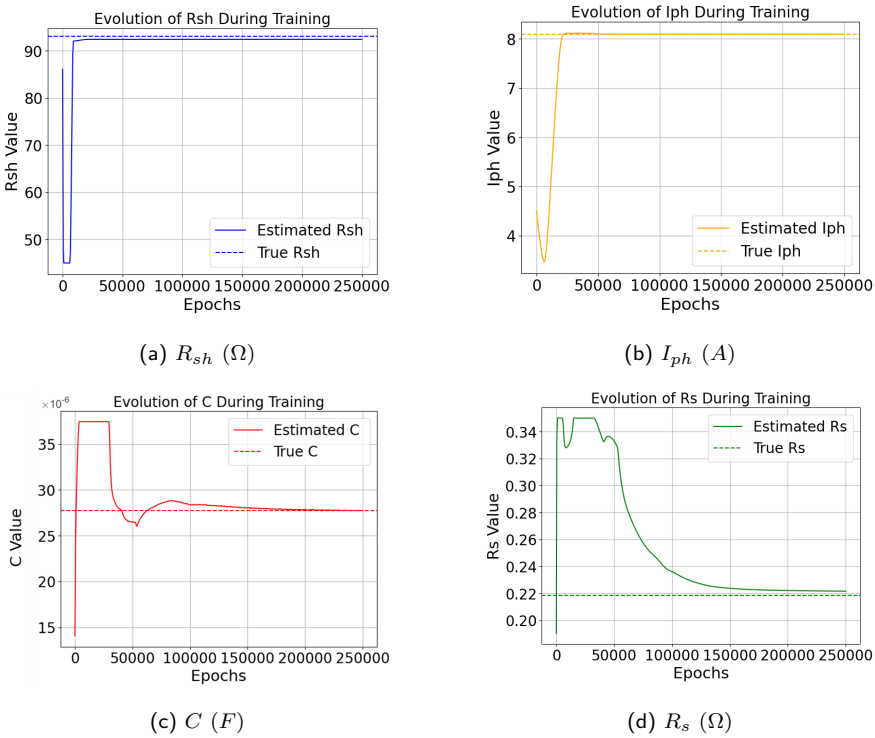

(a) R_{sh} (Ω) (b) I_{ph} (A)

(c) C (F) (d) R_s (Ω)

Figure 3.10: Evolution of estimated parameters during training for the linear case.

To take advantage of this property and to ensure the reliability of the results, this process was repeated for 100 different cases, each with random initial values within the ranges given in Table 3.3. The training epochs and network settings were identical for all cases. The results and analysis of these 100 repetitions are presented in Fig. 3.11. Also, Fig. 3.12 shows the probability distributions of the parameters R_s, C, I_{ph}, and R_{sh} for the 100 cases obtained using the Monte Carlo method [7]. The values of R_s range from 0.220 Ω to 0.228 Ω, with peaks around 0.220 Ω and 0.226 Ω. The values of C are uniformly distributed between 278 nF and 288 nF, indicating high stability in estimation. The values of I_{ph} range between 8.090 A and 8.097 A with a nearly symmetric distribution, showing strong consistency. The values of R_{sh} are between 90.5 Ω and 94 Ω.

These distributions confirm the stability of the model, and this feature makes the method highly advantageous, since in many practical cases the

true parameter values are unknown.

Figure 3.11: Box plot of estimation errors for each parameter over 100 runs. The average error for all parameters is below 2%, indicating high model accuracy.

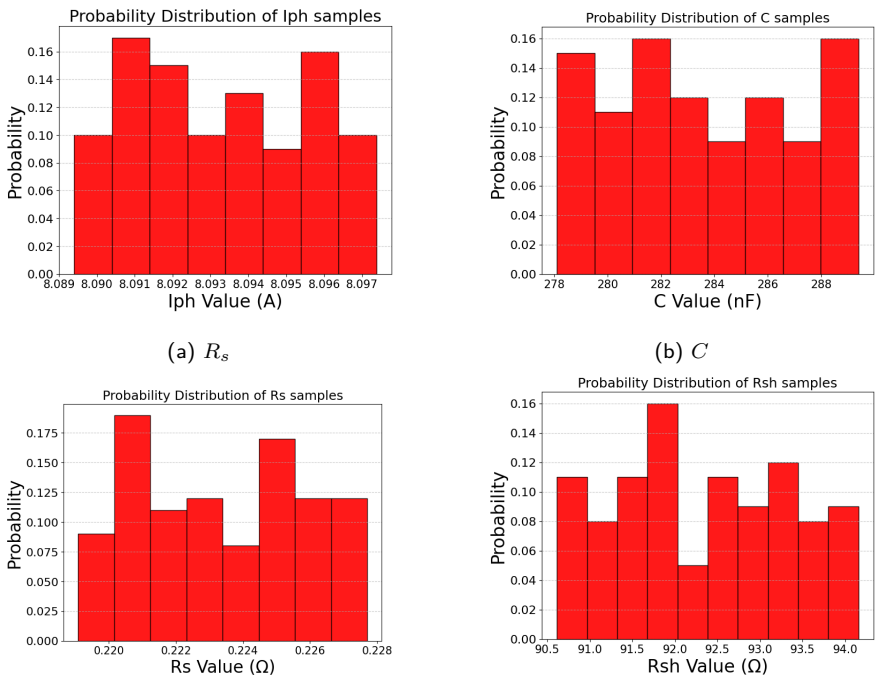

(a) R_s (b) C

(c) I_{ph} (d) R_{sh}

Figure 3.12: Probability distributions of estimated parameters over 100 Monte Carlo samples.

To investigate the effect of noise on the parameter identification pro-

cess, Gaussian noise ranging from 0 to 5% was applied to the $i_{ac}(t)$ samples. The results are presented in Fig. 3.13. The box plots represent the error percentage distributions for each parameter across different noise levels. For R_s, the error remains low and stable up to 4% noise, with median values below 2% and minimal variability. However, at 5% noise, the variability increases significantly, and more outliers appear, indicating that R_s becomes more sensitive to higher noise levels.

For R_{sh}, the error distribution demonstrates strong stability across all noise levels. The median error remains close to 0.5%, and the interquartile range is narrow, reflecting minimal variability. Even at 5% noise, the error increases slightly to around 1%, with a few outliers. This suggests that R_{sh} is robust under noise, with only minor sensitivity to higher noise levels.

The parameter C shows moderate sensitivity to noise. At lower noise levels, the median error is around 1%, and the variability is limited. As noise levels increase, especially at 5%, the interquartile range widens, and the presence of outliers becomes more noticeable. This highlights that C is affected by higher noise levels, leading to larger deviations in error.

The parameter I_{ph} stands out as the most robust. Across all noise levels, the median error remains consistently below 0.5%, with a very narrow interquartile range. Even at 5% noise, I_{ph} exhibits minimal variability and very few outliers, emphasizing its strong resistance to noise and reliable performance under varying conditions.

These observations highlight the effectiveness of the PINN framework in handling measurement noise across a range of parameters. The consistent performance for I_{ph} and R_{sh} indicates that the model successfully leverages physical constraints to maintain accuracy even in noisy environments. The increased variability in R_s and C under higher noise conditions suggests that further optimization could enhance robustness. Overall, the results demonstrate the potential of PINNs for reliable parameter estimation in real-world scenarios with uncertain or noisy data.

In the following subsection, the weighting strategy applied in the loss function is discussed. The focus is on how different loss terms are balanced to

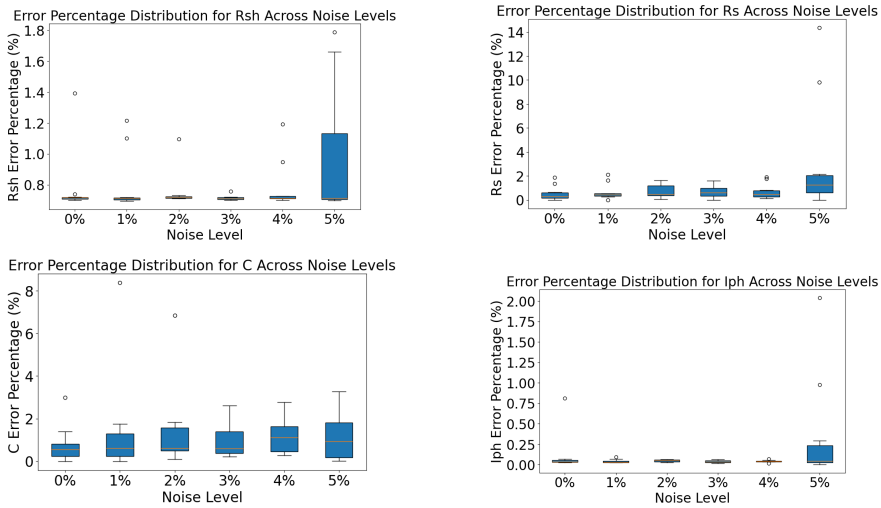

Figure 3.13: Error percentage distribution of R_{sh}, R_s , I_{ph}, and C across noise levels (0% to 5%). The bar heights represent the variations in parameter estimation due to different levels of Gaussian noise, while the horizontal line indicates the true value of the parameter for reference.

ensure stable training and accurate parameter estimation within the PINN framework.

3.2.4 Adaptive Weighting in the Loss Function

In general, the total loss function in a PINN framework combines both the data loss, which measures the discrepancy between model predictions and observations, and the physics loss, which enforces the governing equations. The weighting coefficients λ_{data} and λ_{physics} control the relative contribution of these two components [2], and the total loss can be written as:

$$\mathcal{L}_{\text{total}} = \lambda_{\text{data}} \mathcal{L}_{\text{data}} + \lambda_{\text{physics}} \mathcal{L}_{\text{physics}} \tag{15}$$

where:

- L_{physics} is the residual of the physical model.
- L_{data} is the data mismatch loss.

- λ_1 and λ_2 are weighting coefficients that balance the contributions of the data term and the physics term in the total loss function.

Selecting fixed values for the weights λ_1 and λ_2 is challenging, because assigning a significantly larger value to λ_1 leads the model to overfit the physics and neglect the data, whereas a much larger λ_2 causes the model to overfit the data and disregard the underlying physical laws. To address this problem, we develop a method base on adaptive weighting to adjust the balance during training, leading to more stable convergence and more accurate parameter estimation.

In order to balance the contributions of the data loss and physics-based loss during training, a self-adaptive weighting approach inspired by the concept of homoscedastic uncertainty was presented [8]. In this method, each loss term is associated with an inherent noise level, and the total objective function is derived from the negative log-likelihood of a Gaussian observation model. This formulation allows the network to automatically learn appropriate weights for each loss component, improving training stability and convergence without manual tuning. For two losses, L_{physics} and L_{data}, this yields:

$$L = \frac{1}{2\sigma_{\text{physics}}^2} L_{\text{physics}} + \frac{1}{2\sigma_{\text{data}}^2} L_{\text{data}} + \log \sigma_{\text{physics}} + \log \sigma_{\text{data}} \tag{16}$$

The terms $\sigma_{\text{physics}}^2$ and σ_{data}^2 represent task-dependent variances that act as weighting factors for the loss components. A smaller variance indicates higher confidence in that task and therefore gives it a larger contribution in the total loss.

To reduce the number of trainable parameters and balanced relationship between the physics and data, a parameter α is introduced as:

$$\sigma_{\text{physics}}^2 = e^{\alpha}, \quad \sigma_{\text{data}}^2 = e^{-\alpha} \tag{17}$$

Inserting these terms into the likelihood-based formulation gives the following expression:

$$L = \frac{1}{2}e^{-\alpha}L_{\text{physics}} + \frac{1}{2}e^{\alpha}L_{\text{data}} \tag{18}$$

In this formulation, α serves as a dynamic parameter that adjusts the relative importance of the data and physics losses during training. To keep the optimization stable, a quadratic regularization term $\eta\alpha^2$ is added, which limits extreme values of α and promotes smoother convergence.

Finally, the total loss function is:

$$L_{\text{total}} = \frac{1}{2}e^{-\alpha}L_{\text{physics}} + \frac{1}{2}e^{\alpha}L_{\text{data}} + \eta\alpha^2 \tag{19}$$

This formulation allows the model to adaptively balance the influence of the physics-based and data-driven components, leading to more stable and physically consistent learning behavior without the need to manually tune the weighting coefficients.

The sign of α provide direct insight into how the model distributes attention between the two loss terms. A positive α implies $e^{\alpha} > 1$ and $e^{-\alpha} < 1$, meaning that the data term is weighted more heavily. This typically occurs in the early training phase, when the model prioritizes fitting the observed data. because at the beginning of training, the network's estimation of physical residuals or derivatives is typically unstable and unreliable. To prevent the model from being dominated by inaccurate physical information, the optimizer naturally increases the value of α. As a result, e^{α} becomes larger and $e^{-\alpha}$ smaller, which means the network temporarily relies more on the data loss L_{data} and less on the physics loss L_{physics}. As training continues and the model begins to better capture the underlying physical dynamics, the estimation of physical quantities becomes more stable. Conversely, a negative α means $e^{\alpha} < 1$ and $e^{-\alpha} > 1$, indicating that the physics term has a greater influence. This usually happens after the network has stabilized and learned the main data patterns, allowing it to focus more on satisfying physical constraints. Consequently, the value of α gradually decreases, reducing the dominance of the data term and restoring a balanced contribution from both physics and data. This adaptive process allows the

model to start from data-driven learning for stability and then progressively integrate physical knowledge for consistency and generalization. Overall, α functions as an adaptive control parameter that reflects the model's confidence in each source of information. A larger, positive α corresponds to higher uncertainty in the physics component and therefore greater reliance on data, while a smaller or negative α indicates growing confidence in the physical relationships. The change in sign and magnitude of α throughout training is thus a natural outcome of the learning process, demonstrating how the model intelligently shifts between data-driven and physics-informed learning as it converges toward an optimal balance.

In the training process, along with the main parameters R_s, R_{sh}, I_{ph}, and C, the balancing coefficient α was also learned using the neural network configuration presented in Table 3.2, within the parameter ranges specified in Table 3.3. The evolution of the learned α during the training is illustrated in Figure 3.14.

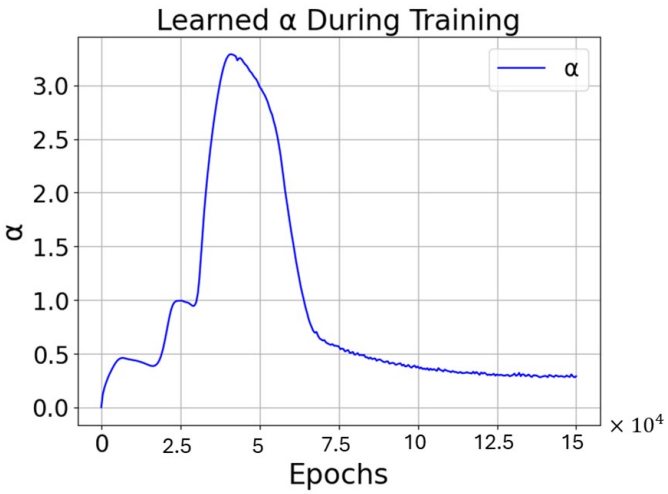

Figure 3.14: Learned α during training.

As shown in Figure 3.14, the value of α initially increases during the early training epochs. This behavior occurs because the network's estimation of the physical residuals is unstable and less reliable. Consequently, the

model temporarily increases α, which strengthens the weight of the data loss (L_{data}) through e^{α} and weakens the physics-based term (L_{physics}) through $e^{-\alpha}$. As the training progresses and the model begins to better capture the underlying system dynamics, restoring a balance between the physics and data components. The final convergence of α toward a small positive value indicates that both the physical and data-driven losses contribute comparably to the optimization process, ensuring stable and physically consistent learning.

The estimated parameter during the training are shown in Fig 3.15. These plots demonstrate that all four parameters converge accurately toward their true values, validating the effectiveness of the adaptive weighting mechanism.

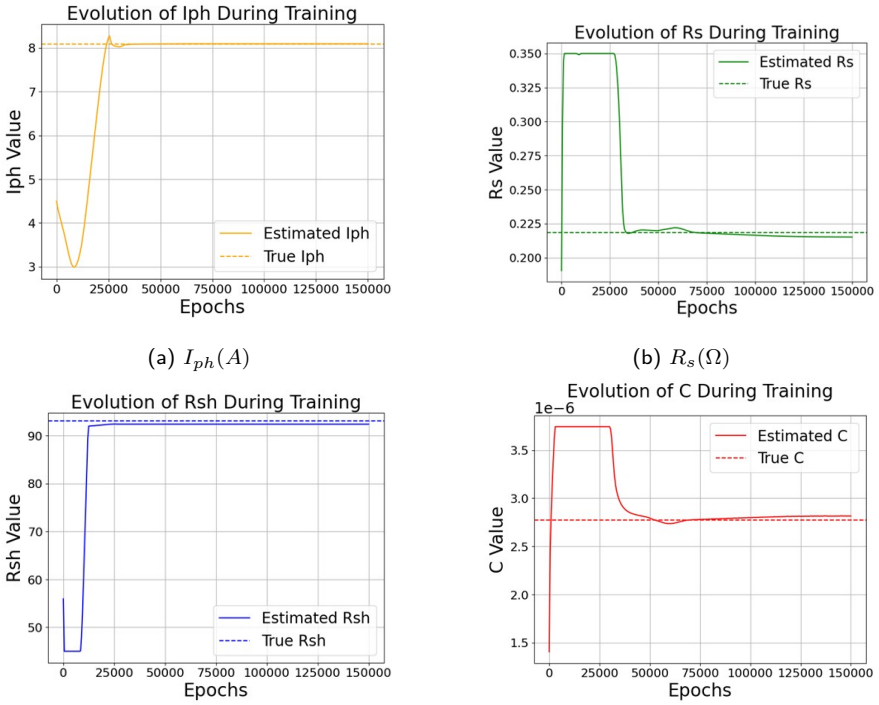

(a) $I_{ph}(A)$ (b) $R_s(\Omega)$

(c) $R_{sh}(\Omega)$ (d) $C(F)$

Figure 3.15: Evolution of estimated parameters during training for the linear case.

Consequently, PINN provides a robust framework for parameter esti-

mation and system identification without relying on prior knowledge of the exact values, which highlights its significant contribution and applicability. Building on these results, the method proves particularly well suited to the PV problem.

In the following section, the model is further developed to address the nonlinear case, thereby extending its applicability to more realistic operating conditions.

3.3 Nonlinear Singel Diod Modeling

In PV semiconductors, the depletion capacitance is what matters when the bias is low or reversed. It changes linearly with small changes in the voltage, causing the electric field to change [9]. When the forward bias is bigger, voltage-dependent effects like carrier accumulation (diffusion capacitance) become more important, leading to nonlinear behavior. Different from linear capacitance, diffusion capacitance grows exponentially with voltage. This is because minority carriers build up in almost neutral areas, making the link between charge and voltage not linear. This change from linear (depletion-dominated) to nonlinear (diffusion-dominated) capacitance is a key feature of how systems like photovoltaic cells respond to changes in operational and environmental factors [10].

Fig. 3.16 shows the PV module SDM with the diode replaced by its dynamic nonlinear capacitance.

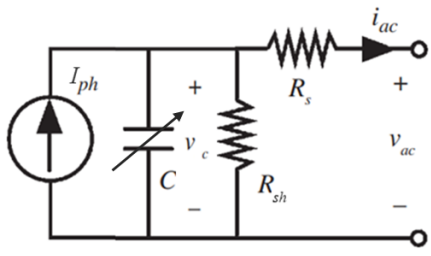

Figure 3.16: Dynamic and nonlinear SDM of the PV module that varies with voltage.

Equation (19) describes the diffusion capacitance in a PN junction [10], which arises from the injection of minority carriers into the neutral region and increases exponentially with the forward bias voltage $v_c(t)$:

$$C(v_c(t)) = \frac{q^2 n_i^2 A}{2kT} \left(\sqrt{\frac{D_p \tau_{p0}}{N_d}} + \sqrt{\frac{D_n \tau_{n0}}{N_a}} \right) \exp\left(\frac{q v_c(t)}{kT} \right) \tag{19}$$

The parameter q represents the electron charge, the parameter n_i denotes the intrinsic carrier concentration, the variable A refers to the junction area, the Boltzmann constant is represented by k, absolute temperature in Kelvin is denoted by T, the parameters D_p and D_n are the diffusion coefficients for holes and electrons, and the carrier lifetimes for holes and electrons are represented by τ_{p0} and τ_{n0}. Lastly, N_d and N_a indicate the donor and acceptor atom concentrations in the semiconductor.

At low voltages, depletion capacitance is the primary factor, whereas at higher voltages, diffusion capacitance gains importance because of decreased potential barriers and enhanced carrier storage. The relationship between temperature, minority carrier lifetimes, and dopant concentrations is represented by the coefficient b, defined as follows:

$$b = \frac{q^2 n_i^2 A}{2kT} \left(\sqrt{\frac{D_p \tau_{p0}}{N_d}} + \sqrt{\frac{D_n \tau_{n0}}{N_a}} \right) \tag{20}$$

Thus, the simplified diffusion capacitance becomes:

$$C(v_c(t)) = b \cdot \exp\left(\frac{q v_c(t)}{kT} \right) \tag{21}$$

For the current through the capacitor, we relate it to the time derivative of the charge, Q, on the capacitor. By assuming $Q(t) = C(v_c(t)) \cdot v_c(t)$, the current is:

$$i_c(t) = \frac{dQ}{dt} = \frac{d(C(v_c(t)) \cdot v_c(t))}{dt} \tag{22}$$

Substituting the expression for C, we have:

$$i_c(t) = b \cdot \frac{d\left(v_c(t) \cdot \exp\left(\frac{q v_c(t)}{kT} \right) \right)}{dt} \tag{23}$$

According to Kirchhoff's law, the current produced by the photogenerated I_{ph} is distributed among the current through the capacitor i_c, the current through the shunt resistor $i_{R_{\mathrm{sh}}}$, and the total output current $i_{\mathrm{ac}}(t)$. The equation is:

$$I_{\mathrm{ph}} - i_c(t) - i_{R_{\mathrm{sh}}}(t) - i_{\mathrm{ac}}(t) = 0 \tag{24}$$

The $i_{R_{\mathrm{sh}}}(t)$ expression is as follows:

$$i_{R_{\mathrm{sh}}}(t) = \frac{v_c(t)}{R_{\mathrm{sh}}} \tag{25}$$

So we have:

$$i_{\mathrm{ac}}(t) = I_{\mathrm{ph}} - b \cdot \frac{d\left(v_c(t) \cdot \exp\left(\frac{qv_c(t)}{kT}\right)\right)}{dt} - \frac{v_c(t)}{R_{\mathrm{sh}}} \tag{26}$$

On the other hand, the input voltage in the circuit is:

$$v_{\mathrm{ac}}(t) = -R_s \cdot i_{\mathrm{ac}}(t) + v_c(t) \tag{27}$$

Thus, we have:

$$\frac{v_c(t) - v_{ac}(t)}{R_s} = I_{ph} - \frac{v_c(t)}{R_{sh}} - \frac{d}{dt}\left(b\, e^{\frac{qv_c(t)}{KT}} v_c(t)\right) \tag{28}$$

In (28), if we consider:

$$b\left(\frac{qv_c(t)}{KT} + 1\right) e^{\frac{qv_c(t)}{KT}} \frac{dv_c(t)}{dt} = \alpha(t) \tag{29}$$

it is possible to obtain:

$$I_{ph} - v_c(t)\left(\frac{1}{R_{sh}} + \frac{1}{R_s}\right) + \frac{v_{ac}(t)}{R_s} - \alpha(t) = 0 \tag{30}$$

Moreover, the output current is as follows:

$$i_{\mathrm{ac}}(t) = \frac{v_c(t) - v_{\mathrm{ac}}(t)}{R_s} \tag{31}$$

Finally, if:

$$\begin{aligned} I_{ph} - v_c(t)\left(\frac{1}{R_{sh}} + \frac{1}{R_s}\right) + \frac{v_{ac}(t)}{R_s} \\ -b\, e^{\frac{qv_c(t)}{KT}} \frac{dv_c}{dt}\left(1 + \frac{qv_c(t)}{KT}\right) = 0 \end{aligned} \tag{32}$$

The model becomes:

$$\frac{dv_c(t)}{dt} = \frac{1}{b\, e^{\frac{qv_c(t)}{KT}}\left(1+\frac{qv_c(t)}{KT}\right)}\Bigg(I_{ph} - v_c(t)\left(\frac{1}{R_{sh}}+\frac{1}{R_s}\right)+\frac{v_{ac}(t)}{R_s}\Bigg) \tag{33}$$

This equation represents the differential equation governing the capacitor voltage $v_c(t)$ in a SDM of a PV system. For network training, the square-wave voltage waveform $v_{ac}(t)$ (Fig. 3.17), serves as the input to (33). The PINN is designed to solve (33) by estimating $v_c(t)$ so that, once $v_c(t)$ is substituted into (26), the current $i_{ac}(t)$ is calculated.

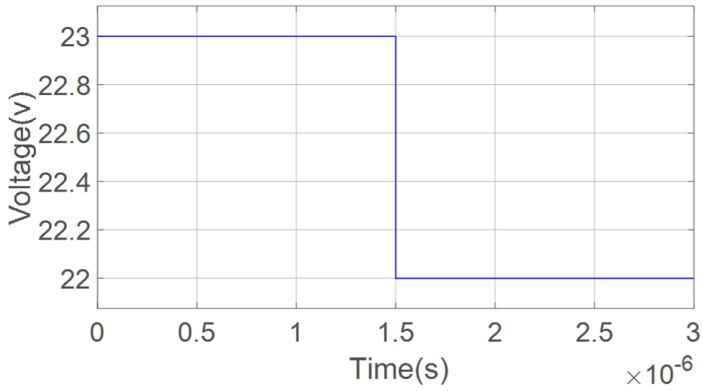

Figure 3.17: $v_{ac}(t)$ in Simulink MATLAB.

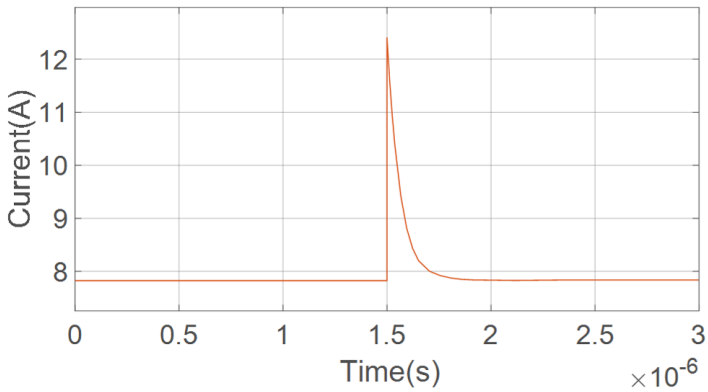

Figure 3.18: $i_{ac}(t)$ in Simulink MATLAB.

The panel specifications considered in this analysis are given in Table 3.1. The value $b = 3.88 \times 10^{-16} F$ is considered as a constant coefficient

for b. The PINN structure consists of 10 neurons and 3 hidden layers. The activation function is Tanh, and the optimizer is AdamW. A total of 600 input data points, consisting of voltage and current values over time, are used to estimate 4 parameters (R_s, R_{sh}, b, i_{ph}). The number of training epochs is set to 150001, and the learning rate for all parameters is determined as 0.0005. The initial values chosen randomly and the range considered for each parameter are shown in Table 3.4. Fig. 3.19 shows the evolution of the estimated parameters during training, while Fig. 5.5 the comparison between the simulated $i_{ac}(t)$ and the one obtained by the PINN-based identification.

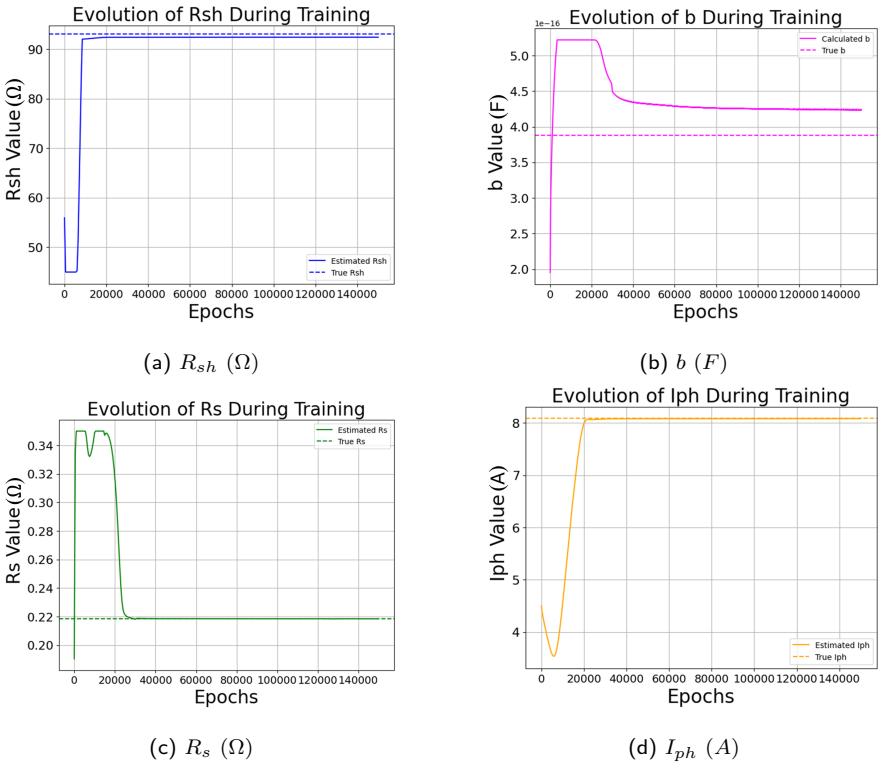

(a) R_{sh} (Ω) (b) b (F)

(c) R_s (Ω) (d) I_{ph} (A)

Figure 3.19: Evolution of estimated parameters during training for the linear case.

The results show that the parameters converge well. To investigate the effect of noise on the parameters identification process, a Gaussian noise from 0 to 5% has been applied to the $i_{ac}(t)$ samples. Results are shown in Fig. 3.21. As for R_s, the identification error remains low under noise levels up to 4%.

Table 3.4: Parameter Ranges for the Estimation Process

Parameter	**Range**
I_{ph}	[0.1A, 12A]
R_s	[0.1Ω, 0.35Ω]
R_{sh}	[45Ω, 140Ω]
b	$[2 \times 10^{-16}F, 6 \times 10^{-16}F]$

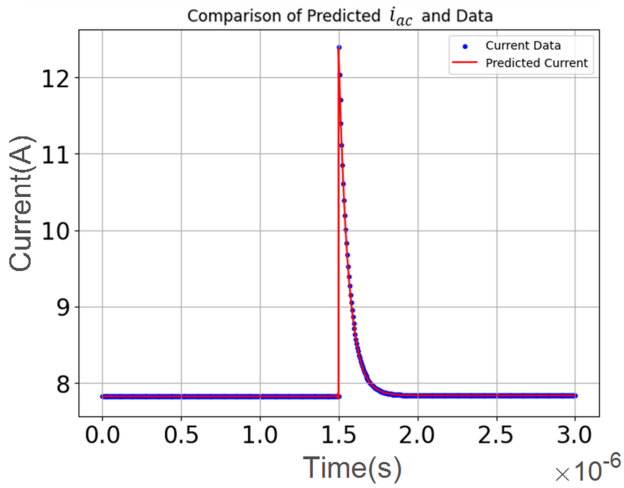

Figure 3.20: Comparison of the simulated $i_{ac}(t)$ in Simulink and the one obtained through the PINN-based identification. The blue dots represent the simulated data, while the red line shows the current waveform based on the parameters identified by the PINN.

At a 5% noise, the variability and presence of outliers increases significantly, showing that R_s becomes more sensitive to higher noise values. Similarly, R_{sh} exhibits stability across most noise levels, with consistently low errors and minimal variability. Even at 5% noise, its performance remains robust, though some sensitivity appears in the form of larger outliers. Instead, b demonstrates higher baseline errors compared to other parameters, with median values around 6%–7%. Noise significantly affects the identification

of b, as the error distribution is larger and more frequent outliers at higher noise levels appear. On the other hand, I_{ph} stands out as the most robust parameter, with consistently low errors and narrow distributions even under 5% noise, highlighting its strong resilience to measurement variability.

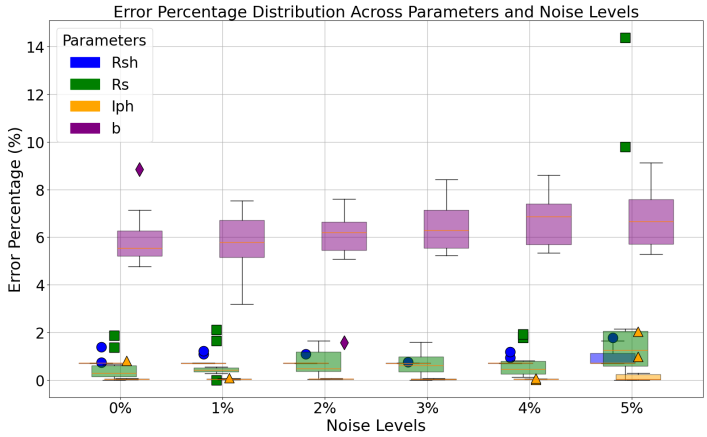

Figure 3.21: Error percentage distribution of R_{sh}, R_s , I_{ph}, and b across noise levels (0% to 5%). The box plots represent the interquartile range (IQR), with the horizontal line inside each box indicating the median error percentage. The bars (circles, squares, triangles, and diamonds) outside the boxes represent outliers (errors deviating significantly from the main distribution). Blue refers to R_{sh}, green to R_s, orange refers to I_{ph}, and purple to b.

In the following subsection, the Newton–Raphson analysis method is discussed for evaluating the behavior of the static parameters. This approach is employed to analyze the nonlinear relationships between the model parameters and the electrical characteristics of the PV, providing a deeper understanding of their steady-state behavior. The obtained results are then compared with those derived from the PINN-based estimation to validate the accuracy and consistency of the proposed approach.

3.4 Static Parameter Analysis

According to [11], the static parameters can be calculated using the Newton-Raphson (NR) method [12] based on datasheet values. Comparing

NR with the static SDM enables a more comprehensive assessment of the PINN. The NR method is one of the most powerful numerical techniques for solving nonlinear equations. In this study, the NR method is used to estimate the parameters of a static SDM. This method iteratively computes the roots of a nonlinear equation, progressively refining the estimated value of the independent variable to converge to the actual value.

In the static SDM, the output current of the PV module is given by:

$$I = I_{ph} - I_s \left(e^{\frac{V+IR_s}{aV_t}} - 1 \right) - \frac{V + IR_s}{R_{sh}} \tag{18}$$

To estimate the unknown parameters of the SDM, a system of five independent nonlinear equations is required; they are the following ones:

$$I_{ph} - I_s \left(e^{\frac{R_s I_{sc}}{\eta V_t}} - 1 \right) - \frac{R_s I_{sc}}{R_{sh}} - I_{sc} = 0 \tag{19}$$

$$\begin{aligned} &I_{ph} - I_s \left(e^{\frac{V_{MPP}+R_s I_{MPP}}{\eta V_t}} - 1 \right) \\ &- \frac{V_{MPP} + R_s I_{MPP}}{R_{sh}} - I_{MPP} = 0 \end{aligned} \tag{20}$$

$$I_{ph} - I_s \left(e^{\frac{V_{oc}}{\eta V_t}} - 1 \right) - \frac{V_{oc}}{R_{sh}} = 0 \tag{21}$$

$$\left. \frac{\partial P_{pv}}{\partial V_{pv}} \right|_{MPP} = 0 \tag{22}$$

$$\left. \frac{\partial I_{pv}}{\partial V_{pv}} \right|_{MPP} = -\frac{I_{MPP}}{V_{MPP}} \tag{23}$$

By solving (19-23) using the NR method, the static parameters have been estimated. This iterative process continues until the estimated values converge, meaning that the changes in subsequent iterations become negligible. In Fig. 3.22, the results obtained from the NR and PINN methods are compared. The values estimated by the PINN method are closer to the expected values, as shown in Table 3.5. The PINN method is able to keep the error value for some parameters small.

Table 3.5: Comparison among the values of the estimated parameters obtained by the NR method and by the PINN-based one [8].

Parameter	**SDM value [8]**	**NR**	**PINN**
I_{ph} (A)	8.0900	7.8484	8.0785
R_s (Ω)	0.2185	0.2449	0.2180
R_{sh} (Ω)	93.0571	92.4989	92.8187

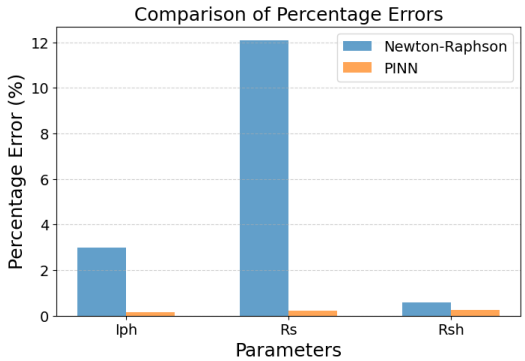

Figure 3.22: Comparison of Percentage Errors in Estimated Circuit Parameters Using Newton-Raphson and PINN Methods. The results indicate that the PINN model provides significantly lower percentage errors across all parameters (I_{ph},R_s,R_{sh}) compared to the Newton-Raphson method, demonstrating its superior accuracy in parameter estimation.

In Fig. 3.22, the percentage error results obtained from the NR and PINN methods are compared.

For the estimated R_s obtained from both methods, a significant difference between the NR and PINN estimates highlights its sensitivity to the solution approach. The governing equations that define R_s exhibit nonlinear behavior, making it more challenging to estimate accurately. The PINN approach integrates data-driven learning with physical constraints, refining parameter estimation by adapting to the nonlinear nature of the equations. Unlike purely numerical methods, PINN can account for small variations in the data and improve robustness against noise and modeling inaccuracies.

This makes it particularly useful for estimating parameters that are sensitive to computational approaches, such as R_s.

However, the estimation of R_s remains challenging due to its strong sensitivity to the transient regions. The precision of measurement instruments, sampling frequency, and inherent system noise can further amplify these effects, making the accurate estimation of R_s difficult even for a well-trained PINN model. Moreover, even when measurement data are available, essential information related to the fast transient behavior may be partially lost or distorted due to limited temporal resolution or filtering effects, further complicating the estimation process. This issue will be examined in more detail, by focusing on how the sensitivity of R_s to transient dynamics influences convergence, and exploring potential modifications to the loss formulation and network architecture to enhance the reliability of R_s estimation under realistic measurement conditions.

In general, this chapter developed the baseline framework of the PINN applied to the dynamic SDM of a PV system. The chapter focused on integrating the governing physical equations of the PV circuit directly into the neural network structure, enabling the model to learn both from data and from the underlying physics. In this analysis, the transient behavior of the circuit was embedded into the loss function, allowing the network to infer the dynamic evolution of system parameters. The implementation relied on minimizing a hybrid loss function that combined data loss and physics loss terms. This structure allowed the PINN to reconstruct the physical consistency of the system even in cases where measurements were incomplete or affected by noise. This chapter validated the proposed framework through simulated case studies, showing that the network effectively learned the time-domain characteristics of the PV system. The combination of data-driven learning and embedded physical constraints established the proposed PINN as a powerful and reliable tool for dynamic parameter identification. The findings of this chapter formed the foundation for further developments in multi-network and layered PINN structures introduced in the subsequent chapters. To further improve training stability, Chapter 3 introduced an

adaptive weighting scheme that dynamically balanced the contributions of the data and physics terms during optimization. This adaptive mechanism accelerated convergence in the early epochs and ensured fine-tuning precision in later stages of training. The results demonstrated that the proposed adaptive PINN achieved faster convergence and lower estimation errors compared to conventional optimization-based methods such as Newton–Raphson and genetic algorithms. The chapter also investigated the effect of noise on estimation accuracy. The model was tested under multiple noise levels, and the results showed that the physics-informed component significantly improved robustness against data uncertainty. Even under severe noise contamination, the PINN maintained smooth parameter trajectories and physically consistent predictions. The estimated parameters closely matched the true parameters considered, confirming the model's ability to accurately capture both static and dynamic behavior. In the next chapter, this issue is discussed in detail, and a new PINN-based model is developed to address the challenges associated with R_s estimation.

References

[1] N. Femia, G. Petrone, G. Spagnuolo, and M. Vitelli, *Power Electronics and Control Techniques for Maximum Energy Harvesting in Photovoltaic Systems*. CRC Press, 2017.

[2] M. Raissi, P. Perdikaris, and G. E. Karniadakis, "Physics-informed neural networks: A deep learning framework for solving forward and inverse problems involving nonlinear partial differential equations," Journal of Computational Physics, vol. 378, pp. 686–707, 2019, doi: 10.1016/j.jcp.2018.10.045.

[3] J. Stiasny, G. S. Misyris, and S. Chatzivasileiadis, "Physics-informed neural networks for non-linear system identification for power system dynamics," *2021 IEEE Madrid PowerTech*, pp. 1–6, 2021, doi: 10.1109/PowerTech46648.2021.9495063.

[4] G. Petrone, C. A. Ramos-Paja, and G. Spagnuolo, Photovoltaic Sources Modeling. Wiley, 1st ed., Jan. 2017. doi: 10.1002/9781118755877.

[5] R. A. Guejia-Burbano and G. Petrone, "Partial shading detection on PV panels through on-line Impedance Spectroscopy," in IEEE International Conference on Environment and Electrical Engineering and 2021 IEEE Industrial and Commercial Power Systems Europe (EEEIC/I&CPS Europe), ZUZL, pp. 1–0, doi: 10.1109/EEEIC/ICPSEurope51590.2021.9584621.

[6] A. Lewkowycz and G. Gur-Ari, "On the Training Dynamics of Deep Networks with L2 Regularization," *34th Conference on Neural Information Processing Systems (NeurIPS 2020)*, Vancouver, Canada, 2020. Available: `https://arxiv.org/abs/2006.08643`.

[7] D. P. Kroese and R. Y. Rubinstein, "Monte Carlo methods," WIREs Computational Statistics, vol. 4, no. 1, pp. 48–58, Jan. 2012, doi: 10.1002/wics.194.

[8] A. Kendall, Y. Gal, and R. Cipolla, "Multi-task learning using uncertainty to weigh losses for scene geometry and semantics," in Proceedings of the IEEE Conference on Computer Vision and Pattern Recognition (CVPR), 2018, pp. 7482–7491.

[9] D. A. van Nijen, M. Muttillo, R. Van Dyck, J. Poortmans, M. Zeman, O. Isabella, and P. Manganiello, "Revealing capacitive and inductive effects in modern industrial c-Si photovoltaic cells through impedance spectroscopy," *Solar Energy Materials and Solar Cells*, vol. 260, pp. 112486, Aug. 2023, doi: 10.1016/j.solmat.2023.112486.

[10] D. A. van Nijen, P. Procel, R. A. C. M. M. van Swaaij, M. Zeman, O. Isabella, and P. Manganiello, "The nature of silicon PN junction impedance at high frequency," *arXiv preprint*, 2024, Available: `https://arxiv.org/abs/2409.06749`.

[11] C. Khin, P. Buasri, A. Siritaratiwat, and R. Chatthaworn, *Simulation and Experimental Results for a Single Diode Photovoltaic Model using Newton-Raphson Parameter Estimation Method.* Engineering Access, vol. 4, no. 2, pp. 29-36, 2018.

[12] C. T. Kelley, *Solving Nonlinear Equations with Newton's Method.* Society for Industrial and Applied Mathematics, 2003.

Chapter 4

4

Multiple Physics-Informed Neural Networks

4.1 Introduction

In real-world scenarios, measurements are often affected by sensor noise, hardware limitations, or communication errors, which can lead to missing or corrupted data. Such imperfections reduce the reliability of analysis and fault diagnosis. Accurate estimation of parameters heavily relies on the model's ability to capture transitions in the current waveform, particularly during transient and peak regions. The transient regions of the waveform usually contain the most useful information. When these regions are not sampled with sufficient time resolution or the sensor bandwidth is limited, important features that describe the system's fast response may be lost, leading to reduced estimation accuracy [1]. Previous studies have shown that limited sampling resolution can result in biased or unstable estimates of R_s, especially when the sampling rate is not sufficent to capture the rapid changes in the current waveform (Fig. 4.1). Overall, the reliability of parameter identification strongly depends on the quality of the measured waveform and the sampling rate of the data.

In the next section, this issue and its possible solutions will be dis-

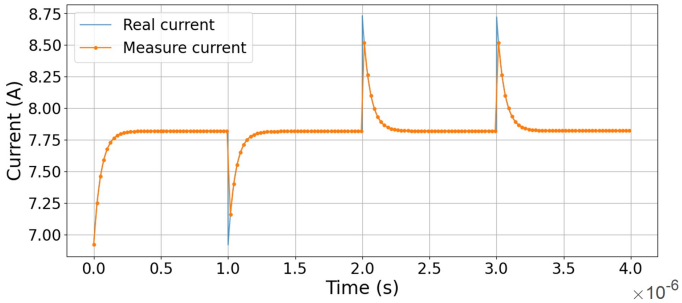

Figure 4.1: Comparison of the real current and the measured current over time. The discrepancies between the two curves may arise in real-world scenarios due to factors such as measurement noise, sensor delays, limited sampling rates, or filtering applied during data acquisition. The measured waveform fails to accurately capture the sharp peak, potentially leading to significant information loss in transient regions that are essential for reliable estimation of R_s.

cussed in detail, including the analysis of how transient behavior affects convergence and the introduction of strategies to improve the stability and accuracy of R_s estimation within the PINN framework.

4.2 Simulation Scenario and Data Description

In this scenario, the dataset is synthetically generated through dynamic simulation of an equivalent PV circuit model developed in Simulink, similar to the modeling framework discussed in the previous chapter. The input voltage signal $v_{in}(t)$ is designed to replicate the typical behavior associated with MPP tracking, while the output current $i_{ac}(t)$ represents the corresponding response of the SDM. First, the set of 4000 input-output data points was initially extracted from a Simulink. To emulate more realistic and cost-effective scenarios we systematically downsampled the original dataset to obtain subsets containing 2000, 1000, 500, and 200 points.

Taking into account the simulation scenario, the PINN framework model applied to analyze the system. As illustrated in Fig. 4.2, the accuracy of parameter estimation progressively declined as the number of available data points was reduced. While the results remained consistent with the

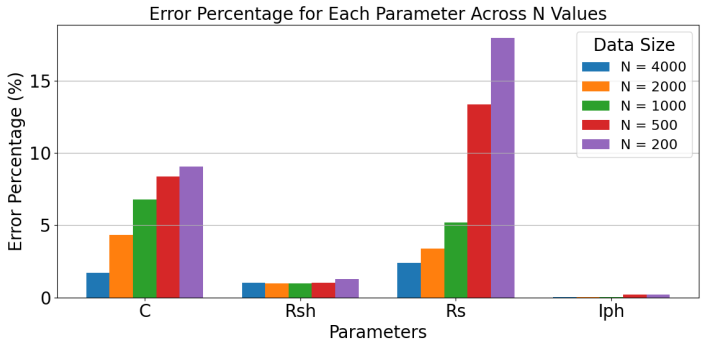

Figure 4.2: Error percentage for model parameters across different data sizes (N). The bar chart illustrates the estimation error for four parameters (C, R_{sh}, R_{s}, I_{ph}) using datasets of varying sizes (N = 4000, 2000, 1000, 500, and 200). The errors for R_{s} and C increase notably as N decreases, indicating higher sensitivity to data volume. In contrast, R_{sh} and I_{ph} maintain relatively stable error percentages across all data sizes.

reference values for $N = 4000$ and $N = 2000$, significant deviations were observed at lower sampling levels. In particular, the parameters R_s and C exhibited considerable sensitivity to reduced data density: the relative error in C increased from approximately 1.7% at $N = 4000$ to over 8% at $N = 200$, while the error in R_s increases from 2.4% to 17.4% in the same range. By contrast, the estimates of R_{sh} and I_{ph} remained largely unaffected by the sampling rate.

This performance drop can be primarily attributed to the transient segments of the input waveform, where the voltage undergoes rapid variations over short time intervals. During such transitions, particularly at rising and falling edges, the system's dynamic response is dominated by parameters such as R_s and C, which control the speed and shape of the transient behavior. As the data becomes sparser through downsampling, the resolution around these fast-changing regions diminishes, leading to inadequate representation of the system's dynamics inaccurate parameter estimation.

In the next section, we introduce a new network and loss function designed to address the problems discussed above.

4.3 Multiple Physics-Informed Neural Networks

In typical PINN frameworks, a single neural network is used to learn the solution, and the loss function usually combines two terms. One encourages the network to fit the observed data, while the other ensures that the solution satisfies the underlying physical laws through automatic differentiation. While this approach provides a balance between data-driven learning and physical constraints, it may fall short when key parameters exert subtle effects on the system. In such cases, the network may struggle to accurately capture the underlying dynamics, leading to slow convergence and limited generalization [2]. To address these limitations, we develop a multiple network architecture in which each key physical parameter is estimated via a dedicated neural network. This separation allows each network to adapt to the specific dynamic behavior of its associated parameter, thereby improving accuracy, enhancing stability, and reducing training time. By aligning both the architecture and the loss function more closely with the underlying physics, the proposed method enhances model robustness and generalization in practical scenarios involving limited or imperfect data. The structure of the proposed network is illustrated in Fig. 4.3. This introduces a new perspective, where the learning process is guided not only by data and equations but also by the distinct physical roles of each parameter. This physics-based viewpoint brings valuable interpretability to the learning process and allows the model to focus on what truly matters in the behavior of photovoltaic systems.

This architectural separation leverages the fundamentally different roles and temporal behaviors of the parameters involved in the photovoltaic system model. Parameters such as R_s and C are tightly dependent on the system's transient response. Further details of the neural network structure and training configuration are provided in Table 4.1. Accurately estimating these parameters requires the network to be sensitive to local variations and fast-changing patterns in the data. For this reason, a deeper neural network with batch normalization, residual connections, and layer normalization is

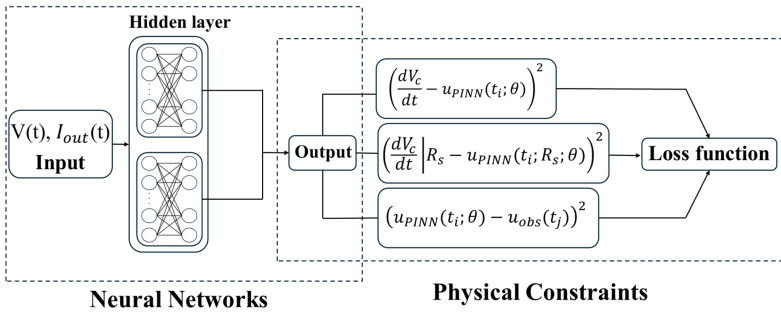

Figure 4.3: Architecture of the PINN used for modeling and parameter estimation. The network takes voltage $V(t)$ and output current $I_{\text{out}}(t)$ as inputs and passes them through hidden layers to generate predictions for internal quantities. These outputs are constrained by physical laws in the loss function, including residual terms derived from the circuit model and comparison with observed data.The total loss is computed from a combination of data-driven and physics-based terms, enabling the network to infer R_s more robustly.

employed that allows the model to better capture rapid dynamics, stabilize training, and maintain gradient flow across layers. Batch normalization helps keep the input to each layer stable during training, which makes the learning process faster and more reliable. Residual connections make it easier for the network to pass information between layers, especially in deeper networks, and prevent problems like vanishing gradients. Layer normalization also helps keep the training stable, especially when the batch size is small or changes during training. In contrast, I_{ph} and R_{sh} are influenced more by environmental conditions and exhibit relatively smooth or slowly varying behavior. Estimating them through a simpler network minimizes unnecessary complexity and overfitting, while preserving generalization in the presence of noise or sparse data. The main advantage of this architectural separation lies in its ability to disentangle the learning processes associated with parameters that operate on different temporal and physical scales. By assigning dedicated networks to each group of parameters, the model allows each sub-network to focus on a specific dynamic behavior without being affected by unrelated variations in the data.

Table 4.1: Network architecture designed based on the behavioral differences of parameters.

Network Information	**Network 1**	**Network 2**
Number of Layers	15	10
Neurons per Layer	3	3
Activation Function	Tanh	Tanh
Optimizer	AdamW	AdamW
Learning Rate	5×10^{-4}	5×10^{-4}
L2 Regularizer	1×10^{-8}	1×10^{-8}
Epochs	100001	100001
Batch Normalization	Yes	No
Residual Connections	Yes	No
Layer Normalization	Yes	No

The effectiveness of this separation is illustrated in Fig. 4.4.

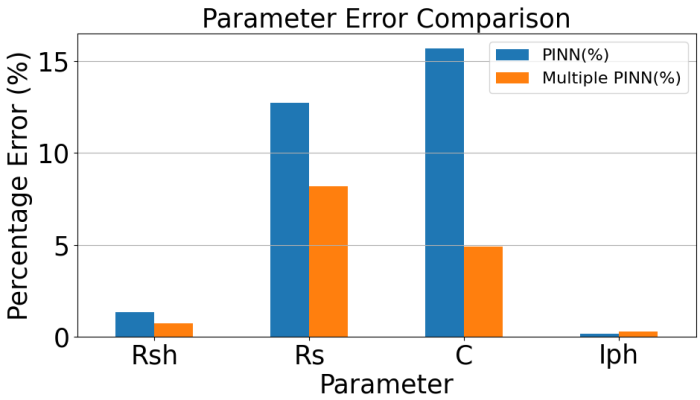

Figure 4.4: Comparison of parameter estimation error between a PINN and a Multiple-PINN architecture. The use of multiple PINNs significantly reduces the percentage error in estimating R_s and C, which are typically more sensitive to data dynamics. All parameters show improved accuracy under the multiple-PINN network, demonstrating its effectiveness in learning parameter behaviors.

As shown in Fig. 4.1, the loss of the waveform leads to a substantial

loss of high-frequency information precisely at regions where sharp voltage or current transitions occur. These transition zones encapsulate the system's most informative dynamic content, where derivatives of the signals are at their peak and the influence of dynamic parameters such as R_s and C is most pronounced. The absence of sufficient temporal granularity in these regions compromises the sensitivity of the loss function to variations in these parameters, thereby hindering their accurate estimation. In effect, this information loss reduces the observability of transient-driven dynamics and deteriorates the model's ability to resolve parameters that predominantly govern high-rate system responses. In PINNs, the loss function combines physical laws and observed data, balancing them through weighting factors. The loss function is defined in equation (1).

$$\begin{aligned}\mathcal{L}(t,\theta) = \frac{1}{M}\sum_{i=1}^{M}\left(\left[\frac{dV_c}{dt} - u_{\text{PINN}}(t_i;\theta)\right]^2\right) \\ + \lambda_1 \cdot \frac{1}{M}\sum_{j=1}^{M}\left(u_{\text{PINN}}(t_j;\theta) - u_{\text{obs}}(t_j)\right)^2 \\ + \lambda_2 \cdot \frac{1}{M}\sum_{k=1}^{M}\left(\left[\left.\frac{dV_c}{dt}\right|_{R_s} - u_{\text{PINN}}(t_k;R_s,\theta)\right]^2\right)\end{aligned} \tag{1}$$

The loss function used in this model consists of three components. The first term is the physics-informed loss, which ensures physical consistency by minimizing the residuals of the governing differential equations. The second term is the data loss, which measures the difference between the predicted and observed outputs based on the input data. The third component includes a term involving the derivative of the governing differential equations with respect to R_s, since R_s is highly sensitive to changes in the waveform during the transient phase. To improve the accuracy of R_s estimation, we include a term in the loss function based on the analytical derivative of the system equation with respect to R_s. This term is derived from the time derivative of the capacitor voltage V_c, which inherently depends on R_s through the system's physical dynamics. By incorporating this derivative-based term, the loss function accounts not only for discrepancies in the predicted output,

but also for how sensitively the system responds to variations in R_s. This leads to more accurate and physically meaningful parameter estimation.

In our loss function, λ_1 and λ_2 are weighting coefficients assigned to the data-driven and physics-informed terms, respectively. While $\lambda_1 = 1000$ ensures that the model remains closely aligned with the observed data, $\lambda_2 = 10^{-8}$ specifically controls the influence of the regularization term associated with R_s, which was added to compensate for the loss of data affecting its estimation. λ_1 coefficients were selected through a grid search over the range $[0, 1500]$ with 100 evaluation steps to ensure a balanced optimization. Although the numerical contribution of this term to the total loss is small, it becomes increasingly important during transient moments, specifically when the input voltage changes rapidly and the system exhibits nonlinear behavior. In the transient moments, the derivative of the output current with respect to R_s grows sharply, reflecting the stronger influence of R_s on the system's dynamic response. By penalizing large deviations in this derivative, the term implicitly encourages the network to capture more realistic and physically consistent values of R_s. This additional constraint acts as a form of regularization that stabilizes the training process.

Given the incomplete information about R_s, the inclusion of a physics-informed constraint allows the model to preserve physical consistency, while the small value of λ_2 ensures that this term contributes meaningfully without overwhelming the learning process. The effectiveness of the R_s term in loss function is illustrated in Fig. 4.5.

To verify the effectiveness of the proposed PINN, the analysis was first conducted on the linear model using the defined dataset and simulation scenario. In the following subsection, this linear model is employed to confirm the validity and reliability of the proposed PINN formulation before applying it to more complex cases.

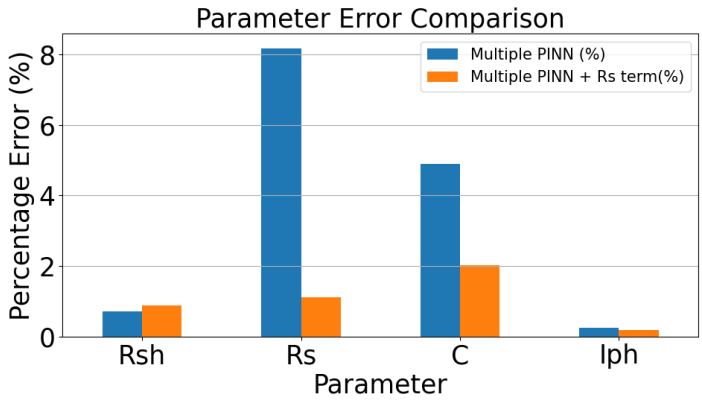

Figure 4.5: Comparison of parameter estimation error with and without the inclusion of the R_s term in the loss function. Including the R_s-dependent physical constraint significantly reduces the percentage error for the R_s and C parameters, improving model accuracy. The R_{sh} and I_{ph} parameters show only minor changes, indicating less sensitivity to this term in the loss formulation.

4.3.1 Multiple PINN Validation on Linear Diode Model

To clearly analyze the effect of data loss in the high-frequency transient region of the system's response, this study restricts the investigation to a single transient case, as shown in Fig. 4.6. Initially, there were 74 data points consisting of voltage and current values over time, which increased to 116 data points after upsampling in the transient region. The data obtained from Simulink like pervios chapter and this input are used in the Python.

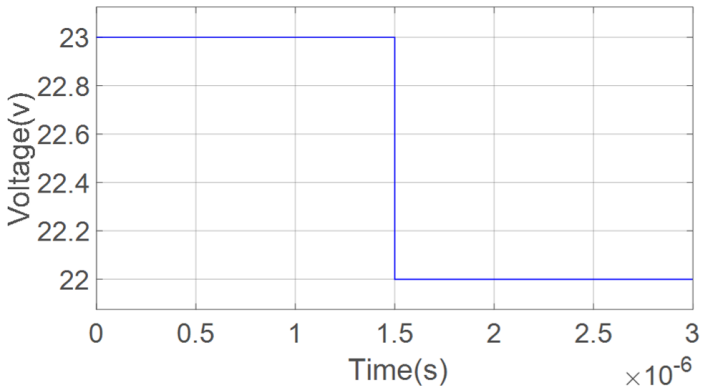

Figure 4.6: Input $v_{ac}(t)$ step waveform.

By downsampling the data around the transient region, we generate the scenario illustrated in Fig. 4.7.

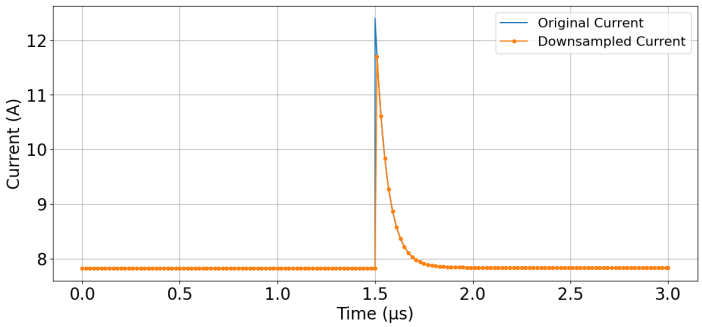

Figure 4.7: Original and downsampled current input used for parameter estimation in the multiple PINN model. The plot shows a sharp current peak around $t = 1.5$ μs, followed by an exponential decay. While the downsampled signal (orange markers) closely follows the original (blue line), slight loss of resolution near the peak may influence the accuracy of parameter estimation.

The range considered for each parameter is shown in Table 4.2.

Table 4.2: Parameter Ranges for the Estimation Process

Parameter	**Range**
I_{ph}	[0.1A, 12A]
R_s	[0.1Ω, 0.35Ω]
R_{sh}	[45Ω, 140Ω]
C	$[125 \times 10^{-9}\,\mathrm{F},\ 375 \times 10^{-9}\,\mathrm{F}]$

Fig. 4.8 shows how the parameter estimates change and improve during the training.

Initially, the parameters are randomly initialized within the ranges provided in Table 4.2, and their values differ considerably from the true ones. As training continues, the PINN gradually adjusts these estimates by incorporating both observed data and the underlying physical equations,

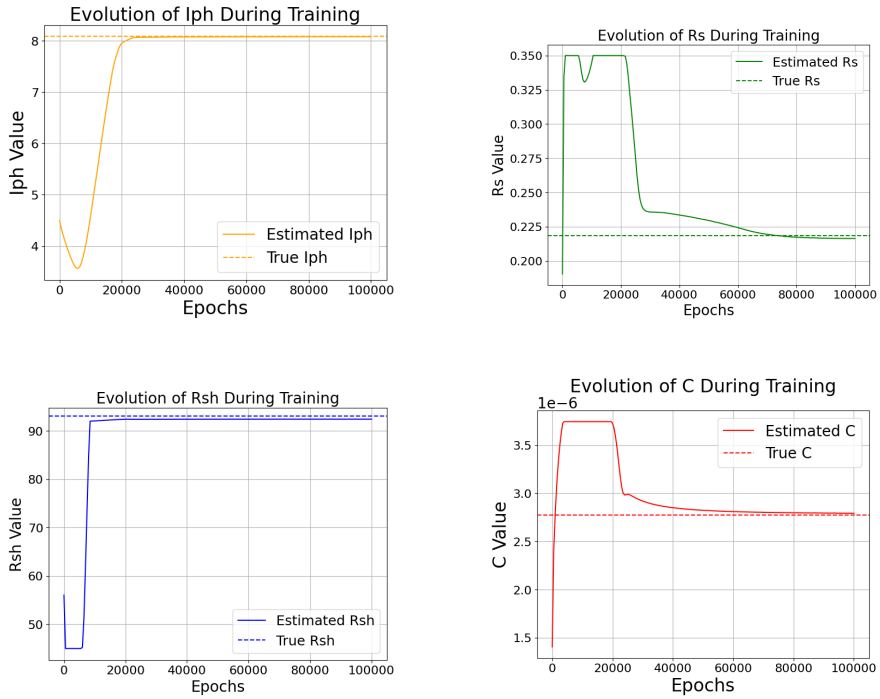

Figure 4.8: Evolution of parameters for linear case during training: R_{sh}, R_s, C, and I_{ph}.

leading to improved accuracy over time. The parameters I_{ph} and R_{sh} converge quickly and reach stable values close to their actual values. On the other hand, R_s and C take longer to stabilize and show more noticeable fluctuations during training, reflecting the higher complexity of their physical dynamics.

Fig. 4.9 shows a comparison between the predicted and true output current.

These observations confirm that the multiple PINN is capable of accurately estimating circuit parameters, although convergence speed and stability are influenced by the physical characteristics and sensitivity of each parameter.

To evaluate the effectiveness of the proposed method, its results were compared with those obtained using the GA [3]. The GA does not rely

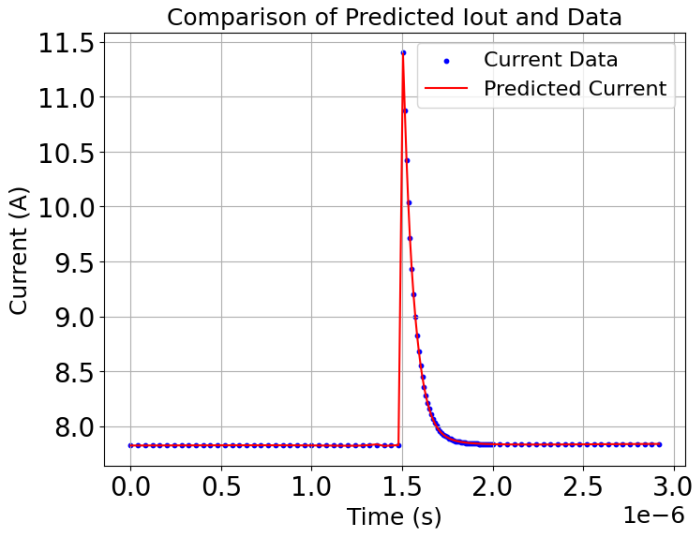

Figure 4.9: Comparison between predicted current and observed data for linear case. The plot shows the true current measurements (blue dots) and the model-predicted current (red line).

on any prior physical knowledge of the system. Instead, it operates solely based on available input-output data. To ensure a fair comparison with the multiple PINN model, the GA is configured with consistent hyperparameters based on [4]. In the GA, a population of 50 individuals is evolved over 50,000 generations. At each generation, new candidate solutions are generated through arithmetic crossover between selected parents. To maintain genetic diversity and enhance global exploration, a mutation probability of 5% is applied by introducing small random variations to the values of R_s, R_{sh}, I_{ph}, and C.

To assess the accuracy of parameter estimation, the percentage errors for each method are presented in Fig. 4.10. In this comparison, the estimation error for R_s is about 10.1% with GA and 2.9% with Multiple PINN. For R_{sh}, the errors are approximately 0.3% with GA and 0.8% with Multiple PINN, which are nearly the same. For I_{ph}, estimation with GA has an error of around 0.3% and estimation with Multiple PINN around 0.1%. For the C, the estimation error is 7.0% with GA and 1.2% with Multiple PINN.

Overall, Multiple PINN shows better accuracy in parameter estimation.

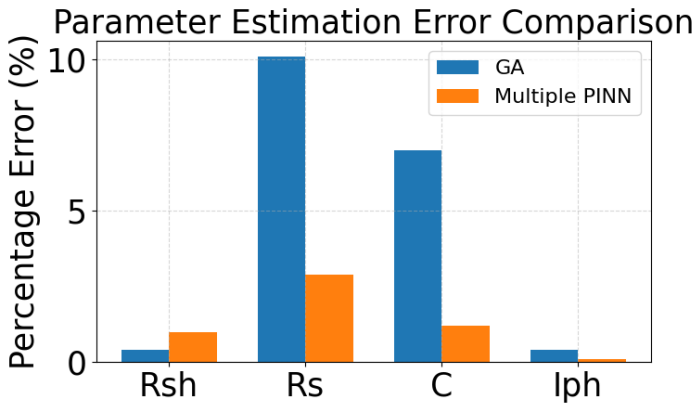

Figure 4.10: Comparison of parameter estimation errors between the GA and the proposed Multiple PINN approach with R_s term in loss function. The Multiple PINN method significantly reduces estimation errors across all parameters (R_s, R_{sh}, I_{ph}, and C), particularly for R_s and C, where the GA approach exhibits the highest error.

Based on the literature [5], uniform noise is considered one of the important types of measurement noise. This type of noise is uniformly distributed over a specific interval and is often used to simulate measurement uncertainties in physical models, including PV systems. The impact of different levels of uniform noise (from 0% to 5%) on the accuracy of parameter estimation is investigated. For each noise level, the model was 10 training times to assess the stability and variability of the estimation results. The results are illustrated in Fig. 4.11, which presents boxplots of the percentage error for parameters.

Among all parameters, R_{s} shows the highest sensitivity to noise. At 0% noise, the average percentage error is below 1%, but as noise increases to 5%, the median error rises to around 3.5%, with a noticeable increase in variability, especially between 3% and 5% noise levels. This indicates a significant drop in estimation accuracy for R_{s} in noisy conditions.

In contrast, R_{sh} demonstrates highly stable behavior. Across all noise levels, the median error remains consistently between 0.7% and 0.75%, and

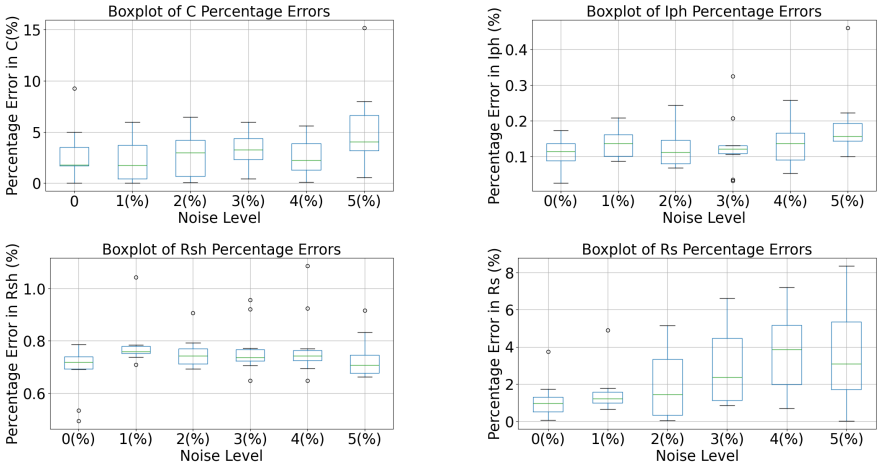

Figure 4.11: Error percentage distribution of R_{sh}, R_s , I_{ph}, and C across noise levels (0% to 5%). The bar heights represent the variations in parameter estimation due to different levels of uniform noise, while the horizontal line indicates the true value of the parameter for reference.

the maximum observed error does not exceed 1.07%. The error distributions are compact and uniform, reflecting the robustness of R_{sh} estimation against uniform noise. The parameter I_{ph} also maintains high estimation accuracy. At 0% noise, the error is around 0.1%, and even at 5% noise, the median remains as low as 0.18%. This shows that the model is highly reliable in estimating I_{ph} under noisy conditions. The parameter C is also affected by noise, though to a lesser extent than R_{s}. The median error increases from approximately 2% at 0% noise to around 4% at 5% noise. While a few outliers appear at higher noise levels, the general trend indicates a gradual increase in error with rising noise intensity.

In the next section of our analysis, we examined the nonlinear characteristics of the PV system parameters, with particular attention to the capacitor.

4.4 Nonlinear Capacitance Model

In this section, we focus on the nonlinear dynamics of the system to better capture its inherent behavior and evaluate the performance of the proposed algorithm. Specifically, we examined how the capacitor's response changes with varying voltage levels, emphasizing its voltage-dependent characteristics. The equivalent circuit considered for this analysis is shown in Fig. 3.16, which represents the nonlinear behavior of the PV system with a voltage-dependent capacitor. All subsequent model analyses are carried out based on the mathematical formulations presented in equations (19–33).

In Simulink, equation (20) is implemented as a function for C, which varies with the capacitor voltage. The value $b = 3.88 \times 10^{-16}$ F is considered a constant coefficient.

The input and output waveforms used for training are the same as those shown in Fig. 4.6 and Fig. 4.7. The number of input data points is 116, with upsampling similar to the linear model.

To train the network, we use the loss function defined in equation (33). The range considered for each parameter is shown in Table 5.3.

Table 4.3: Parameter Ranges for the Estimation Process

Parameter	**Range**
I_{ph}	[0.1A, 12A]
R_s	[0.1Ω, 0.35Ω]
R_{sh}	[45Ω, 140Ω]
b	$[0.94 \times 10^{-16}\,\text{F},\ 6.82 \times 10^{-16}\,\text{F}]$

The network structure used for parameter estimation follows the configuration presented in Table 5.3.

For the estimation of b and R_s, Network 1 is used to ensure better learning performance and convergence. In contrast, for estimating I_{ph} and

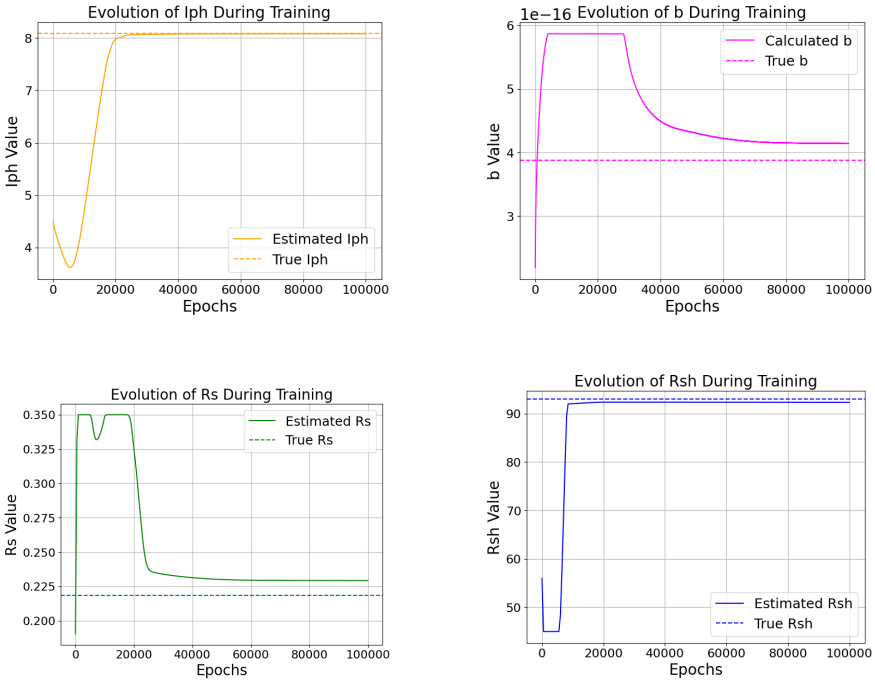

Figure 4.12: Evolution of parameters for linear case during training: R_{sh}, R_s, b, and I_{ph}.

R_{sh}, which show more stable behavior and are less sensitive to noise, Network 2 is applied. Fig. 4.12 shows how the parameter estimates change and improve during training.

Fig. 4.13 shows a comparison between the predicted and true output current.

Fig. 4.14 compares parameter estimation errors of a nonlinear model with and without including the R_s term in the loss function. As shown, incorporating the R_s term in the loss function significantly improves the accuracy of R_s and b estimation, leading to lower overall errors.

Fig. 4.15 shows a comparison of parameter estimation errors between the standard PINN and the Multiple PINN approach for the nonlinear case. The results indicate that the Multiple PINN significantly reduces the percentage error, especially for sensitive parameters such as R_s and b.

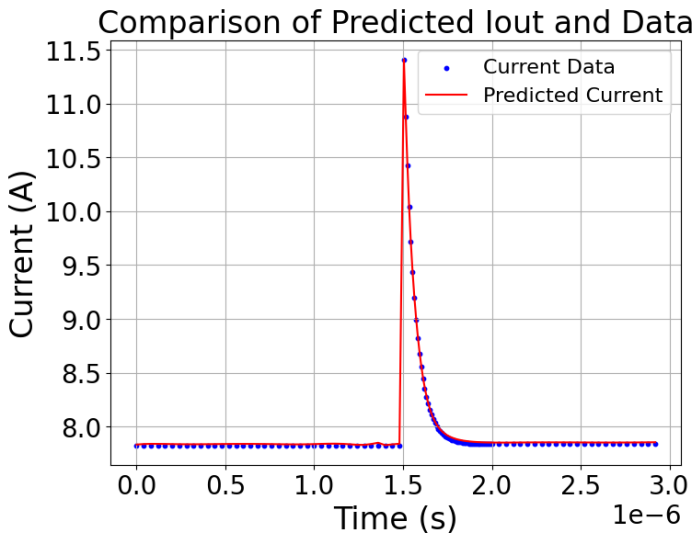

Figure 4.13: Comparison between predicted current and observed data for nonlinear case. The plot shows the true current measurements (blue dots) and the model-predicted current (red line).

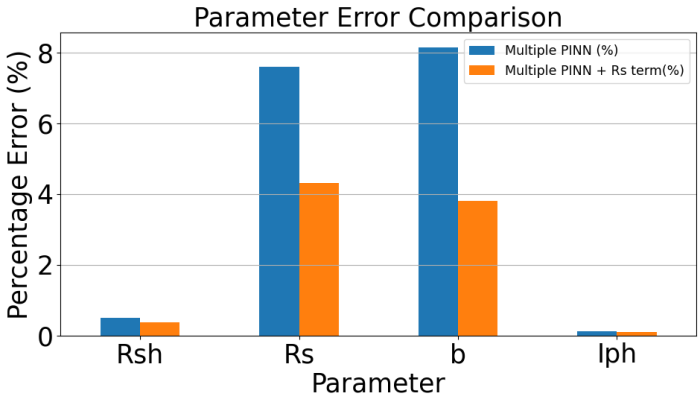

Figure 4.14: Comparison of parameter estimation error with and without the inclusion of the R_s term in the loss function. Including the R_s-dependent physical constraint significantly reduces the percentage error for the R_s and b parameters, improving model accuracy. The R_{sh} and I_{ph} parameters show only minor changes, indicating less sensitivity to this term in the loss formulation.

Similar to the linear model, the nonlinear model was also evaluated using a GA and compared under the same conditions to allow a clear and consistent comparison of performance. To assess the accuracy of parameter

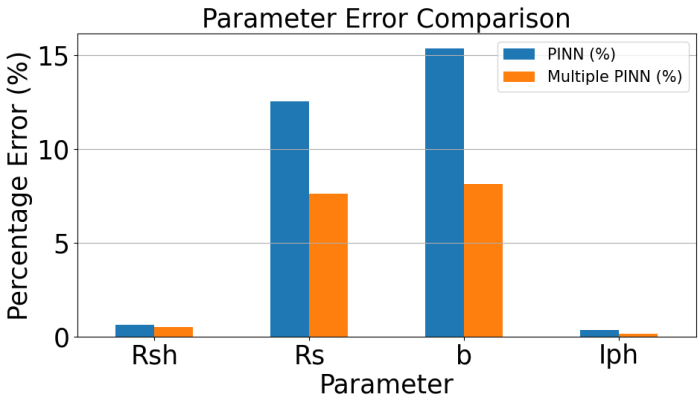

Figure 4.15: Comparison of parameter estimation error between a PINN and a Multiple-PINN architecture. The use of multiple PINNs significantly reduces the percentage error in estimating R_s and b, which are typically more sensitive to data dynamics.

estimation, the percentage errors for each method are presented in Fig. 4.16. In this comparison, the estimation error for R_s is about 8.0% with GA and 4.3% with Multiple PINN. For R_{sh}, the errors are approximately 0.7% with GA and 0.6% with Multiple PINN, which are nearly the same. For I_{ph}, GA has an error of around 0.1% and Multiple PINN around 0.2%. For the parameter b, the error is 16.1% with GA and 3.8% with Multiple PINN. Overall, Multiple PINN shows better accuracy in parameter estimation compared to GA.

Following the same approach used for the linear model, the effect of uniform noise was also examined for the nonlinear case.

Noise levels ranging from 0% to 5% were applied to the input data in order to evaluate the stability and reliability of parameter estimation. The resulting percentage errors are illustrated in Fig. 4.17. The parameter R_s While the median error remained below 5% in the absence of noise, it reached approximately 10% at 3% and 4% noise, and stayed at a similar level under 5% noise. This trend indicates a sensitivity of R_s to noise in the nonlinear model. In contrast, the estimation of R_{sh} was only slightly affected. The median error increased modestly from around 0.6% at 0% noise to about

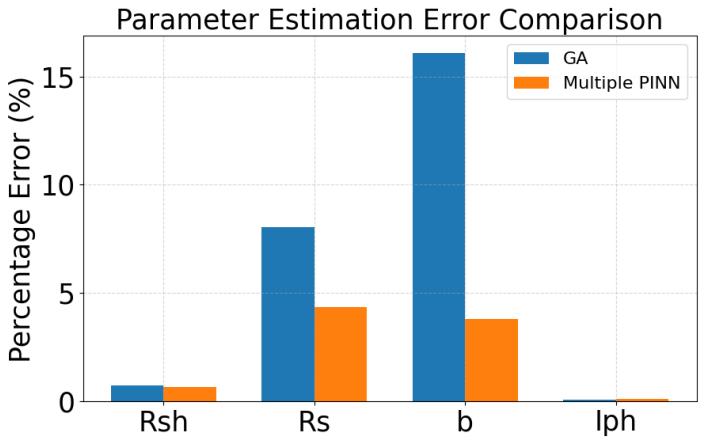

Figure 4.16: Parameter estimation error comparison between the GA and the proposed Multiple PINN approach, including the nonlinear parameter b with R_s term in loss function. The Multiple PINN significantly reduces the error for both linear parameters (R_s, R_{sh}, I_{ph}) and the nonlinear parameter b, which shows the highest discrepancy in GA results.

2.2% at 5%, with limited variation across samples. This suggests that R_{sh} is relatively stable and less sensitive to noise. For I_{ph}, the error remained consistently low. It increased only marginally, from below 1% without noise to approximately 1% at the highest noise level, indicating that this parameter is highly robust against noise. The parameter b exhibited a more noticeable response. The median error rose from around 2% at 0% noise to nearly 8% at 5% noise, along with a broader distribution of error values. This reflects a decline in estimation accuracy as noise increases.

Overall, the nonlinear model shows a higher sensitivity to noise compared to the linear case. While some parameters such as R_{sh} and I_{ph} remain relatively unaffected, others demonstrate greater vulnerability under noisy conditions.

This chapter extended the baseline framework by introducing a Multiple PINN architecture to enhance the robustness and accuracy of parameter estimation in dynamic photovoltaic models. The chapter began by analyzing the limitations of standard PINNs under reduced data resolution and measurement noise, highlighting how insufficient sampling in transient regions

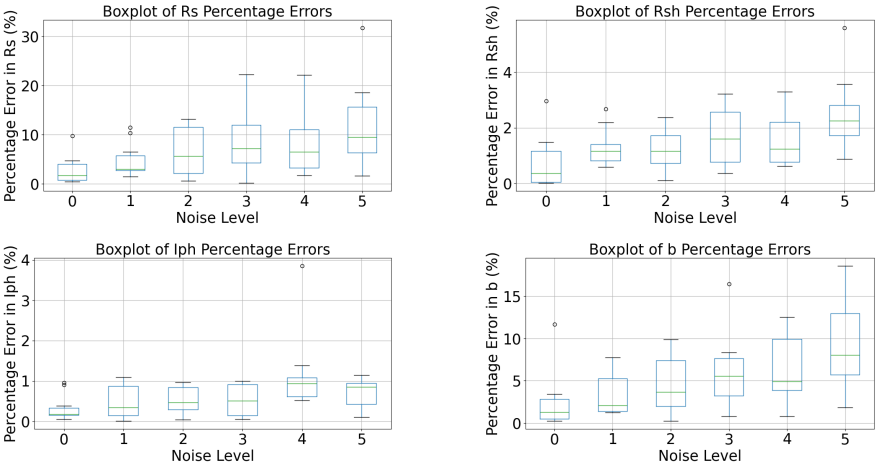

Figure 4.17: Error percentage distribution of R_{sh}, R_s , I_{ph}, and b across noise levels (0% to 5%). The bar heights represent the variations in parameter estimation due to different levels of uniform noise, while the horizontal line indicates the true value of the parameter for reference.

could lead to biased estimation of parameters. To address this limitation, the proposed Multiple PINN structure developed the learning process by assigning independent subnetworks to different groups of parameters according to their physical behavior and time response. While one subnetwork focused on transient parameters, another subnetwork estimated other parameters. All subnetworks were governed by the same physical equations embedded within the loss function. The chapter presented the detailed network design, training configuration, and validation through simulated case studies based on the dynamic SDM. The results demonstrated that the Multiple PINN significantly improved convergence stability and maintained high accuracy even with noisy or downsampled data. Compared to a single PINN and optimization-based methods such as Genetic Algorithms, the Multiple PINN achieved stronger resilience to measurement uncertainties. This development highlighted an important advancement in the proposed framework, establishing a scalable and physically consistent approach to parameter identification in PV systems. The results confirmed that dividing the learning process across multiple physics-informed subnetworks allowed for a more efficient

representation of parameter dynamics. Based on this analysis, the proposed approach was able to accurately estimate the parameter values of the system, demonstrating its capability in capturing the nonlinear characteristics of the PV model. However, one of the most critical factors influencing the overall performance and stability of such models is the environmental condition, particularly solar irradiance and temperature which directly affect the current–voltage characteristics and dynamic response of the system. These environmental effects are therefore examined in detail in the next chapter, where a new network architecture is proposed to explicitly account for these dependencies and improve the model's adaptability under varying operating conditions.

References

[1] S. Zhao, Y. Peng, Y. Zhang, and H. Wang, "Parameter Estimation of Power Electronic Converters With Physics-Informed Machine Learning," IEEE Transactions on Power Electronics, vol. 37, no. 10, pp. 11567–11578, Oct. 2022, doi: 10.1109/TPEL.2022.3176468..

[2] E. Haghighat, M. Raissi, A. Moure, H. Gomez, and R. Juanes, "A physics-informed deep learning framework for inversion and surrogate modeling in solid mechanics," Computer Methods in Applied Mechanics and Engineering, vol. 379, pp. 113741, 2021, doi: 10.1016/j.cma.2021.113741.

[3] J. D. Bastidas-Rodriguez, G. Petrone, C. A. Ramos-Paja, and G. Spagnuolo, "A genetic algorithm for identifying the single diode model parameters of a photovoltaic panel," *Mathematics and Computers in Simulation*, vol. 131, pp. 38–54, 2017. doi: 10.1016/j.matcom.2015.12.003.

[4] J. Montano, L. F. Grisales Noreña, A. Tobón, and D. Gonzalez Montoya, "Estimation of the parameters of the mathematical model of an equivalent diode of a photovoltaic panel using a continuous genetic algorithm," *IEEE Latin America Transactions*, vol. 20, no. 4, pp. 616–623, Apr. 2022. doi: 10.1109/TLA.2022.9759926.

[5] J. Stiasny, G. S. Misyris, and S. Chatzivasileiadis, "Physics-informed neural networks for non-linear system identification for power system dynamics," *2021 IEEE Madrid PowerTech*, pp. 1–6, 2021, doi: 10.1109/PowerTech46648.2021.9495063.

Chapter 5

5

Two-Level Layered Physics-Informed Neural Networks

5.1 Introduction

The behavior of the depletion capacitance (C) in photovoltaic (PV) semiconductors plays a crucial role in describing the dynamic response of the system. This capacitance originates from the separation of charge carriers within the p–n junction, forming a space-charge region whose width varies with the applied electrical conditions. As reported in [1], the value of C depends on the instantaneous voltage and current applied to the module, since these quantities directly influence the charge distribution within the junction. Under transient conditions, the continuous redistribution of carriers and the evolution of the internal electric field lead to a time-varying and inherently nonlinear capacitance behavior.

The equivalent circuit used for this analysis is shown in Fig. 3.16, representing the nonlinear dynamics of the PV system with a voltage-dependent capacitor. In earlier nonlinear model, the capacitance was assumed to depend solely on the terminal voltage. In contrast, the present work extends this representation by considering both voltage and current dependencies, which allows the model to capture the coupled nonlinear interactions be-

tween electrical and dynamic effects more accurately.

Additionally, environmental factors such as irradiance and temperature are integrated into the model, as they significantly affect both the capacitance and the current–voltage characteristics of the PV cell. This enhanced nonlinear model therefore provides a more realistic description of the PV module's dynamic behavior under real operating conditions, where environmental variations and electrical transients occur simultaneously.

In the following sections, the focus is placed on the modeling and development of a PINN framework based on the challenges identified in this nonlinear formulation. The proposed model is designed to accurately capture the dynamic behavior of the PV system by incorporating both electrical and environmental dependencies. Through this approach, the PINN is trained to learn the underlying physical relationships governing the system, enabling robust estimation of parameters and improved prediction of transient responses under realistic operating conditions.

5.2 Nonlinear model of PV

Fig. 5.1 illustrates the SDM of the PV module, in which the diode is replaced by a non-linear capacitance that varies with both current and voltage [1, 2].

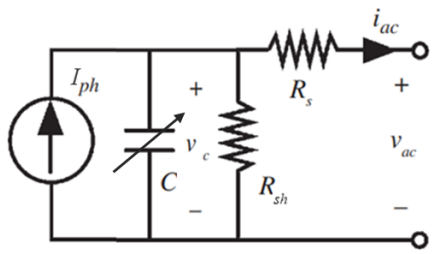

Figure 5.1: Dynamic and nonlinear SDM of the PV module that varies with both current and voltage.

The following expression defines the capacitance model as a function of both voltage and current:

$$C(V_{ac}(t), i_{ac}(t)) = \frac{C_{j0}}{\sqrt{1 + \frac{(V_{ac}(t) + R_s i_{ac}(t))}{V_j}}} \tag{1}$$

In equation (1), C_{j0} represents the junction capacitance, while V_j refers to the built-in junction. These parameters define how the depletion capacitance changes with voltage in the circuit model. The current through the capacitor is obtained by differentiating the charge with respect to time. Assuming $Q(t) = C(v_c(t)) \cdot v_c(t)$, the expression for charge becomes:

$$Q(t) = \frac{C_{j0} V_{ac}(t)}{\sqrt{1 + \frac{(V_{ac}(t) + R_s i_{ac}(t))}{V_j}}} \tag{2}$$

The capacitive current can be expressed as the time derivative of the charge:

$$i_c(t) = \frac{dQ(t)}{dt} = \frac{d}{dt}\left(\frac{C_{j0} V_{ac}(t)}{\sqrt{1 + \frac{(V_{ac}(t) + R_s i_{ac}(t))}{V_j}}}\right) \tag{3}$$

The capacitive current can also be written as:

$$i_c(t) = C_{j0} \frac{d}{dt}\left(\frac{V_{ac}(t)}{\sqrt{1 + \frac{(V_{ac}(t) + 2R_s i_{ac}(t))}{V_j}}}\right) \tag{4}$$

According to Kirchhoff's current law, the photogenerated current I_{ph} is divided among the capacitive current $i_c(t)$, the current through the shunt resistor $i_{R_{\text{sh}}}(t)$, and the output current $i_{\text{ac}}(t)$, leading to the following relation:

$$I_{ph} - i_c(t) - i_{R_{sh}}(t) - i_{ac}(t) = 0 \tag{5}$$

The current flowing through the shunt resistance is:

$$i_{R_{sh}}(t) = \frac{v_c(t)}{R_{sh}} \tag{6}$$

So we have:

$$i_{ac}(t) = I_{ph} - C_{j0}\frac{d}{dt}\left(\frac{V_{ac}(t)}{\sqrt{1+\frac{(V_{ac}(t)+2R_s i_{ac}(t))}{V_j}}}\right) - \frac{v_c(t)}{R_{sh}} \tag{7}$$

And the voltage-current relationship is:

$$v_c(t) = V_{ac}(t) - R_s i_{ac}(t) \tag{8}$$

Using this relation in the total current equation gives:

$$\frac{(v_c(t) - V_{ac}(t))}{R_s} = I_{ph} - C_{j0}\frac{d}{dt}\left(\frac{V_{ac}(t)}{\sqrt{1+\frac{(V_{ac}(t)+2R_s i_{ac}(t))}{V_j}}}\right) - \frac{v_c(t)}{R_{sh}} \tag{9}$$

The final equation becomes:

$$\frac{d}{dt}\left(\frac{V_{ac}(t)}{\sqrt{1+\frac{(V_{ac}(t)+2R_s i_{ac}(t))}{V_j}}}\right) = \frac{1}{C_{j0}}\left(I_{ph} + \frac{V_{ac}(t)}{R_{sh}} - v_c(t)\left(\frac{1}{R_{sh}} + \frac{1}{R_s}\right)\right) \tag{10}$$

Equation (10) describes the nonlinear variations of the junction capacitance with respect to the input voltage and current.

According to the literature [3], several essential parameters of SDM depend on irradiance (G) and temperature (T). The equations are as follows:

$$I_{ph}(G,T) = \frac{G}{G_{STC}}\left[I_{ph,STC} + \alpha(T - T_{STC})\right] \tag{11}$$

$$R_s(G,T) = R_{s,STC} \tag{12}$$

$$R_{sh}(G,T) = R_{sh,STC} \cdot \frac{G_{STC}}{G} \tag{13}$$

We considered the value for $R_{s,STC}$, $R_{sh,STC}$, $I_{ph,STC}$ based on Table 3.1. G_{STC} and T_{STC} are the irradiance and temperature under STC

condition ($G_{STC} = 1000$ W/m^2, $T_{STC} = 25°$C). α is the temperature coefficient of the current and $\alpha = 3.18$ mA/°C based on Table 3.1.

From equations (11)–(13), it can be observed that the SDM parameters are functions of G and T. Therefore, estimating G and T using the step waveform and step response waveform is sufficient to determine the dependent parameters, eliminating the need to estimate them separately. In the first step of the analysis, the series resistance R_s is considered constant, following the assumptions commonly adopted in the literature. This simplification allows for an initial evaluation of the model performance and provides a reference for comparing the results obtained in the subsequent adaptive estimation stages.

On the other hand, C_{j0} in equation (10) represents the junction capacitance. Its explicit dependence on irradiance G and temperature T is not established in the literature. In this study, C_{j0} is considered as an independent dynamic component and is estimated separately. Based on the identified electrical and environmental characteristics, a new PINN model was developed to address these features and capture the system's dynamic behavior more effectively. The details of this model are discussed in the following section.

5.3 Two-level layered physics informed neural network

To better capture the complex interactions between the electrical and environmental variables of the PV system, an enhanced PINN architecture was designed. This model integrates both physical knowledge and data-driven learning to account for the nonlinear dependencies introduced by irradiance and temperature variations. It aims to simultaneously estimate the system parameters and the environmental conditions influencing them, providing a unified and adaptive modeling framework. The architecture includes two connected neural subnetworks. The parameters I_{ph}, R_s, and R_{sh}

themselves depend on environmental conditions such as irradiance G and temperature T. The parameter C_{j0} is treated separately from R_s, R_{sh}, and I_{ph} because the model does not express it as a function of temperature or irradiance, but only as dependent on voltage and current. These dependencies are implicitly encoded in the first layer of the proposed two-level layered PINN (Fig. 4.3), which receives voltage and current over time and learns to estimate G and T. This layer starts by minimizing the loss associated with environmental variables and system-level behavior, where the loss function is constructed based on the governing differential equation (10). As the training progresses and the error in estimating G and T decreases, the network gradually enables the second layer to refine the output dynamics by focusing on the internal parameter C_{j0}, which appears explicitly in the differential structure of equation (10). Once the external conditions are sufficiently captured and the system behavior stabilizes, the second layer effectively starts to learn C_{j0} with higher accuracy. This staged training process prevents interference between parameter spaces and allows the model to better capture the nonlinear transient behavior of the PV system. The layered strategy ensures that learning follows the structure of the physical model, improving both robustness and accuracy.

Table 5.1 summarizes the architectures of the two-level layered PINN used to estimate the parameters. C_{j0} has a more complex and nonlinear behavior. Batch normalization, residual connections, and layer normalization are used to improve learning and estimation accuracy for C_{j0}. Batch normalization stabilizes training by reducing internal covariate shift, while residual connections improve gradient flow. Layer normalization is also applied to enhance robustness, particularly in deeper layers. The use of a two-level layered PINN architecture improves the overall estimation performance by decoupling the learning of global and local parameters. Estimating irradiance and temperature in the first stage allows the second stage to operate on more physically-informed inputs, resulting in faster convergence, reduced training complexity, and improved accuracy in estimating C_{j0} that changes with voltage and current.

Table 5.1: Network architecture designed based on the behavioral differences of parameter C_{j0}.

Network Information	**Network for C_{j0}**	**Network for T, G**
Number of Layers	28	30
Neurons per Layer	3	3
Activation Function	Tanh	Tanh
Optimizer	AdamW	AdamW
Learning Rate	2×10^{-4}	5×10^{-4}
L2 Regularizer	1×10^{-8}	1×10^{-8}
Epochs	50001	50001
Batch Normalization	Yes	No
Residual Connections	Yes	No
Layer Normalization	Yes	No

Also, the loss function is formulated as presented in equation (14).

$$\begin{aligned}\mathcal{L}(t,\theta) = \frac{1}{M}\sum_{i=1}^{M}\left(\left[\frac{dV_c}{dt} - u_{\text{PINN}}(t_i;\theta)\right]^2\right) \\ + \lambda_1 \cdot \frac{1}{M}\sum_{j=1}^{M}\left(u_{\text{PINN}}(t_j;\theta) - u_{\text{obs}}(t_j)\right)^2 \\ + \lambda_2 \cdot \frac{1}{M}\sum_{k=1}^{M}\left([I_{\text{ph,STC}} + \alpha(T - T_{\text{STC}})] \cdot u_{\text{PINN}}(t_k;\theta)\right)\end{aligned} \tag{14}$$

The loss function in equation (14) is composed of three main terms, each reflecting a different aspect of the learning objective. The first term represents the physics-based component, which penalizes the discrepancy between the predicted value $u_{\text{PINN}}(t;\theta)$ and the time derivative of the capacitor voltage $\frac{dV_c}{dt}$. This term ensures that the neural network's output adheres to the governing differential equation, thus embedding physical consistency into the training process. The second term, corresponds to the data-driven loss, which minimizes the error between the model's predictions

and the observed measurements $u_{\text{obs}}(t)$. This term helps guide the learning process using available data and becomes especially important in estimating parameters with highly nonlinear behavior, such as C_{j0}. The coefficient λ_1 controls the contribution of the data-driven term. The third term, introduces temperature dependence into the loss formulation. Including this term helps the network attribute temperature-induced variations to the correct physical sources, improving estimation accuracy and preventing parameter cross-dependency [4]. To ensure its impact is properly captured, it is weighted by λ_2. As shown in Fig. 5.2, without including T in the loss function, the model misattribute temperature effect to other parameters, resulting in biased estimates. According to (14) in our loss function framework, $M = 150$ represents the number of training samples used for the data loss. The loss weighting factors are empirically set to $\lambda_1 = 1000$ for the data loss, ensuring that the model closely fits the observed data, and $\lambda_2 = 10$ to maintain the temperature effect's influence without letting it dominate the training process. We have searched for the best value for λ_1, λ_2 in the range $[1, 1500]$ using 100 steps.

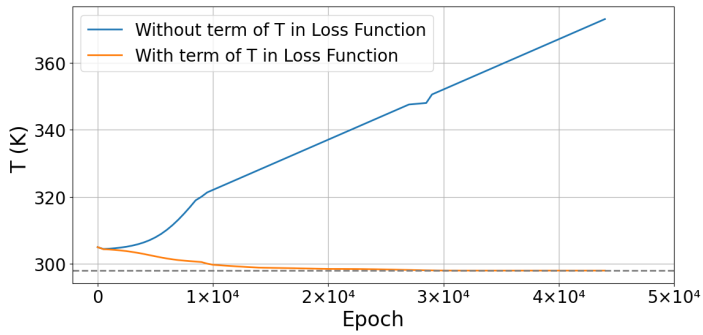

Figure 5.2: Effect of including the temperature term in the loss function. The model without the T term in loss function (blue curve) becomes unstable, while the model with the T term in loss function (orange curve) converges smoothly.

For input data, only the transient part of the current is used, and the dataset consists of 150 samples containing voltage and current values over time. Using only the transient region helps reduce the amount of data and improves the efficiency of training as well as the accuracy of parameter esti-

mation. The structure shown in Fig. 5.3 represents a two-level layered PINN developed for parameter estimation in PV systems. This model combines measurement data with physical laws described by differential equations.

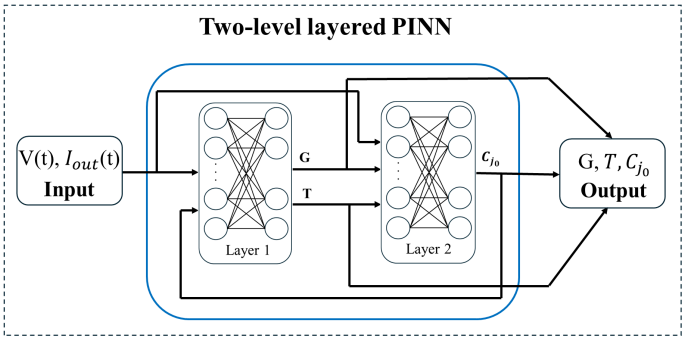

Figure 5.3: Architecture of the proposed two-level layered PINN. The Layer 1 focuses on estimating the G and T. These estimates are then used by the Layer 2 to refine the model output and estimate the junction C_{j0}.

Fig.5.4 illustrates the impact of using a on-level layered PINN versus a two-level layered PINN architecture, where the percentage error of each parameter is compared to evaluate the performance of both models. Table 5.2 summarizes the value ranges used in the training process. The initial values for all parameters are randomly assigned, and the model is trained using 150 data points taken from the transient region of the current response.

Table 5.2: Value ranges used for each parameter during training

Parameter	**Range**
G	$[700\,W/m^2,\ 1500\,W/m^2]$
T	$[270\,\mathrm{K},\ 320\,\mathrm{K}]$
C_{j0}	$[0.1 \times 10^{-7}\mathrm{F},\ 3.5 \times 10^{-7}\mathrm{F}]$

The output current is illustrated in Fig. 5.5, demonstrating that the response predicted by the PINN closely matches the true output throughout

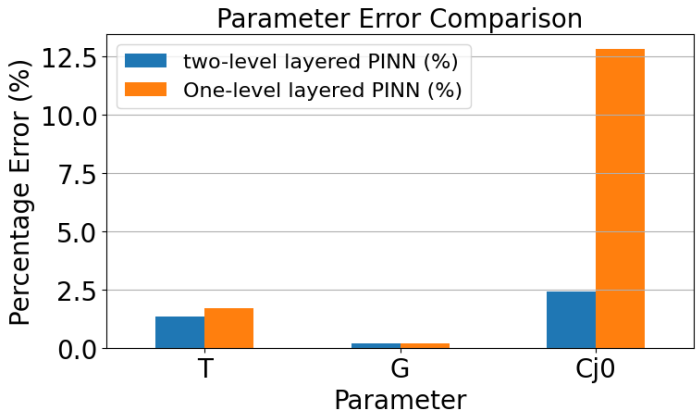

Figure 5.4: Comparison of parameter estimation errors between the one-level layered PINN and the two-level layered PINN approach. The results show that while both methods achieve low errors for parameters T and G, the two-level layered PINN significantly reduces the estimation error for C_{j0}, indicating its superior ability to capture complex parameter dynamics.

the transient region.

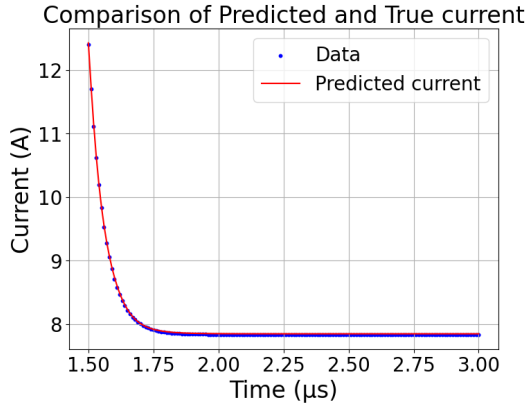

Figure 5.5: Comparison of simulated $i_{ac}(t)$ and Two-level layered PINN-identified waveform.

Fig. 5.6 presents the convergence behavior of the estimated parameters T, G, and C_{j0} over the training epochs. As illustrated, all parameters gradually converge to their true values over time, which are considered reference values under STC. The values of T and G are defined under STC

as $T = 298°\text{k}$ and $G = 1000\,\text{W/m}^2$, and the value of C_{j0} is taken to be $1.6 \times 10^{-7}\,\text{F}$. This consistency supports the assumption that the network effectively identifies the underlying physical parameters governing the system dynamics during training.

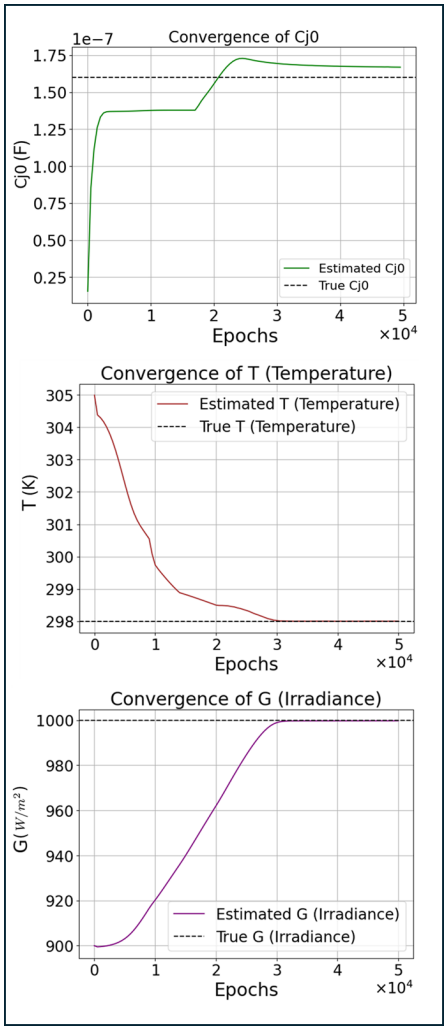

Figure 5.6: Evolution of parameters during training: G, T, and C_{j0}.

Similar to the previous chapter, other methodes employed for parameter estimation to provide a comparative benchmark. To evaluate the performance of different estimation methods, the percentage errors for each parameter are presented in Fig. 5.7. To ensure a fair comparison with the

proposed PINN model, both GA and PSO were implemented with consistently tuned configurations. According to the literature [5], more robust hyperparameters were employed to improve the accuracy of parameter estimation using GA and PSO.

For the GA, we use a population size of 50 and run the optimization over 50,000 generations. Parent solutions combine using arithmetic crossover, and mutations are introduced with a 5% probability by applying small perturbations to the C_{j0}, T, and G values.

For the PSO, we use a swarm size of 50 and conduct the optimization over 50,000 generations within the same search space. The inertia weight is set to 0.7, and both the cognitive and social acceleration coefficients are fixed at 1.5 to balance exploration and exploitation.

Both methods use the parameter boundaries defined in Table 5.2, and these values are determined through empirical testing.

In contrast, the PINN integrates both input data and the underlying physical laws governing the system, leading to more informed and potentially more accurate estimations. All the methods demonstrate strong performance in estimating the (T) and (G), with comparable and minimal percentage errors. However, a significant discrepancy arises in the estimation of C_{j0}. The two previous methods, exhibit noticeably higher errors, suggesting that relying solely on observed data insufficient for accurately capturing the complex behaviour of C_{j0}.

Figure 5.7: Comparison of percentage errors in estimating the parameters C_{j0}, G, and T using GA, PSO, and PINN. While all three methods show similar and low errors for G and T, the PINN significantly outperforms the data-driven approaches (GA and PSO) in estimating C_{j0}, demonstrating its advantage in capturing more complex system behaviors.

To examine how noise influences the parameter identification process, according to [6], Gaussian noise with levels from 0% to 5% is added to the $i_{ac}(t)$ samples. Figure 5.8 shows how increasing noise levels affect the accuracy of the estimated output current, with RMSE increasing consistently from 0% to 5%.

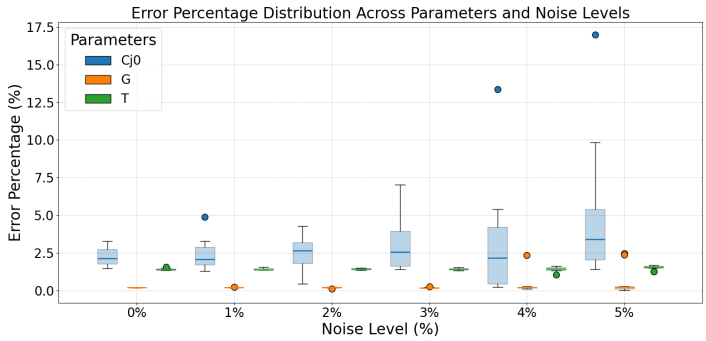

Figure 5.8: RMSE values for different noise levels affect the accuracy of the estimated output current

Fig. 5.9 presents the percentage error distributions for the estimated parameters C_{j0}, G, and T under different levels of Gaussian noise (0% to 5%) added to the $i_{ac}(t)$. For each noise level, the experiment was repeated 10 times to ensure statistical reliability, and the results reflect the variability and robustness of the estimation process under noisy conditions.

The estimation error of C_{j0} for 10 times increases from approximately 2.1% at 0% noise to around 5.3% at 5% noise, with noticeable growth in variance and outliers beyond 3% noise. For parameter G, the error remains consistently low, increasing slightly from 0.23% to 0.29% across all noise levels. Similarly, the median error of T changes from about 1.4% at 0% noise to 1.7% at 5%, showing only a marginal increase. These results indicate that C_{j0} is significantly more affected by noise compared to G and T. These box plots effectively capture both the central tendency (median error) and the spread (variance and presence of outliers) of the estimation accuracy under noisy conditions. A wider interquartile range and larger number of outliers, especially in the case of C_{j0}, indicate greater sensitivity and higher

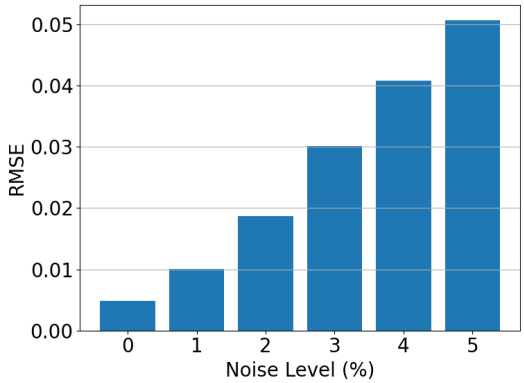

Figure 5.9: Distribution of error percentages in estimating parameters C_{j0}, G, and T across different Gaussian noise levels (0% to 5%) applied to $i_{ac}(t)$. As the noise level increases, the estimation error for C_{j0} shows greater variation and sensitivity compared to G and T, which remain relatively stable and less affected.

estimation uncertainty due to noise. This heightened sensitivity of C_{j0} to noise can be attributed to its physical role in the system. As a junction capacitance, C_{j0} primarily governs the transient response of the circuit during high-frequency or switching conditions. In such transition regions, small fluctuations in the current or voltage can lead to disproportionately large variations in the estimated capacitance due to its nonlinear dependence on voltage. Unlike parameters such as G or T, which influence the steady-state characteristics more directly and are inferred from longer-term signal behavior, C_{j0} is inherently linked to fast, high-frequency dynamics where noise has a more immediate and amplified effect.

In this analysis, the series resistance R_s was kept constant according to the assumptions commonly adopted in the literature, since its variation was considered to have a secondary influence compared to other parameters. However, R_s plays a crucial role in shaping the transient response and overall accuracy of the electrical model. Therefore, in the following section, R_s is also estimated together with G, T, and C_{j0} to further assess the robustness and generalization capability of the proposed model.

5.4 Extended Parameter Estimation Including R_s

In the previous section, R_s is following STC assumptions. However, because R_s is highly sensitive to system degradation and fault conditions, excluding it from the estimation process limits the model's ability to extract meaningful diagnostic information. Therefore, the current framework treats R_s as an estimable parameter and includes it in the training process. Similar to the previous cases, the training data were obtained from the Simulink model under the same operating conditions. The model assigns random initial values to all parameters and trains using 150 data points taken from the transient region of the current response. The output current appears in Fig. 5.10, which shows that the response predicted by the PINN closely matches the true output throughout the transient region. The network structure for parameter estimation follows the configuration presented in Table 5.3. Figure 5.11 illustrates the convergence of the estimated parameters.

Table 5.3: Value Ranges Used for Each Parameter During Training

Parameter	**Range**
G	$[100\,\mathrm{W/m^2},\ 2500\,\mathrm{W/m^2}]$
T	$[0\,\mathrm{K},\ 400\,\mathrm{K}]$
R_s	$[0.1\Omega,\ 0.35\Omega]$
C	$[125 \times 10^{-9}\,\mathrm{F},\ 375 \times 10^{-9}\,\mathrm{F}]$

Given that the transient parts of the signal typically contain high-frequency components and rapid variations, the model applies upsampling in those regions to improve the accuracy of parameters like C_{j0}, which are particularly sensitive to transient behavior. By increasing the resolution

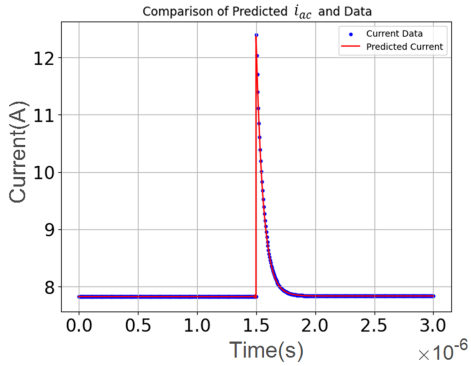

Figure 5.10: Comparison between predicted current and observed data. The plot shows the true current measurements (blue dots) and the model-predicted current (red line).

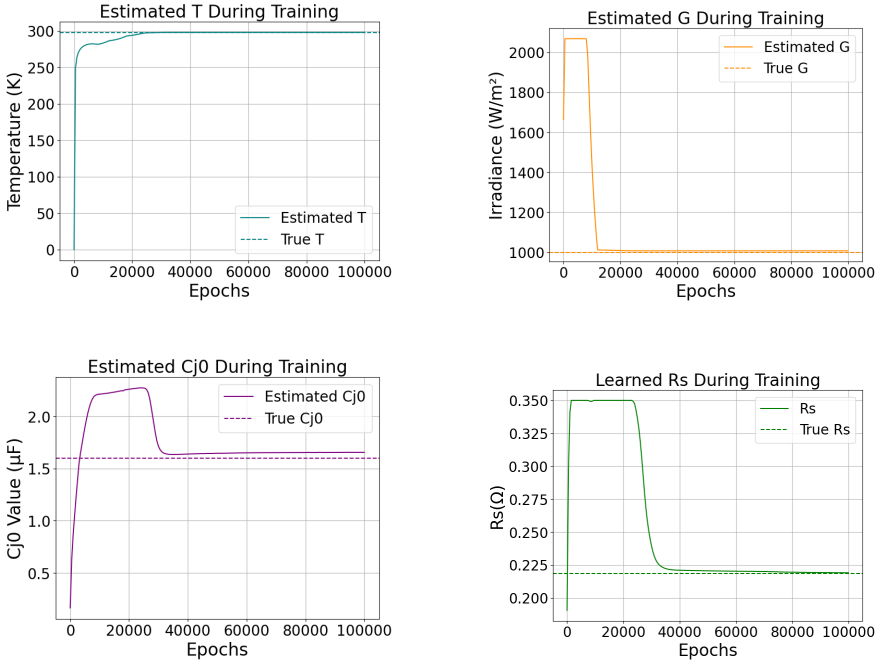

Figure 5.11: Evolution of parameters during training: R_s, C_{j0}, T, and G.

in these regions, the model captures more detailed information about the system's dynamic response. The effect of this modification appears in the improved convergence of C_{j0} and its increased robustness to noise in the final

estimation.In the previous configuration, only the transient portion of the signal was considered for parameter estimation, as it carries most of the dynamic information required for identifying parameters such as C_{j0} . However, since the series resistance R_s mainly affects the steady-state characteristics and the voltage drop before the transient occurs, it cannot be accurately estimated without considering the steady-state segment. Therefore, in the extended analysis, both transient and pre-transient parts of the signal are incorporated, enabling the model to capture a more complete system behavior and to achieve more accurate and physically consistent estimation of R_s, G, T, and C_{j0} .

In general, in this chapter we improved the PINN framework by developing a Two-Level Layered PINN designed to capture the nonlinear, irradiance-, and temperature-dependent behavior of photovoltaic systems. The chapter introduced an advanced modeling strategy in which the nonlinear capacitance was formulated as a function of both voltage and current, allowing the network to account for dynamic effects under varying operating conditions. This formulation was based on the dynamic SDM. The proposed Two-Level Layered PINN architecture consisted of two interconnected learning levels. The first level estimated the environmental parameters, while the second level focused on the transient dynamics and estimated the junction capacitance parameter (C_{j0}) from the electrical responses, leveraging the G and T values predicted by the first level. Both levels were trained under shared physical constraints to maintain internal consistency between the electrical and environmental domains. This network design enabled the model to infer unmeasured external conditions directly from the observed circuit dynamics. Simulation results validated the effectiveness of the Two-Level Layered PINN in accurately reconstructing both circuit parameters and environmental variables under noisy and dynamic conditions. This chapter represented a significant advancement in the proposed framework, transforming the PINN approach from a parameter-estimation tool into a comprehensive diagnostic model capable of real-time inference of both electrical parameters and operating conditions in photovoltaic systems. In the next chapter we will discuss

about exprimental mesurment and analysis.

References

[1] M. De Riso, I. Matacena, S. Daliento, and P. Guerriero, "Impedance Spectroscopy as On-Field Monitoring Technique for PV Modules," in *Proc. 2024 19th Conf. Ph.D. Research in Microelectronics and Electronics (PRIME)*, Larnaca, Cyprus, 2024, pp. 1–4, doi: 10.1109/PRIME61930.2024.10559699.

[2] N. Femia, G. Petrone, G. Spagnuolo, and M. Vitelli, *Power Electronics and Control Techniques for Maximum Energy Harvesting in Photovoltaic Systems*. Boca Raton, FL: CRC Press, 2017.

[3] M. Piliougine, P. Sánchez-Friera, and G. Spagnuolo, "Comparative of IEC 60891 and other procedures for temperature and irradiance corrections to measured I–V characteristics of photovoltaic devices," *Energies*, vol. 17, no. 3, p. 566, 2024.

[4] A. Kendall, Y. Gal, and R. Cipolla, "Multi-task learning using uncertainty to weigh losses for scene geometry and semantics," in *Proc. IEEE Conf. Computer Vision and Pattern Recognition (CVPR)*, Salt Lake City, UT, USA, 2018, pp. 7482–7491.

[5] J. Montano, L. F. Grisales Noreña, A. Tobón, and D. Gonzalez Montoya, "Estimation of the parameters of the mathematical model of an equivalent diode of a photovoltaic panel using a continuous genetic algorithm," *IEEE Latin America Transactions*, vol. 20, no. 4, pp. 616–623, Apr. 2022, doi: 10.1109/TLA.2022.9759926.

[6] J. Stiasny, G. S. Misyris, and S. Chatzivasileiadis, "Physics-informed neural networks for non-linear system identification for power system dynamics," in *Proc. IEEE Madrid PowerTech*, Madrid, Spain, 2021, pp. 1–6, doi: 10.1109/PowerTech46648.2021.9495063.

Chapter 6

6

Experimental Data Analysis and Model Comparison

As discussed in the previous chapters, the transient region of the waveform provides valuable insights into the system's dynamic characteristics. By analyzing this region, it becomes possible to identify the physical parameters of the system more accurately and to understand how it responds to sudden perturbations or changes in operating conditions.

Therefore, studying the transient response not only helps in parameter estimation but also provides a deeper understanding of the underlying physical processes governing the system's dynamics. In this chapter, we focus on the study and analysis of the transient response observed in the real data.

6.1 Exprimental setup

To experimentally validate the proposed approach, two series-connected PV panels from SOLBIAN, model SP16L [1], were used for testing. This configuration provided the voltage level required by the power converter, ensuring compatibility with the laboratory setup. Under STC, the array delivers a nominal power of 108 W, with an open-circuit voltage of $V_{oc} = 23.02\,\mathrm{V}$,

a maximum power point voltage of $V_{mpp} = 19.2\,\mathrm{V}$, a short-circuit current of $I_{sc} = 6\,\mathrm{A}$, and a maximum power point current of $I_{mpp} = 5.6\,\mathrm{A}$.

The array was characterized with a BioLogic SP-200 potentiostat equipped with an HCV-3048 power booster and an HV-48 high-voltage probe [2]. This setup enabled IV curve measurement to determine the maximum range of step perturbations. Measurements were automated using the EC-Lab Dynamic Link Library interfaced with a Python script. The protocol consisted of a DC voltage sweep to obtain the IV curve, followed by MPP identification. Irradiance was monitored with a Kipp-Zonen CMP10 pyranometer [3], and cell temperature with a PT100 sensor mounted on the rear surface.

A three-phase interleaved boost converter was used to apply the step perturbation [4]. Based on the I-V characterization, the converter's duty cycle was configured to establish a stable initial operating point for the PV string near the Maximum Power Point (MPP). This point was intentionally set on the constant-voltage side of the I-V curve, at a voltage $V = 1.2 \cdot V_{\mathrm{MPP}}$. From this position, the step perturbation could be applied across the linear MPP region without falling into the constant-current region. Voltage and current waveforms were acquired using a Tektronix 3 Series MDO oscilloscope [5]. Voltage measurements were performed with a THDP0200 differential probe, offering a $150\,\mathrm{V_p}$ range and 20 MHz bandwidth [8], while current was measured using a TCP0030A 30A AC/DC probe [9]. The acquisition system was configured to record 10 M samples over a $10\,\mu\mathrm{s}$ time window, achieving an effective sample rate of $1\,\mathrm{GS/s}$. This high-density, single-shot capture ensures nanosecond-level temporal resolution, enabling accurate characterization of fast transients without aliasing or data distortion. The resulting waveforms serve as the basis for subsequent analysis and model validation.

6.2 waveform analysis

Figures 6.1a and 6.1b show the measured voltage and current waveforms of the photovoltaic panel under real experimental conditions.

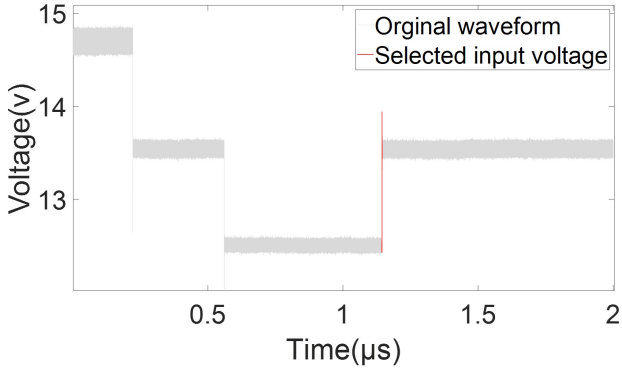

(a) Measured voltage waveform of the PV panel. The red line indicates the selected transient time window.

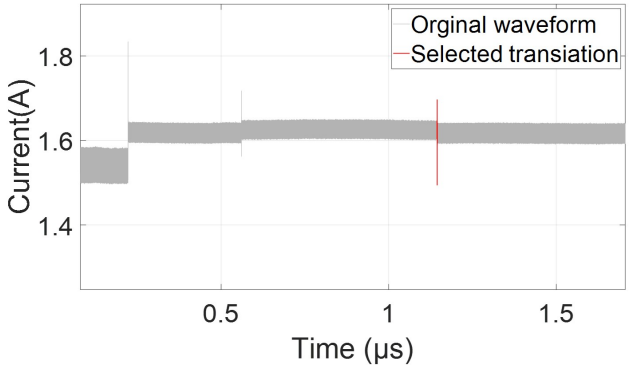

(b) Measured current waveform of the PV panel. The red line indicates the corresponding transient region extracted from the measured data.

Figure 6.1: Measured voltage and current waveforms of the photovoltaic panel under real experimental conditions.

As illustrated in Figures 6.1a and 6.1b, the input voltage exhibits a stepwise variation, and for each voltage step, the output current responds with a transient behavior before settling to a new steady-state value.

The measured data are noisy due to real operating conditions. To

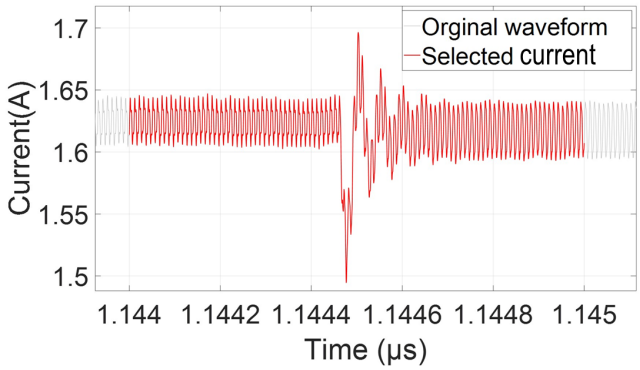

(a) Selected transient region of the measured current waveform.

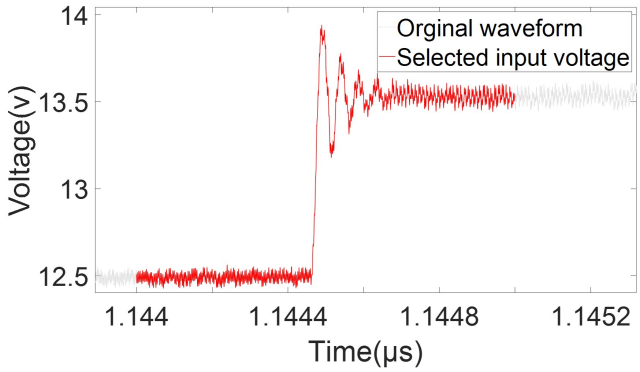

(b) Selected transient region of the measured voltage waveform.

Figure 6.2: selected transient regions in the measured voltage and current waveforms. The red wavefrom correspond to the specific time window extracted from the original data for dynamic analysis.

analyze the panel's dynamic behavior, a specific transient time window is selected from both the voltage and current signals. This window includes 2,481 data samples and represents the transition between two steady-state operating points, as shown by the red waveform in Figures 6.1a and 6.1b. The gray waveform corresponds to the complete dataset that includes 10 million data points. Since the transient region is of primary interest in this study, it is not necessary to include the entire 10 million point dataset. Therefore, the red segment including 2,481 samples is extracted and analyzed to capture the essential dynamic behavior between the two steady states.

Figures 6.2a and 6.2b show the selected transient time windows of the measured voltage and current waveform from the PV panel. In Figure 6.2a, the input voltage exhibits a step increase followed by brief oscillations around the new steady-state value and in Figure 6.2b, the output current presents a dynamic transition in response to the voltage step, and finally settles to a new steady-state value.

Overall, Figures 6.2a and 6.2b illustrate the system's transition between two steady-state operating points. These selected regions form the basis for parameters estimation and the training of the PINN model.

6.3 Parameter Estimation from Experimental PV Data Using Physics-Informed Neural Networks

Before applying the PINN for parameter estimation, we obtain an initial approximation of the PV model parameters using the static SDM based on the electrical characteristics provided in the module datasheet.

Under STC, the datasheet provides only four characteristic points: the open-circuit voltage (V_{oc}), the short-circuit current (I_{sc}), the voltage at the maximum power point (V_{mpp}), and the current at the maximum power point (I_{mpp}). However, to accurately estimate the parameters, it is necessary to consider the actual operating point of the PV module, since the parameters depend on the voltage–current conditions. The measured operating point of the PV module ($V = 13.5$ V, $I = 1.65$ A) is used to further refine and verify the parameter estimation under real experimental conditions. The static parameters of the PV panel at the measured operating point are determined by numerically solving the nonlinear system through the Newton–Raphson method [6]. The obtained values represent:

$$R_s \approx 0.28\ \Omega, \qquad R_{sh} \approx 58\ \Omega, \qquad I_{ph} \approx 1.64\ \text{A},$$

This estimation provides the static parameters of the model.

To estimate the model parameters based on measurement data, a standard PINN is used while assuming linear capacitor behavior in the model. Due to the noise in the measured waveform of the experimental data, an adaptive loss weighting approach is use to ensure a balanced contribution between the data information and physics information during parameter estimation. The relative weights of these loss components are dynamically adjusted during training, allowing the network to dynamically adjust the influence of each loss component, ensuring that no term dominates the optimization process, following the adaptive weighting formulation presented in Chapter 3.

The details of the neural network and training configuration are provided in Table 6.1.

For training, we use the parameter ranges in Table 6.2 with random initial values. The parameter ranges are centered around the nominal datasheet values and extended up to about three times their magnitude. Since no specific reference is available for the capacitance value based on datasheet value, its range is determined based on the typical values considered in the previous chapters and reported in the literature for PV systems.

Table 6.1: Neural Network and Training Details

Category	**Details**
Neural Network Structure	10 neurons, 3 hidden layers
Activation Function	Tanh
Optimizer	AdamW
Input Data Points	2481
Parameters Estimated	R_s, R_{sh}, C, i_{ph}
Training Epochs	20,001
Learning Rate	0.0005

Table 6.2: Parameter ranges considered for the estimation process.

Parameter	**Range**
I_{ph}	$[0.5\text{A},\ 5\text{A}]$
R_s	$[0.1\Omega,\ 0.85\Omega]$
R_{sh}	$[20\Omega,\ 180\Omega]$
C	$[1 \times 10^{-6}\,\text{F},\ 5 \times 10^{-6}\,\text{F}]$

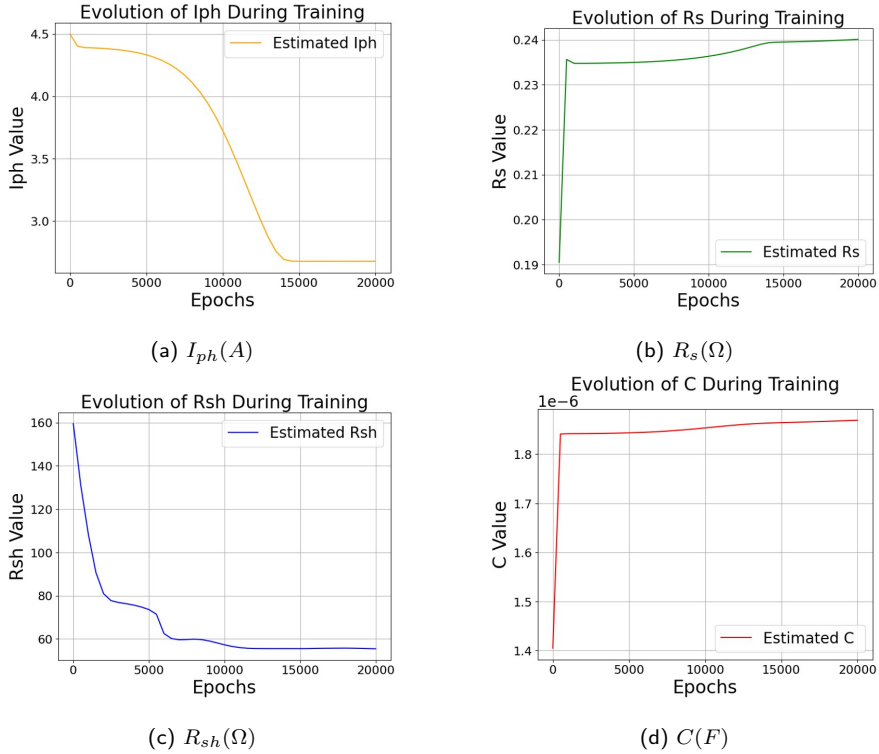

(a) $I_{ph}(A)$ (b) $R_s(\Omega)$

(c) $R_{sh}(\Omega)$ (d) $C(F)$

Figure 6.3: Evolution of estimated parameters during training for the linear case.

Figure 6.3 shows that the estimated parameters converge to values close to the datasheet values under the considered operating conditions. Figure 6.4 illustrates the convergence of the adaptive weight parameter α, which becomes negative during training. This indicates that the network decreases

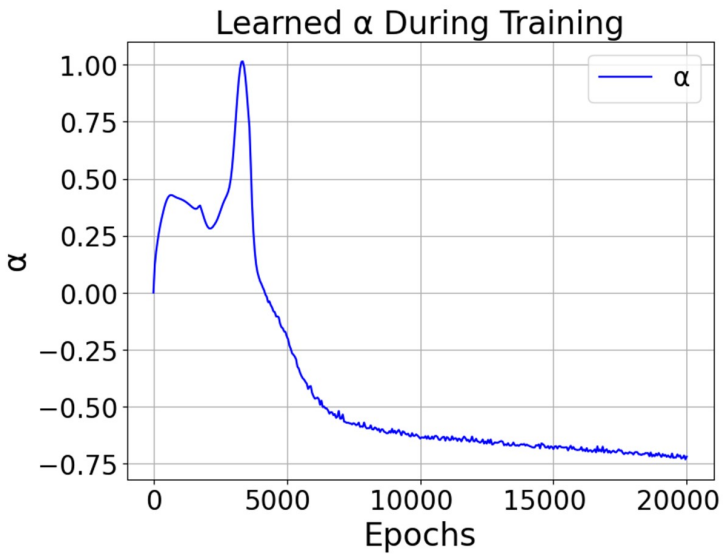

Figure 6.4: Evolution of α during training.

the influence of the data base term in cost function and relies more on the physics information, consistent with the adaptive weighting approach described in Chapter 3.

The complete measured current data over the selected time range is illustrated in Fig. 6.5(a). To enable a more detailed analysis of the system behavior in the transient region, the section of the transient region data highlighted by the boxed area has been magnified, as shown in Fig. 6.5(b). This zoom is only a closer view of the same raw data, without any filtering or processing, allowing a clearer observation of the instantaneous variations and oscillations in the current response.

To better evaluate the model's performance, a detailed view of the transient section is provided in Fig. 6.6 to examine how the predicted current compares with the measured data.

The predicted current does not fit the measured data well in some regions because during the transition to a new operating point, the system exhibits additional nonlinear behavior that cannot be perfectly captured when a linear capacitance value is assumed, which also affects the current response and contributes to the observed mismatch. For this reason, the model is fur-

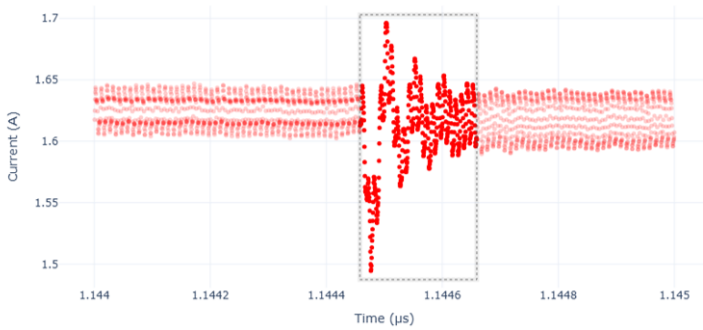

(a) Current data.

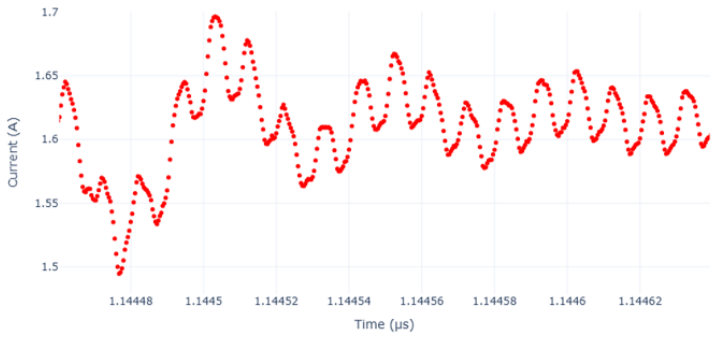

(b) Transient region for better analysis.

Figure 6.5: In the 6.5(a), the complete current data over the selected time range is presented. For a more detailed analysis of the system behavior during the transient region, the boxed area shown in the 6.5(b).

ther developed by a nonlinear capacitance that varies with voltage to better represent the system's dynamic behavior and improve the fitting accuracy. The nonlinear capacitance model considered here follows the same formulation as described in Chapter 3. Random initial values are consider to the parameters, and the parameter ranges are chosen according to Table 6.2, while the details of the neural network architecture and training configuration are provided in Table 6.1. The only exception is the parameter b, whose range is defined based on the previous chapters and relevant literature, and is set between $[2\times10^{-16}$ F, 6×10^{-16} F], corresponding to values reported for

the PV technology.

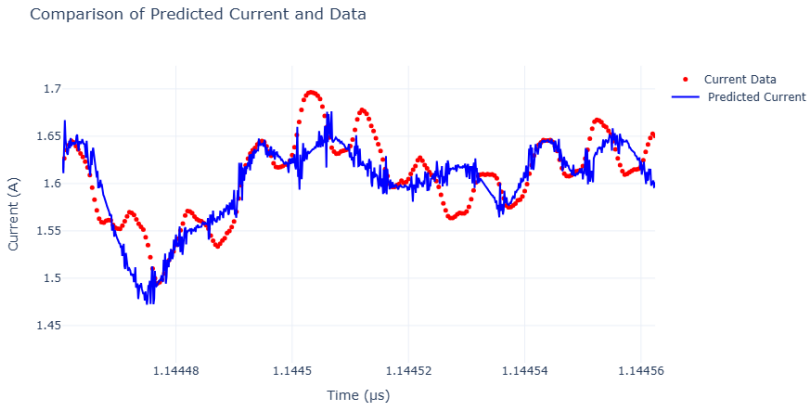

Figure 6.6: Comparison of current waveform and PINN-identified waveform.

Figure 6.7 illustrates the convergence of the estimated parameters.

As shown in Figure 6.8, the convergence in the transient region is improved, and the predicted current exhibits a much better fit compared to the model with a constant capacitance.

To evaluate the performance of the different estimation methods, we use a GA with a population size of 15 and optimization for 100,000 generations to evaluate the performance of different estimation methods.

RMSE values of each method are show in the Figure 6.11. The results show that the PINN for nonlinear model achieves better identified waveform than the GA and PINN for linear model. Because the measured voltage and current waveform are affected by a high level of experimental noise, the PINN leverages the governing circuit equations to guide the optimization toward physically consistent solutions. This improvement results from incorporating a nonlinear voltage-dependent capacitance, which enables the model to more accurately capture the dynamic response of the PV module under varying operating conditions.

Table 6.3 summarizes the estimated parameter values obtained by the GA and PINN method for both the linear and nonlinear models. The results show that the parameters identified by the PINN are generally closer to the

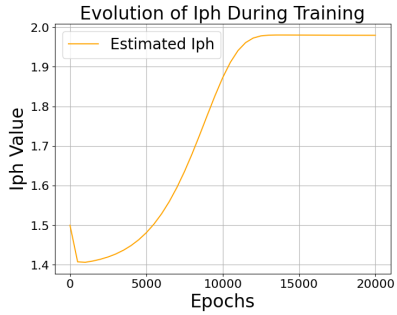

(a) $I_{ph}(A)$

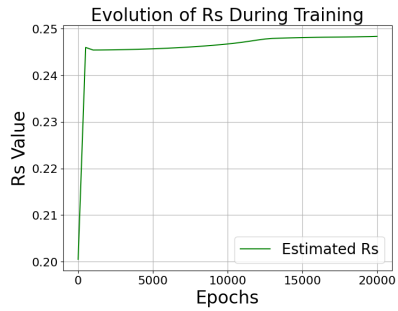

(b) $R_s(\Omega)$

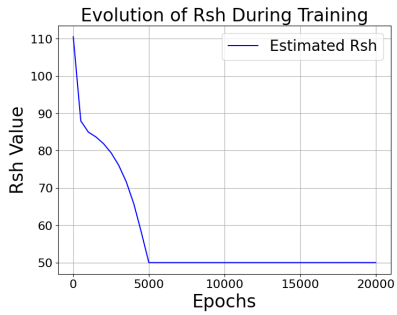

(c) $R_{sh}(\Omega)$

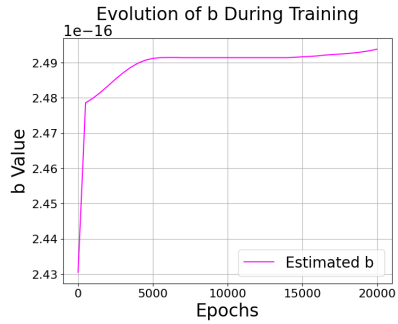

(d) $b(F)$

Figure 6.7: Evolution of estimated parameters during training for the nonlinear case.

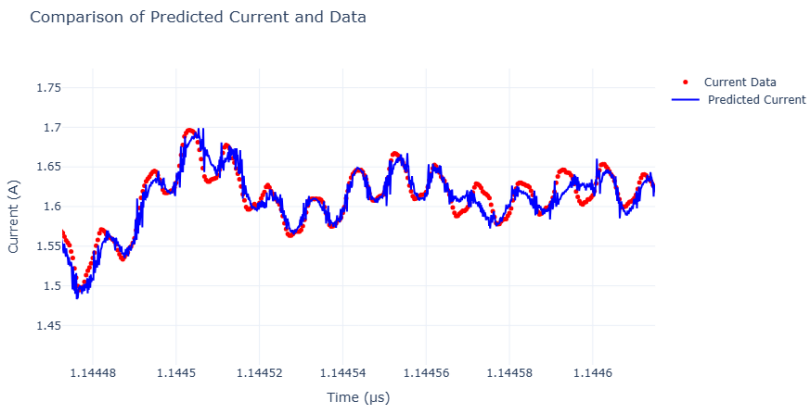

Figure 6.8: Comparison of current waveform and PINN identified waveform for the nonlinear case.

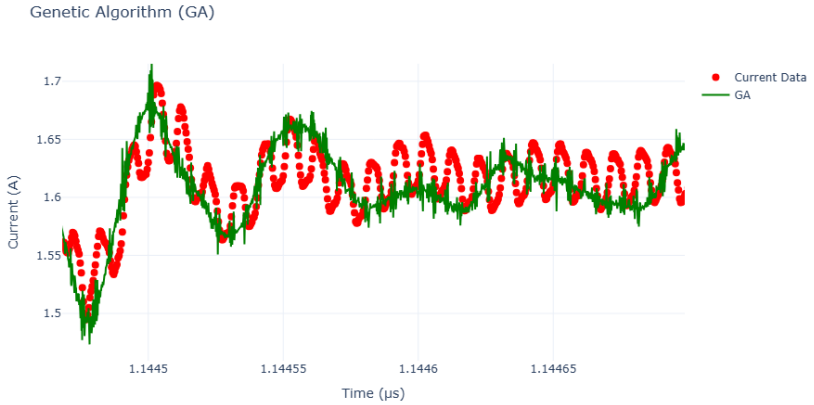

Figure 6.9: Comparison of current waveform and GA identified waveform for linear case.

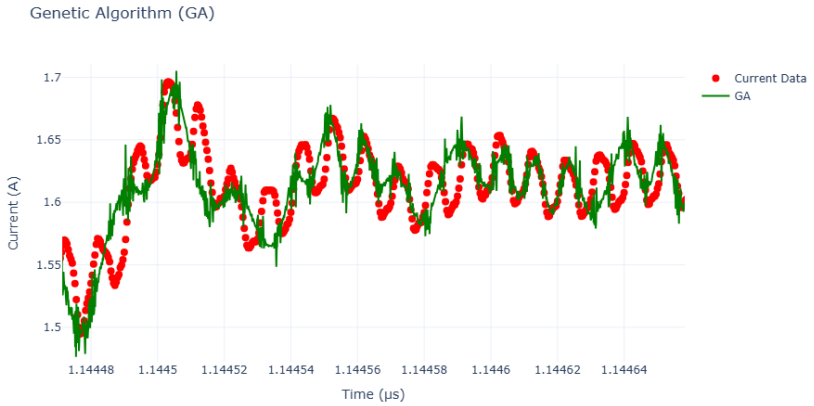

Figure 6.10: Comparison of current waveform and GA identified waveform for nonlinear case.

datasheet values compared to those obtained by the GA.

Figure 6.12 compares the percentage errors of the estimated parameters relative to the datasheet values for both linear and nonlinear models obtained using the GA and PINN methods.

In the inear model, the PINN demonstrates better accuracy compared to the GA in all parameters. Specifically, the error of R_{sh} in PINN is significantly reduced (around 3.8%) compared to GA (about 37%). Similarly,

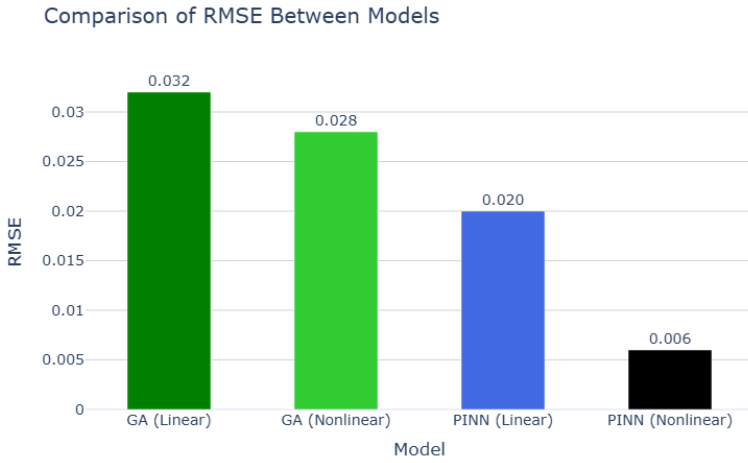

Figure 6.11: Comparison of RMSE between the models.

Table 6.3: Estimated parameters for each model.

Model	R_{sh} (Ω)	I_{ph} (A)	R_s (Ω)	C (F)	b (F)
Datasheet	55.00	1.64	0.28	–	–
GA (Linear)	75.51	1.93	0.35	1.83×10^{-6}	–
PINN (Linear)	57.07	1.83	0.25	1.91×10^{-6}	–
GA (Nonlinear)	73.51	1.88	0.33	–	1.82×10^{-16}
PINN (Nonlinear)	50.20	1.86	0.24	–	2.49×10^{-16}

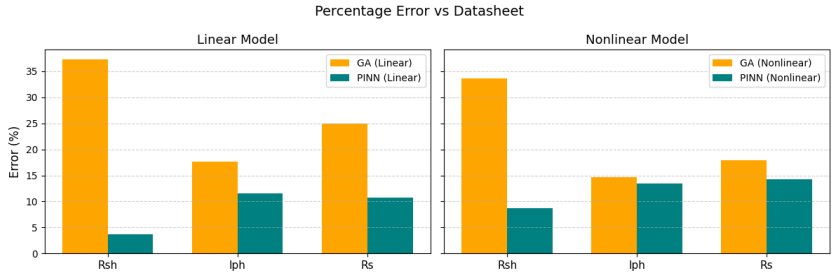

Figure 6.12: Percentage error of the estimated parameters compared with datasheet values for both linear and nonlinear models using GA and PINN approaches.

for I_{ph}, PINN achieves an error of approximately 11.6%, which is lower than the 17.7% error obtained by GA. The series resistance R_s is also estimated

more precisely by PINN (10.7% error) compared to GA (25%).

In the nonlinear model, the PINN maintains better overall performance and stability. The shunt resistance R_{sh} error from about 33.6% in GA and 8.7% in PINN, showing a substantial improvement. Although both methods achieve comparable accuracy for I_{ph} (around 13–15%), the PINN slightly outperforms GA in estimating R_s (14.3% vs. 17.9%).

Overall, these results confirm that the PINN yields more reliable and physically consistent parameter estimations compared to the GA.

In summary, the proposed PINN framework provides an efficient, noise-resilient, and physically consistent approach for extracting equivalent circuit parameters of PV modules from real transient measurements. The experimental analysis demonstrates that the transient of the PV waveform carries essential information about the system's dynamic behavior. The results show that the PINN achieves significantly lower estimation errors than the GA for all parameters, confirming the benefit of embedding the circuit's physical equations into the learning process. Between the two PINN configurations, the nonlinear version provides better fit in the transient region. Overall, the results support the effectiveness of the PINN framework in extracting physically consistent parameters and reproducing the observed transient dynamics, even under noisy real-world measurements.

References

[1] https://www.solbian.eu/en/sp-series/23-sp-16-l.html

[2] https://www.biologic.net/products/sp-200/

[3] https://www.kippzonen.com/Product/276/CMP10-Pyranometer

[4] Pavon-Vargas, C., Bouvier, Y. E., Rodriguez-Lorente, A., Lopez, J. V., Petrone, G. (2025, June). Multiphase Interleaved DC-DC Converters for Impedance Spectroscopy in Photovoltaic Diagnostics: Findings from SPICE Simulations. In 2025 International Conference on Clean Electrical Power (ICCEP) (pp. 262-268). IEEE.

[5] https://www.tek.com/en/products/oscilloscopes/3-series-mdo

[6] J. Stiasny, G. S. Misyris, and S. Chatzivasileiadis, "Physics-informed neural networks for non-linear system identification for power system dynamics," *2021 IEEE Madrid PowerTech*, pp. 1–6, 2021, doi: 10.1109/PowerTech46648.2021.9495063.

[7] N. Femia, G. Petrone, G. Spagnuolo, and M. Vitelli, *Power Electronics and Control Techniques for Maximum Energy Harvesting in Photovoltaic Systems*. Boca Raton, FL: CRC Press, 2017.

[8] https://www.tek.com/en/datasheet/high-voltage-differential-probes

[9] https://www.alldatasheet.com/datasheet-pdf/pdf/889275/CUI/CP30.html

Chapter 7

7

Conclusion and outlook

In this thesis, we focus on the identification of parameters in dynamics PV generators through a comprehensive time-domain analysis framework. Unlike conventional steady-state or frequency-domain methods, the time-domain approach enables the direct observation of the transient and dynamic response of the PV system, offering deeper insight into its nonlinear behavior under real operating conditions. This perspective allows for the accurate tracking of current–voltage interactions and the extraction of system parameters that are often hidden in static analysis.

To ensure accuracy, stability, and physical consistency, a PINN framework was developed and optimized for PV system modeling. The proposed PINN not only learns from measured data but also embeds the governing physical equations directly into the learning process. This hybrid structure bridges the gap between data-driven and physics-based modeling, ensuring that the estimated parameters remain consistent with the real system behavior.

Based on the PINN structure, two novel PINN architectures were designed to explore different ways of balancing data with physical constraints. The first architecture emphasizes high-precision fitting of experimental waveforms, while the second focuses on improving generalization and robustness under varying environmental conditions. Furthermore, the thesis investi-

gates the effect of scaling, normalization, and adaptive loss weighting to enhance the convergence speed and stability of the network during training.

The results demonstrate that the proposed PINN frameworks are capable of accurately estimating PV parameters with high precision and robustness. Even in the presence of measurement uncertainty or noise, the models maintained consistent performance and physical interpretability.

The developed methodologies not only enhance parameter estimation accuracy but also contribute to the understanding of PV system dynamics, offering a foundation for future developments in diagnostics, control, and performance optimization of renewable energy systems.

The research is structured across 7 chapters, each addressing a specific stage in the development, implementation, and validation of the proposed methodologies, progressively advancing from theoretical background to experimental verification.

This study demonstrates the practical feasibility of the proposed PINN framework and confirms its capability to perform real-time diagnostic and parameter estimation tasks in actual PV systems with strong physical consistency and adaptability across different operating conditions.

One direction for future development is the design and implementation of hybrid PINN–LSTM architectures that incorporate temporal memory and long-term dependencies between transient responses. By integrating a recurrent structure such as LSTM or GRU with the PINN framework, temporal features of the voltage and current signals $v(t)$ and $i(t)$ are encoded into a dynamic latent space and then processed by the PINN head to enforce the physical consistency of the circuit equations. In this configuration, the LSTM acts as a temporal encoder that captures sequential dependencies, while the PINN ensures that the predicted behavior follows the underlying physical laws through automatic differentiation of the governing equations. As a result, the hybrid model simultaneously forecasts the next current waveform, estimates the physical parameters, and minimizes the residual of the PV dynamic equation.

A critical aspect of this development is the treatment of the vanishing

gradient problem, which becomes significant in PV circuits that operate on very short time scales. The transient responses in such systems occur in the range of microseconds to milliseconds, and the temporal derivatives of voltage and current, computed through automatic differentiation within the PINN framework, tend to approach zero because of the small numerical magnitude of the time variable. As a result, the associated gradients decay rapidly during backpropagation, which prevents the network from effectively updating its weights and capturing the fast dynamics. This phenomenon slows down convergence and can even stop learning in deep or long-sequence models.

This issue is addressed through time rescaling, where the temporal variable is normalized from the microsecond domain to the second domain during training. This normalization keeps the derivatives within a numerically stable range and preserves effective gradient flow throughout the network. After training, all quantities are rescaled back to their original physical domain to ensure accurate physical interpretation. This method stabilizes the learning process and prevents early gradient decay in the physics-based layers. However, the vanishing gradient remains an important open issue in physics-informed machine learning because the accuracy of these models strongly depends on the stability of gradient propagation. This challenge becomes even more critical for online monitoring and adaptive control applications, where the model must react in real time under high-frequency variations. Future research may explore advanced gradient normalization techniques, improved weight initialization, and multi-scale PINN architectures that jointly model both fast electrical transients and slower environmental effects to maintain consistent performance across all operating conditions.

Another direction for future work is the extension of the current single-scenario framework toward a graph-based state representation using Graph Neural Networks (GNNs). In the current study, the network is trained and tested under a single operating condition and waveform scenario. In real PV systems, however, multiple operating states coexist, such as different irradiance levels, partial shading, or converter switching modes, all of which

influence the electrical and dynamic behavior of the circuit. By representing each operating condition as a node in a state graph and defining weighted connections that describe the transition probabilities or correlations between these nodes, a state matrix can capture the full dynamic landscape of the system. Integrating GNNs into the PINN framework allows the model to learn relationships between different operating states, share knowledge across conditions, and generalize to unseen scenarios without retraining. This graph-based extension also supports the development of adaptive control and fault diagnosis systems, where the model transitions between learned states based on real-time sensor feedback.

Combining the hybrid PINN–LSTM temporal modeling, gradient-stabilized training, and GNN-based state representation creates a comprehensive, multi-layer learning framework that handles both fast transients and global operational variability. Such an integrated approach enables robust and physically consistent real-time monitoring, prediction, and control of PV systems under a wide range of environmental and circuit-level conditions.

Another direction for future research involves integrating the developed PINN framework within a Digital Twin (DT) architecture supported by a Control Communication Network (CCN) to enable real-time monitoring, control, and optimization of large-scale PV systems. In this approach, the Digital Twin acts as a virtual representation of the physical PV system, continuously synchronized with live sensor data such as voltage, current, temperature, and irradiance. The PINN operates as the analytical core of the twin, combining measurement data with the governing physical equations to dynamically estimate parameters and internal states. The Control Communication Network (CCN) serves as the communication backbone connecting the physical PV assets and their digital counterparts. It enables bidirectional data flow, allowing sensor information, control commands, and model updates to be exchanged in real time with minimal latency. Through this connection, the Digital Twin can perform adaptive learning and predictive control, updating the internal model as new measurements arrive.

By coupling the CCN infrastructure with the physics-informed capa-

bilities of PINNs, the Digital Twin can evolve into an intelligent, self-adaptive monitoring system capable of identifying parameter drifts, detecting faults at early stages, predicting performance under varying irradiance and temperature profiles, and autonomously optimizing operating conditions. This integration would extend the current PINN-based modeling approach from single-module estimation to a system-level framework, enabling scalable, predictive, and real-time management of PV plants and future smart energy grids.

Overall, this research contributes to advancing intelligent and physically consistent modeling approaches for next-generation PV systems, paving the way for more resilient, efficient, and autonomous renewable energy infrastructures.

Appendix

.1 Appendix A: Multiple Physics-Informed Neural Network Framework

Instead of estimating all parameters using a single neural network, a Multiple PINN architecture is adopted. The parameter vector is decomposed as:

$$\boldsymbol{\theta} = [\boldsymbol{\theta}^{(1)}, \boldsymbol{\theta}^{(2)}], \tag{1}$$

where each subset of parameters is learned by an independent neural network.

Two neural networks are defined in parallel:

$$\boldsymbol{\theta}^{(1)}(\mathbf{x}) = \mathcal{N}_1(\mathbf{x}; \mathbf{w}_1), \qquad \boldsymbol{\theta}^{(2)}(\mathbf{x}) = \mathcal{N}_2(\mathbf{x}; \mathbf{w}_2), \tag{2}$$

where $\mathcal{N}_1$ and $\mathcal{N}_2$ are fully connected feedforward neural networks with different architectures. Each neural network has its own set of trainable weights and biases, represented by $\mathbf{w}_1$ and $\mathbf{w}_2$.

Although the networks are structurally independent, they are coupled through the same physics-based model. The estimated parameters are injected into the governing equations to compute the model output current:

$$I_{\text{model}}(t) = \mathcal{F}\big(v(t), \boldsymbol{\theta}^{(1)}(\mathbf{x}), \boldsymbol{\theta}^{(2)}(\mathbf{x})\big), \tag{3}$$

where $\mathcal{F}(\cdot)$ represents the physical equations of the system, which are identical for both networks.

Both neural networks are trained simultaneously by minimizing a single global loss function defined as:

$$\mathcal{L}(\mathbf{w}_1, \mathbf{w}_2) = \mathcal{L}_{\text{data}} + \mathcal{L}_{\text{phys}}, \tag{4}$$

where $\mathcal{L}_{\text{phys}}$ loss of the governing differential equations and $\mathcal{L}_{\text{data}}$ enforces consistency between original data and modeled data. This formulation represents a baseline structure and can be extended by incorporating additional loss terms to account for further physical constraints, regularization, or problem-specific objectives.

The loss function is minimized with respect to both parameter sets, and gradients are computed via backpropagation through the shared physics model:

$$\nabla_{\mathbf{w}_k}\mathcal{L} = \frac{\partial \mathcal{L}}{\partial \boldsymbol{\theta}^{(k)}} \frac{\partial \boldsymbol{\theta}^{(k)}}{\partial \mathbf{w}_k}, \qquad k \in \{1, 2\}. \tag{5}$$

This formulation enables parallel training of multiple neural networks while enforcing physical consistency through a common loss function and shared governing equations. The framework can be readily extended to more than two networks without modifying the underlying physics or optimization strategy.

.2 Appendix B: Two-Level Layered Physics-Informed Neural Network

To improve convergence and decouple parameters with different physical roles, a two-level layered PINN architecture is employed. The physical parameters are organized into:

$$\boldsymbol{\theta} = \{\boldsymbol{\theta}^{(1)}, \boldsymbol{\theta}^{(2)}\}, \tag{6}$$

where $\boldsymbol{\theta}^{(1)}$ represents global operating condition parameters and $\boldsymbol{\theta}^{(2)}$ represents dynamic parameters.

The first-level network is designed to capture the dominant, large-scale components of the system dynamics. These parameters are estimated through a neural network of:

$$\boldsymbol{\theta}^{(1)}(t) = \mathcal{N}_1(t, v(t), i(t); \mathbf{w}_1), \tag{7}$$

where $\mathbf{w}_1$ collects the trainable weights and biases of the first-level network.

By learning the dominant system behavior at this stage, the first-level network provides a coarse but physically consistent representation of the dynamics, effectively resolving parameters associated with larger numerical scales. This learning strategy reduces scale imbalance.

The second-level network is designed to resolve parameters whose numerical scales are significantly smaller than the dominant scale of the overall system dynamics. These parameters are learned through a second neural network of:

$$\boldsymbol{\theta}^{(2)}(t) = \mathcal{N}_2(t, v(t), i(t), \boldsymbol{\theta}^{(1)}(t); \mathbf{w}_2), \tag{8}$$

where $\mathbf{w}_2$ collects the trainable weights and biases of the second-level network.

The outputs of the first-level network provide a coarse, physically consistent representation of the dominant system behavior and are therefore used as informed inputs to the second level. This structure allows the second-level network to focus on learning fine-scale dynamics once the large-scale effects have been resolved.

Both levels are trained using the same loss function:

$$\mathcal{L}(\mathbf{w}_1, \mathbf{w}_2) = \mathcal{L}_{\text{phys}} + \mathcal{L}_{\text{data}}, \tag{9}$$

where $\mathcal{L}_{\text{phys}}$ loss of the governing differential equations and $\mathcal{L}_{\text{data}}$ enforces consistency between original data and modeled data. This formulation represents a baseline structure and can be extended by incorporating additional loss terms to account for further physical constraints, regularization, or problem-specific objectives.

The loss function is minimized with respect to both parameter sets, and gradients are computed via backpropagation through the shared physics model:

$$\nabla_{\mathbf{w}_k} \mathcal{L} = \frac{\partial \mathcal{L}}{\partial \boldsymbol{\theta}^{(k)}} \frac{\partial \boldsymbol{\theta}^{(k)}}{\partial \mathbf{w}_k}, \qquad k \in \{1, 2\}. \tag{10}$$

This layered formulation reduces interference between parameter spaces, improves convergence for highly nonlinear parameters, and ensures that the learning process follows the physical structure of the underlying model.

Acknowledgement

Trust me on this: Confidence isn't built by thinking positive thoughts. It's built by doing difficult things while your brain screams at you to stop. It's built in the quiet moments when you keep going, not because you're sure of the outcome but because quitting would mean betraying the person you're becoming. Confidence is born when you send the email you're terrified to send. When you walk into that meeting still shaking. When you rewrite that chapter for the seventh time. When your chest is tight, your eyes are swollen, and you still show up to your work not out of strength, but survival. It's the choice to stand again, even when nothing inside you feels steady. You earn your strength in yourself, through every moment no one applauds but you keep going anyway. Not because you have to, Because you "can".

I carried the weight of being far from my family and my country, but I carry my homeland in my heart always and persian woman means standing for Woman, Life, Freedom.

I want to thank to my supervisor, Prof. Giovanni Spagnuolo, for his guidance throughout this journey. A part of my heart will always stay in Lab 142.

Acronyms

AD additiv. 50

CAN-PINN Coupled automatic-numerical automatic–numerical differentiation PINNs. 48

CPE Constant Phase Element. 37

ECM Equivalent Circuit Model. 33, 63

IS Impedance Spectroscopy. 36–38

I–V current-voltage. 18, 34, 36, 37

KdV Korteweg–de Vries. 47, 48

MFLP-PINN Multiaxial fatigue life prediction physics-informed neural network. 49

MPP Maximum Power Point. 3, 34, 39, 40, 63, 68

MPPT Maximum Power Point Tracking. 3, 19, 39–41, 63, 68

P&O Perturb and Observe. 3, 19, 20, 23, 39, 40, 63

PDE Partial Differential Equation. 67

PIGNN Physics-Informed Graph Neural Network. 50

PIML Physics-Informed Machine Learnin. 50

PINN Physics Informed Neural Network. 11, 20–24, 46–51, 63, 65, 67–70, 72

PMU Phasor measurement unit. 50

PV Photovoltaic. 3, 4, 11, 17–25, 33–41, 51, 63, 64, 69

P–V Power–Voltage. 3, 34, 39, 40

SDM Single-diode model. 3, 4, 18, 23, 33–35, 37, 63, 64, 68

STC Standard test condition. 11, 68, 69

sync synchronization. 50